May, 2002

A time-resolved method for nonlinear acoustic measurement

Stephen D. Holland, *Iowa State University*

A TIME-RESOLVED METHOD FOR NONLINEAR ACOUSTIC MEASUREMENT

A Dissertation

Presented to the Faculty of the Graduate School

of Cornell University

in Partial Fulfillment of the Requirements for the Degree of

Doctor of Philosophy

by

Stephen D. Holland

May 2002

A TIME-RESOLVED METHOD FOR NONLINEAR ACOUSTIC MEASUREMENT

Stephen D. Holland, Ph.D.

Cornell University 2002

We describe a time-resolved method for measuring nonlinear ultrasonic phenomena. Conventional approaches to the measurement of nonlinear phenomena utilize narrowband measurements of harmonic generation. These measurements are fundamentally narrowband and hence have poor time resolution. In contrast, our method utilizes a series of narrowband bursts that can be combined to form a composite time-resolved broadband impulse. Simultaneous time resolution and harmonic isolation are thereby obtained. The composite impulse can then be used to perform time-resolved measurements of weakly nonlinear phenomena. Such time-resolved measurements have the potential to dramatically improve the capability and performance of nondestructive testing systems that use acoustic nonlinearity to detect flaws.

We develop a mathematical theory by which these measurements can be explained, and describe an algorithm for performing the measurements. To evaluate the method and its utility, we present several demonstrative experiments. We also perform numerical simulations analogous to the experiments and apply theory in order to better understand the measurements and the underlying phenomena.

BIOGRAPHICAL SKETCH

Stephen D. Holland was born in Boston on September 19, 1975. He grew up in the town of Wayland, Massachusetts, attending Wayland High School and graduating in 1993. He started his undergraduate studies at Cornell in the Fall of 1993 majoring in Electrical Engineering. He graduated in January, 1997 and started his doctoral work at Cornell immediately thereafter. He completed his doctoral studies with the publication of this dissertation in May, 2002.

Stephen enjoys the outdoors, and is an active participant in many activities, including mountain biking, rock climbing, and cross-country skiing.

To my grandparents.

ACKNOWLEDGEMENTS

I would like to thank Professor Wolfgang Sachse, my advisor, for making this research possible. Thanks go also to Professors Richard Weaver and Sigrun Hirsekorn for their comments, suggestions, and answering questions. Finally, I thank my parents for help editing drafts.

This work was supported by the Air Force Office of Scientific Research under Grant #F49620-98-1-0338.

This work made use of the Cornell Center for Materials Research facilities supported by NSF under Award No. DMR-0079992.

TABLE OF CONTENTS

Biographical Sketch . . . iii
Dedication . . . iv
Acknowledgements . . . v
Table of Contents . . . vi
List of Tables . . . ix
List of Figures . . . x
List of Symbols . . . xii

1 Introduction 1

2 Experimental methods in nonlinear acoustics 5
2.1 History . . . 6
2.2 Standard experimental technique . . . 6
2.3 Our technique . . . 8
2.4 Other phenomena . . . 9

3 A Model of a Weakly Nonlinear Medium 10
3.1 Impulse response . . . 11
3.2 Volterra expansion . . . 12
3.3 Reduced Volterra expansion/Taylor series . . . 13
3.4 Representation of the model as a convolution . . . 13
3.5 Restrictions of the model . . . 15
3.6 Amplitude sensitivity . . . 15
3.7 Weak nonlinearity . . . 16

4 Measurement algorithm 17
4.1 Mathematical justification . . . 17
4.2 Measurement procedure . . . 19
4.3 Interference and Error . . . 21
4.3.1 Non-ideal behavior . . . 21
4.3.2 Algorithmic interference . . . 22
4.4 Relation to other techniques . . . 24
4.4.1 Conventional CW or burst harmonic generation measurements 24
4.4.2 "Vibroseis" method . . . 25

5 Implementation of the measurement algorithm 26
5.1 Implementation with an analog signal processing system . . . 26
5.2 Experimental techniques . . . 28
5.2.1 System design . . . 28
5.2.2 Frequency step dithering . . . 32
5.2.3 Amplifier gate time dithering . . . 33
5.3 Typical wavelet . . . 35
5.4 Implementation with a digital signal processing system (proposed) . 36

5.5 Limiting factors of the measurement . . . 38

6 Simulation **40**
6.1 A tool for verification . . . 40
6.2 Finite difference model . . . 40
6.3 Convergence issues and $\frac{\Delta x}{\Delta t}$ . . . 42
6.4 Model of a crack or dry contact . . . 44
6.5 Integration with data collection . . . 45
6.6 Nonlinear wave propagation demonstration . . . 48

7 Experiment: Harmonic generation in Water **49**
7.1 Experimental configuration . . . 49
7.2 Experimental results . . . 51
7.3 Simulation results . . . 56
7.4 An analytic solution . . . 56

8 Experiment: Measurements on a crack **64**
8.1 Experimental configuration . . . 64
8.2 Results . . . 66
8.3 Analysis . . . 68

9 Experiment: Harmonic generation at a dry contact **71**
9.1 Experimental configuration . . . 71
9.2 Experimental results . . . 73
9.3 Simulation results . . . 76

10 A blueprint for future development **80**

11 Conclusions **82**

A Derivations **83**
A.1 Demonstration that the discrete time Volterra expansion is a Taylor series . . . 83
A.2 Difference equation of a weakly nonlinear medium . . . 84
A.3 Derivation of the nonlinear PDE from the discrete time difference equation . . . 86
A.4 Derivation of the nonlinear PDE from the nonlinear elastic constitutive law . . . 87
A.5 Dispersive behavior of the linearized difference equation . . . 88
A.6 Derivation of the force-displacement equation for the dry-contact model . . . 90
A.7 Demonstration of the analytic solution . . . 92
A.8 Demonstration of mapping the analytic solution to our model . . . 95

B Control firmware for an ultrasonic measurement system **97**
B.1 An Internet-enabled client/server laboratory instrument 97
B.2 The RAM-5000 control server 98
B.3 The virtual front panel 101
B.4 Conclusions 102

C Design of a jig to hold transducers for measurement of the cracked titanium sample **103**

References **107**

LIST OF TABLES

B.1 Partial list of server commands. 99

LIST OF FIGURES

4.1 Construction of a broadband impulse from a series of narrowband bursts. 19
4.2 Burst processing demonstration. 20

5.1 Diagram of the hardware used for the time-resolved nonlinear method. 29
5.2 Photograph of the hardware used to carry out the time-resolved nonlinear measurements. 30
5.3 Diagram of the software used for the time-resolved nonlinear method. 31
5.4 Experimental and simulated wavelets used to probe medium. . . . 34
5.5 Second harmonic content of wavelets used to probe medium. 34

6.1 Finite difference model of a nonlinear medium. 41
6.2 Dispersion of the finite difference model as a function of Δx and Δt. 43
6.3 Finite difference modeling of a dry contact or crack. 44
6.4 Stress-strain relation of nonlinear contact model. 46
6.5 Demonstration of simulated wave propagation in a nonlinear medium. 47

7.1 Results from Krassilnikov et al. [16]. 50
7.2 Illustration of experiment showing harmonic generation in water. . 50
7.3 Sample waveforms, harmonic generation in water, propagation distance=4 mm. 51
7.4 Linear (fundamental) impulse response waveforms as source-receiver distance is varied. 52
7.5 Second harmonic impulse response waveforms as source-receiver distance is varied. 52
7.6 Linear (fundamental) impulse response amplitude as source-receiver distance is varied. 53
7.7 Second harmonic impulse response amplitude as source-receiver distance is varied. 54
7.8 Simulated linear impulse response waveforms as source-receiver distance is varied. 57
7.9 Simulated second harmonic impulse response waveforms as source-receiver distance is varied. 57
7.10 Simulated linear impulse response amplitude as source-receiver distance is varied. 58
7.11 Simulated second harmonic impulse response amplitude as source-receiver distance is varied. 58
7.12 Fundamental and second harmonic impulse responses, along with $\partial(\text{fundamental}^2)$, in the time and frequency domains. 62

8.1 Diagram showing the cracked titanium sample and transducer positioning. 65
8.2 Photograph of the cracked titanium sample. 65

8.3 Reflected signals from the crack, fundamental (linear) impulse response. 66
8.4 Reflected signals from the crack, second harmonic impulse response. 67
8.5 Fundamental (linear) impulse response residual. 67
8.6 Second harmonic impulse response residual. 68

9.1 Results from Solodov [24]. 72
9.2 Diagram of Contact Acoustic Nonlinearity (CAN) experiment. . . . 72
9.3 Sample contact acoustic nonlinearity waveforms, Force/Area=11.4 MPa. 74
9.4 Fundamental impulse response waveforms from contact acoustic nonlinearity as a function of applied load. 74
9.5 Second harmonic impulse response waveforms (contact acoustic nonlinearity) as a function of applied load. 75
9.6 Change of first arrival amplitude with applied compressive load, dry-contact CAN. 75
9.7 Stress-strain relation of nonlinear contact model for small stress. . 77
9.8 Amplitude of fundamental and second harmonic signals from simulation experiment. 78
9.9 Amplitude of fundamental and second harmonic signals from simulation experiment, limited stress range. 79

B.1 A sample transcript of direct communication with the server using `telnet`. 100
B.2 Screenshot of the virtual front panel controls. 101

C.1 Design of a jig to hold transducers for the measurement of a cracked titanium sample. 104
C.2 Design of Teflon transducer-holding inserts for a jig to hold transducers for the measurement of a cracked titanium sample. 105
C.3 Photograph of the transducer jig with two inserts and two transducers. 106

LIST OF SYMBOLS

α	σ/L. Parameter for dry contact model.
Δf	Frequency step size.
Δt	Burst width.
Δt	Time step size in simulation.
Δx	Spatial step size in simulation.
$\delta(t)$	Dirac delta function (distribution).
δ_{ij}	Kronecker delta function. $\delta_{ij} = 1$ for $i = j$, $\delta_{ij} = 0$ otherwise.
ϵ	Epsilon, i.e. small number.
ϵ	Strain.
ρ	Density (mass/unit volume).
σ	Stress.
σ	Standard deviation of pin length.
τ	Integration variable for a convolution.
ω	Angular frequency.
A	Cross sectional area.
$\mathbf{A}$	Linear impulse response.
A_{ij}	Convolution matrix corresponding to linear impulse response.
$\mathbf{B}$	Second harmonic impulse response.
B_{ij}	Convolution matrix corresponding to second harmonic impulse response.
c	Acoustic wavespeed.
c	Damping coefficient of a dashpot.
c_Δ	$\Delta x/\Delta t$.
c_{ph}	Phase velocity.
d	Separation of source and receiver.
E	Young's modulus.
E_1	Young's modulus in a nonlinear stress-strain relation.
E_2	Second stiffness modulus in a nonlinear stress-strain relation.
F	Force.
$f(t)$	Arbitrary input function.
$f'(t)$	df/dt.
f_i	Time sample i of $f(t)$.
f_s	Sampling frequency $(1/\Delta t)$.

$g(t)$	Response of system to input $f(t)$.
g_i	Time sample i of $g(t)$.
$\hat{g}_i$	Modeled or estimated value of g_i.
i	The imaginary number. $i^2 + 1 = 0$.
k_1	First stiffness coefficient of a nonlinear spring.
k_2	Second stiffness coefficient of a nonlinear spring.
L	Length of contact region in dry contact model.
m	Mass.
$m(t)$	Waveform measured from receiving transducer.
n	An integer.
r_{over}	$f_s/2f$, $1/2f\Delta t$, or $\pi/\omega\Delta t$. Oversampling factor.
r_{speed}	c_{ph}/c. Ratio of phase velocity of simulated system to correct wavespeed.
r_{step}	c_Δ/c. Factor by which $\Delta x/\Delta t$ is larger than the wavespeed c.
$s(t)$	Probe waveform (burst).
t	Time.
t_0	Excitation time.
$\mathbf{R}$	Receiver filter.
u	Substitution variable for an integration.
$u(t)$	Step function. $u(t) = 0$ for $t < 0$ and $u(t) = 1$ for $t > 0$.
$W_1(t)$	Window function for excitation.
$W_2(t)$	Window function for receiver.
x	Position.
y	Displacement from reference position.
y_x^t	Displacement at position x, time t.

CHAPTER 1

INTRODUCTION

The nonlinear acoustic behavior of materials exposed to high (finite) amplitude sound waves has been studied for several hundred years. Many studies have focused on the quantitative measurement of harmonic generation with the goal of determining higher-order elastic constants, e.g. Breazeale [5], and Breazeale and Philip [6]. Measurements of harmonic generation and nonlinear mixing have been widely deployed as a tool for non-destructive testing. Other researchers have begun to look at more exotic effects such as instability and chaos in the stronger nonlinearity from higher amplitude waves. This dissertation takes an intermediate approach. We look for more data than is normally collected in a measurement of harmonic generation, but we eschew the complexity of strong nonlinearity. Our goal is to use information from weak nonlinearity as a supplement to linear characterization of a medium.

We characterize a linear medium by measuring its impulse response (Green's function). We will propose a model for a weakly nonlinear medium based on the conventional linear impulse response with the addition of higher order 'impulse responses' to characterize the nonlinearity. We will use this model as the basis for an experimental method that measures these 'impulse responses', and we will demonstrate their use in studying a nonlinear medium.

Nonlinear phenomena are widely used for nondestructive testing applications because material nonlinearity is an extremely sensitive indicator of damage, fatigue, and cracking [15]. Conventional measurements of harmonic generation in weakly nonlinear media use narrowband bursts and narrowband detection to

isolate harmonics from each other and from the fundamental frequency. Concomitant with the use of narrowband bursts is poor time resolution and the potential for interference. Without time resolution it is impossible to distinguish adjacent echos from a complex specimen. For this reason, and because absolute amplitude measurements are error-prone, conventional nonlinear nondestructive testing techniques focus on integrating the total nonlinearity observed in a sample. The total nonlinearity is compared with calibrations from known-good and known-bad samples to reach a go/no-go conclusion. A time-resolved measurement would permit a much more detailed examination of the sample. Arrival times of different echos can be directly observed, and their second-harmonic components compared. A known-linear behavior such as a direct reflection from a surface could be used in place of a known-good sample for calibration. Time-resolved nonlinear measurements have the potential to dramatically improve the state-of-the-art in nondestructive testing.

While we have not yet achieved such advances in nondestructive testing, we have developed a first-generation system for time-resolved measurements of nonlinear harmonic generation. Our method uses a series of narrowband bursts at different frequencies to construct a virtual, time-resolved impulse that is used to probe the medium. The summed responses, measured at frequency multiples (harmonics), provide linear and second harmonic 'impulse responses'.

We have performed two demonstrative experiments to show the capability and applicability of this model and measurement method: Measurement of harmonic generation in water, and measurement of Contact Acoustic Nonlinearity (CAN) of two dry-coupled aluminum blocks.

Compared with single frequency burst measurements of harmonic generation, our method collects far more information by using a wide range of frequencies. The additional information, from the different frequencies used for measurement, provides much more time resolution in the recorded signal. High time resolution allows accurate distance or wavespeed measurements, as well as readily interpretable signals free from interference between nearby arrivals. High time resolution also means that this method can be used on higher attenuation samples where only a few wavelengths can propagate before the signal is substantially attenuated. With a single frequency burst measurement, one often obtains uninterpretable interference between multiple echos of reverberation within a small sample. In contrast, using our broadband method one can obtain separate and non-interfering echos. Our focus is on the measurement, not on the physics. The physical phenomena that we measure are well known and have been studied many times before. We have developed a better experimental method for measuring and analyzing these phenomena.

The primary drawback of our method is that the time required for data collection is necessarily increased by the additional information we must gather. Instead of one pulse-echo experiment, we must perform hundreds to thousands at different frequencies. Limitations of the equipment currently in use increase the number of experiments required further, to the hundreds of thousands. Furthermore, our method imposes much stiffer requirements on the analog transducers, amplifiers, and other hardware than single frequency burst measurements. With a single frequency in use, one can use narrowband high-efficiency transducers, narrowband amplifiers, and analog filters to measure the signal at that one frequency and improve isolation and signal-to-noise ratio. In our broadband

system, we must use less efficient broadband transducers and unfiltered broadband amplifiers. These reduce signal strength and increase the difficulty of identifying low amplitude harmonics buried under high amplitude signals. The result is that it is in general more difficult to measure a particular nonlinear phenomenon using our method than with conventional single-frequency burst harmonic measurement. Nevertheless, the improvements in resolution and interpretability, along with the potential for dramatic advances in ultrasonic nondestructive testing, make this method a superior choice for the measurement of acoustic harmonic generation from nonlinear materials or interfaces.

CHAPTER 2

EXPERIMENTAL METHODS IN NONLINEAR ACOUSTICS

> Strike a bell, and the bell rings at its resonance modes. Strike it harder and the bell rings with the same tone, only louder. Now imagine a small crack in the bell, perhaps invisible to the eye. We strike the bell gently and it rings normally. Striking it harder we find, to our surprise, that the tone drops in frequency ever so slightly. Striking it even harder, the tone drops farther down in frequency. The frequency shift is a manifestation of *nonlinearity* due to the presence of the crack. [1]

Nonlinearity creates a paradigm shift in measurement. As scientists, we have been trained in the tools of linearity. We assume proportional behavior. When a butterfly flaps its wings in Florida, why should it change the weather in New York? When we study nonlinear systems, we must be prepared to encounter phenomena fundamentally different from those we have been trained to expect.

Consider the bell once again. Suppose we apply a pair of arbitrary (high amplitude) tones, perhaps 440 and 8000 Hz, to the bell using an audio speaker. Our undamaged (linear) bell rings at only the two frequencies, 440 and 8000 Hz. In contrast, the damaged (nonlinear) bell rings at a large number of frequencies in addition to those applied. We detect vibration at frequency multiples, *harmonics*, of the applied tones: 880, 1320, and 1740 Hz; and 16000, 24000, and 32000 Hz. We also detect mixing between the tones: 8000+440 Hz and 8000-440 Hz [15]. Still higher harmonics and higher order mixing occur, but at much smaller amplitude. Nonlinearity can be a sensitive indicator of flaws or damage [2]. Nonlinearity is readily detectable because nonlinear phenomena, such as

[1] Johnson [15]

harmonic generation or mixing, are distinct and different from those possible within a linear medium.

2.1 History

Theories of finite amplitude wave propagation were developed in the 18th and early 19th centuries by Euler, Poisson, and Lagrange [4]. Investigation was continued in the 19th century by Earnshaw [9]. In 1935 Thuras et al. [27] discussed harmonic generation phenomena in air.

In the late 1950's, interest in nonlinear acoustics began to increase. Krassilnikov et al. [16] published an enumeration of nonlinear elastic parameters of fluids in 1957. Romanenko [21] performed experimental studies of finite amplitude spherical waves in 1959. Ryan et al. [22] measured harmonic content as a function of propagation distance in 1962. Studies of harmonic generation in solids began in the early 1960's. Breazeale and Thompson [7] and Hikata et al. [13] measured harmonic generation in aluminum in 1963, setting off a flurry of interest. The development of nonlinear acoustics has been widely reviewed, for example by Bjørnø [4] and by Breazeale and Philip [6]. Of particular importance was the discovery in the early 1970's by Gits et al. [11] of the correlation of fatigue damage in aluminum with nonlinear distortion of ultrasonic waves.

2.2 Standard experimental technique

In most investigations of harmonic generation or mixing phenomena, narrowband bursts or continuous waves are applied to the sample. Then some measurement

of the response spectrum is performed. Such measurements are commonly referred to as Nonlinear Elastic Wave Spectroscopy (NEWS).

Over the years, a standardized technique was developed for performing what we might today call "traditional" ultrasonic nonlinearity measurements. The technique has been embodied in commercial off-the-shelf measurement systems such as the Ritec RAM-5000 [19]. A continuous-wave (CW) or tone burst signal is applied to the material under test. A high-power amplifier provides the large signal levels required to observe nonlinearity. Narrowband transducers made from piezoelectric materials such as quartz or lithium niobate and cut to resonate at the frequencies of interest are used for excitation and detection. Measurement is performed with a heterodyne or superheterodyne receiver that downconverts the desired receive frequency to DC. The amplitude of the selected frequency is determined by integrating the quadrature phase components of the downconverted signal. By using this method, maximum frequency selectivity can be obtained, and measurements can be performed at the fundamental frequency and various harmonics to quantitatively determine harmonic generation in the medium under test. In recent years, the heterodyne receiver has been commonly replaced by a digitizer and Fourier transform algorithm to measure the spectrum directly, e.g. Delsanto et al. [8].

Two specific modern techniques, widely used in non-destructive testing applications, are worthy of note. Nonlinear Resonant Ultrasound Spectroscopy (NRUS) involves observing nonlinear behaviors in a sample excited at an acoustic resonance [1]. These include shifts in resonant frequency, harmonic generation, and damping characteristics. The second modern non-destructive testing

technique is known as Nonlinear Wave Modulation Spectroscopy (NWMS) [2]. NWMS involves the application of CW signals or tone bursts of different frequencies to the sample. Nonlinearity in the medium causes multiplicative effects that are observed as generated sum and difference frequency signals in the sample. This method dates back to the work of Rollins et al. [20], who studied phonon-phonon scattering as a function of the angles and frequencies of the incoming and scattered phonons. NWMS has an advantage over measurements of harmonic generation because interference from nonlinearity in the equipment can be more easily rejected. If the signal generation circuitry, amplification circuitry, and transducers for the two excitation frequencies are separated, nonlinear mixing in the excitation signal is eliminated. Therefore, if NWMS is used properly, nonlinearity in the excitation equipment becomes irrelevant and the components of the sound wave at $f_1 + f_2$ and $f_1 - f_2$ can only come from nonlinearity in the medium.

Much recent interest has developed in the exotic nonlinear phenomena that appear when extremely high amplitude excitation is applied. Solodov [24], [25] has been studying contact acoustic nonlinearity (CAN) and the instability and chaos that can result from very high amplitude excitation given such a nonlinearity.

2.3 Our technique

We build upon the standard experimental technique for measurement of harmonic generation. The basis of our equipment is the measurement system by Ritec [19] that was built to perform conventional harmonic generation and

mixing measurements. However, we use it in a dramatically different way. We are interested in making broadband, time-resolved measurements. Instead of using narrowband resonance transducers, we use broadband damped transducers. These have much lower efficiency, but allow us to make measurements over a wide range of frequencies. Instead of using a single continuous wave or tone burst, we apply a tone burst at a wide range of frequencies and use an algorithm to build up composite waveforms showing the linear and second harmonic responses of the medium. We use the same superheterodyne receiver and integrator as in the standard technique, but we apply it in a much more advanced way and collect far more information. This information is condensed into readily interpretable time-resolved waveforms for the fundamental frequency and the second harmonic. We extract maximum information from the sample, but bound the complexity by limiting ourselves to quadratic nonlinearity. We thereby obtain time-resolved waveforms that have the potential to dramatically improve the state-of-the-art in nondestructive testing.

2.4 Other phenomena

It is important to mention in closing that there are many nonlinear acoustic phenomena other than just those mentioned above. There is an entire field of study related to shock waves and sonic booms, and the concomitant specialized experimental apparatus. Nonlinear mixing phenomena generate highly directed sound waves at the sum and difference frequencies. This has uses both in audio applications such as the "Audio Spotlight" [18] and in medical applications where "harmonic imaging" with directed beams has dramatically improved spatial resolution and image quality [28].

CHAPTER 3

A MODEL OF A WEAKLY NONLINEAR MEDIUM

Recall the cracked bell of the previous chapter. We applied an excitation with frequencies 440 Hz and 8000 Hz. Then we observed the response of the bell, and identified a large number of frequencies present:

- The applied frequencies: 440 Hz and 8000 Hz
- Harmonics of 440 Hz: 880, 1320, and 1740 Hz (second harmonic, third harmonic and fourth harmonic).
- Harmonics of 8000 Hz: 16000, 24000, and 32000 Hz (second harmonic, third harmonic and fourth harmonic).
- Mixing frequencies: 8000+440 Hz and 8000-440 Hz.

A very simple analysis can explain the frequencies that appear. Suppose the cracked bell has a quadratic (squaring) property. We apply 440 Hz and 8000 Hz superimposed:

$$\cos(2\pi 8000t) + \cos(2\pi 440t) \tag{3.1}$$

Then the quadratic behavior is:

$$\left[\cos(2\pi 8000t) + \cos(2\pi 440t)\right]^2 \tag{3.2}$$

or

$$\cos^2(2\pi 8000t) + 2\cos(2\pi 8000t)\cos(2\pi 440t) + \cos^2(2\pi 440t) \tag{3.3}$$

or, using the identities $\cos^2(\theta) = \frac{1}{2} + \frac{1}{2}\cos(2\theta)$ and

$2\cos(\alpha)\cos(\beta) = \cos(\alpha+\beta) + \cos(\alpha-\beta)$,

$$1 + \frac{1}{2}\cos(2\pi 16000t) + \cos(2\pi(8000+440)t) + \cos(2\pi(8000-440)t) + \frac{1}{2}\cos(2\pi 880t) \tag{3.4}$$

We find that squaring an applied (440 Hz + 8000 Hz) signal gives us the additional frequencies 880, 16000, and 8000 ± 440 Hz. This most simple analysis, which assumes only that the nonlinearity has the effect of multiplying the wave by itself, predicts most of the observed frequencies (the higher harmonics come from cubing, or higher, effects). So we hypothesize that perhaps a Taylor expansion will allow us to model the dynamic response of the bell.

3.1 Impulse response

We will start by proposing a model for the nonlinear acoustic medium. This will be a simplistic model; it will apply only when amplitudes are small enough that behavior is weakly nonlinear. We will further limit it by explicitly ignoring many potentially significant terms to limit the required information that must be collected. Nevertheless, this model provides a mathematical justification for our measurement, and provides a basis for interpreting the measured waveforms.

Linear systems are usually modeled by their impulse response (Green's function). Impulse response precisely characterizes a time-invariant linear system. It is time-resolved, broadband, and easy to analyze. Our approach to modeling weakly nonlinear systems will be analogous. We will define the *second harmonic*

impulse response to go along with the *linear impulse response*. We might also define third and higher order responses, but we will not discuss those here.

3.2 Volterra expansion

Consider a weakly nonlinear system that maps a function $f(t)$ to $g(t)$. If we make various assumptions about continuity and differentiability of the mapping, we can write the Taylor Series for this mapping, discretized in time by subscripts:

$$\hat{g}_i = \left.\frac{\partial g_i}{\partial f_j}\right|_{f=0} f_j + \frac{1}{2!}\left.\frac{\partial^2 g_i}{\partial f_j \partial f_k}\right|_{f=0} f_j f_k + \frac{1}{3!}\left.\frac{\partial^3 g_i}{\partial f_j \partial f_k \partial f_l}\right|_{f=0} f_j f_k f_l + \ldots \quad (3.5)$$

$$\left(\begin{array}{c} \text{sum over} \\ \\ j, k, l, \text{ etc.} \end{array} \right)$$

This particular Taylor series is also known as a discrete-time Volterra expansion [23], [29]. We begin our approximation of the output of the map at time i, $\hat{g}_i$, by evaluating the partial derivative of g_i with respect to the input of the map at some other time j, f_j, and multiplying the evaluated partial derivative by the actual value of the input of the map at time j. This gives us the linearized dependence of the approximated g_i on f_j. To combine the linearized effect of f on the approximated g_i at different times j, we must sum over possible values of j. Of course, each time i in g must be considered independently. This gives us a matrix of constants $\frac{\partial g_i}{\partial f_j}$. The quadratic term relates g_i to each possible combination $f_j f_k$, and is summed over all j and k. Higher terms can be analyzed similarly. It can be readily confirmed that eq. 3.5 is indeed the Taylor series for the $f \rightarrow g$ mapping by evaluating the first few derivatives of eq. 3.5 at $f = 0$. Those derivatives match the actual derivatives of g with respect to f. This is demonstrated in appendix A.1.

3.3 Reduced Volterra expansion/Taylor series

A linearized (impulse response) model includes only the first term $\frac{\partial g_i}{\partial f_j} f_j$ of the above Volterra expansion. For our nonlinear model, we will use the first term, plus selected parts of the second. In particular, we would like to reduce the second term from n^3 coefficients to n^2 coefficients. We can do this by assuming that the signal never interacts nonlinearly with a time shifted version of itself. That is, we assume $\frac{\partial^2 g_i}{\partial f_j \partial f_k}\Big| = 0$ for $j \neq k$. We keep only the terms for which $j = k$. Now we only have two subscripts and therefore n^2 coefficients. Thus, our model $\hat{g}_i$ for g_i is:

$$\hat{g}_i = \left.\frac{\partial g_i}{\partial f_j}\right|_{f=0} f_j \; + \; \frac{1}{2!} \left.\frac{\partial^2 g_i}{\partial f_j^2}\right|_{f=0} f_j^2 \tag{3.6}$$

This model ignores all third and higher order terms. It also ignores second order terms involving time-shifted self interaction. We are assuming all nonlinear interaction to be of the form $(f(t))^2$, and not of the form $f(t)f(t+\Delta)$. This assumption is of the utmost importance. It both makes this method viable, and restricts the domain of problems to which this method can be applied. If the physical nonlinearity to be measured comes from interaction of the wave with itself at the same time, then this method may be applicable.

3.4 Representation of the model as a convolution

$\left.\frac{\partial g_i}{\partial f_j}\right|_{f=0}$ is a set of constant numbers with two indices. We can write it as a matrix A_{ij}. Similarly, $\left.\frac{1}{2!}\frac{\partial^2 g_i}{\partial f_j^2}\right|_{f=0}$ can be denoted as a matrix B_{ij}. Now our model can be

rewritten using matrix notation:

$$\hat{g}_i = A_{ij} f_j + B_{ij} f_j^2 \qquad \text{sum over j} \tag{3.7}$$

or in vectorized notation,

$$\hat{g} = \mathbf{A} f + \mathbf{B} f^2 \tag{3.8}$$

We assume our nonlinear system is time-independent. That is, if we run our experiment in an hour, or tomorrow, we will get the same results as running it now. Therefore our model is not consistent with slow dynamics or hysteresis behavior such as that described by Ten Cate and Shankland [26]. Since we assume our system to be time-independent, the matrices A_{ij} and B_{ij} must have the form of convolutions.

Let us return to continuous time, now denoting our convolutions as $\mathbf{A}$ and $\mathbf{B}$. Our modeled signal can be written as:

$$\hat{g} = \mathbf{A} \otimes f(t) + \mathbf{B} \otimes f^2(t) \tag{3.9}$$

We will refer to the convolutions $\mathbf{A}$ and $\mathbf{B}$ as the *linear impulse response* and *second harmonic impulse response* respectively. $\mathbf{A}$ characterizes the linear (small signal) behavior of the system, and $\mathbf{B}$ characterizes quadratic nonlinearity of the system. $\mathbf{A}$ is also sometimes referred to as the *first order Volterra kernel* of the system, and $\mathbf{B}$ is a reduced version of the *second order Volterra kernel* of the system.

3.5 Restrictions of the model

The model restricts the domain of nonlinear behavior we can analyze. Using only the first two terms of the Taylor expansion limits us to the analysis of weakly nonlinear phenomena and limited excitation amplitude (in addition, the continuity, differentiability, and convergence requirements of the Taylor series may be violated in the case of strongly nonlinear phenomena or very large excitation amplitude). Ignoring time-shifted self interaction restricts us from being able to consider situations in which an acoustic wave is nonlinearly interacting with a delayed version of itself. For example, it restricts us from using this method to study dispersive media. It might also be a problem for situations in which the excitation burst is long enough that echos superimpose, but experimentally this does not appear to be a problem. The model also assumes that there is no convolution or filtering of the signal before the nonlinearity of the medium is encountered. In practice, the signal is always filtered by at least the transducer impulse response before it reaches the acoustic nonlinearity. Our method can generally be meaningfully applied to a nonlinear medium provided time-shifted self interaction is not expected and the excitation is small enough that the nonlinearity is weak.

3.6 Amplitude sensitivity

An important observation to draw from this model is the amplitude sensitivity of the nonlinearity. The nonlinear term of equation 3.9 is proportional to the square of the applied signal f. This means that measured nonlinearity will be a strong

function of input amplitude; doubling the input amplitude will quadruple the nonlinearity. This observation is especially critical from an experimental standpoint, since it implies that for weak phenomena, excitation amplitude is critical. Further, it warns that if too powerful a signal is applied, there is the risk of violating the 'weak nonlinearity' assumptions of the model.

3.7 Weak nonlinearity

In the above analysis, we have referred to weak nonlinearity without discussing exactly what we mean by "weak". If one propagates a tone burst through a linear medium, the measured burst is a filtered version of the excitation burst. If a very small amount of nonlinearity is added to the medium, then a small spectral image will appear at $2f$ in the measured signal. As the nonlinearity is increased, the amplitude of the $2f$ harmonic will increase, and spectral images will also appear at higher harmonics – $3f$, $4f$, etc. As the nonlinearity (or equivalently the excitation amplitude) is increased further, shock waves develop. At still higher levels of nonlinearity the behavior becomes very complicated and difficult to analyze. We define weak nonlinearity as the second case outlined above: A small component at $2f$ is detected in the measured signal. Our derivations rely on this assumption. Nevertheless, we suspect that our method is applicable even in the presence of higher harmonics, provided the amplitude of the harmonic signals remain small relative to the fundamental.

CHAPTER 4

MEASUREMENT ALGORITHM

4.1 Mathematical justification

We would like to characterize a nonlinear medium by applying the model of the previous chapter, equation 3.9:

$$\hat{g} = \mathbf{A} \otimes f(t) + \mathbf{B} \otimes f^2(t) \tag{3.9}$$

To characterize the medium, we must evaluate the convolutions $\mathbf{A}$ and $\mathbf{B}$. We start by remarking that in equation 3.9, $\mathbf{A}$ is linear in $f(t)$, and $\mathbf{B}$ is linear in $f^2(t)$. If we want to use the tools of linearity to help in our measurement of $\mathbf{A}$ and $\mathbf{B}$, all we need to do is perform the measurement so that the terms of equation 3.9 are distinguished. Let us attempt to apply a signal $s(t)$ for $f(t)$, such that $\mathbf{A}$ and $\mathbf{B}$ can be distinguished in the measurement. If the measurement is performed by a receiver filter $\mathbf{R}$, then the receiver signal is:

$$\mathbf{A} \otimes s(t) \otimes \mathbf{R} + \mathbf{B} \otimes s^2(t) \otimes \mathbf{R} \tag{4.1}$$

The criterion of distinguishing $\mathbf{A}$ from $\mathbf{B}$ is then equivalent to selecting $s(t)$ and $\mathbf{R}$ such that $s(t) \otimes \mathbf{R}$ is non-zero while $s^2(t) \otimes \mathbf{R}$ is (approximately) zero or vice-versa. That is, we can distinguish $\mathbf{A}$ and $\mathbf{B}$ if we can distinguish the terms in equation 4.1. $s(t)$ and $\mathbf{R}$ need to be constructed so that we can distinguish these terms.

We will apply tone bursts for $s(t)$ and the impulse response of $\mathbf{R}$. $s^2(t)$ will be a frequency-doubled tone burst (+ DC). When we convolve with $\mathbf{R}$, frequencies not present in the impulse response of $\mathbf{R}$ become zero. By selecting the frequency of the receiver filter $\mathbf{R}$ to be f or $2f$, we can select either of the two terms in eq. 4.1.

If $s(t)$ is a modulated tone burst and $\mathbf{R}$ has an impulse response similar to $s(-t)$, then $s^2(t) \otimes \mathbf{R}$ is approximately zero and we extract only the first term and obtain information about $\mathbf{A}$. On the other hand, if $\mathbf{R}$ has an impulse response similar to $s^2(-t)$, then $s(t) \otimes \mathbf{R}$ is approximately zero and we extract only the second term and obtain information about $\mathbf{B}$. That is, with a modulated tone burst $s(t)$, we can selectively probe $\mathbf{A}$ with $s(t) \otimes s(-t)$ or $\mathbf{B}$ with $s^2(t) \otimes s^2(-t)$ by selecting the frequency of $\mathbf{R}$. We use narrowband probing signals so that it is possible to distinguish $\mathbf{A}$ and $\mathbf{B}$.

Recalling from above that equation 3.9 is linear in $\mathbf{A}$ and $\mathbf{B}$, the principle of superposition can be applied. We can construct thousands of different tone bursts $s(t) \otimes s(-t)$ and superimpose them to effectively probe $\mathbf{A}$ with $\sum_i s_i(t) \otimes s_i(-t)$. Given a wide frequency band and small frequency steps, $\sum_i s_i(t) \otimes s_i(-t)$ will be very similar to a bandlimited delta function (a sinc function) because its components are autocorrelations and hence zero phase. Similarly, we can measure $\mathbf{B}$ with $\sum_i s_i^2(t) \otimes s_i^2(-t)$ by performing a series of measurements and adding the results. Because we use very narrowband signals for $s_i(t)$, we must probe at a large number of frequencies in order to obtain a flat frequency response for the composite signal.

To recap, we measure $\mathbf{A}$ and $\mathbf{B}$ by applying a large number of narrowband bursts at different frequencies, then applying linear superposition. This is graphically illustrated in figure 4.1. The bursts add in the time domain to a bandlimited impulse, or in the frequency domain to a uniform response within the selected frequency band.

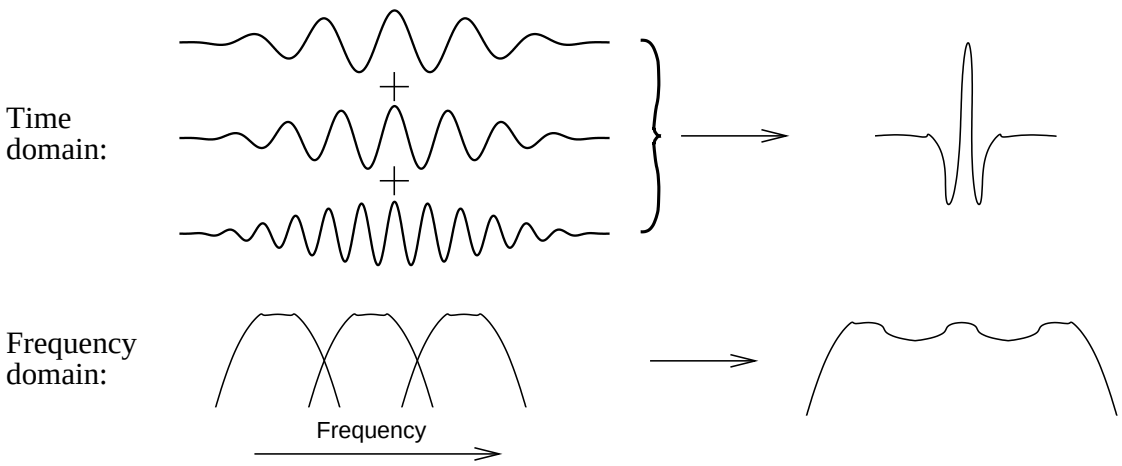

Figure 4.1: Construction of a broadband impulse from a series of narrowband bursts.

4.2 Measurement procedure

Our procedure for measuring linear and second harmonic impulse responses follows:

1. **Apply burst**

   Apply a modulated tone burst $s(t) = W_1(t)\cos(\omega t)$. (Fig. 4.2a).

2. **Measure acoustic response**

   The response of the nonlinear system is $\mathbf{A} \otimes s(t)$ plus the frequency doubled term $\mathbf{B} \otimes s^2(t)$. (Fig. 4.2b).

3. **Correlate with** $W_2\cos(n\omega t)$

   We convolve (correlate in negative time) the measured response with the receiver filter $\mathbf{R}$. The impulse response of $\mathbf{R}$ is a modulated burst $r(t) = W_2(t)\cos(-n\omega t)$. This process extracts the nth (1st or 2nd) term of Eq. 4.1. (Fig. 4.2c).

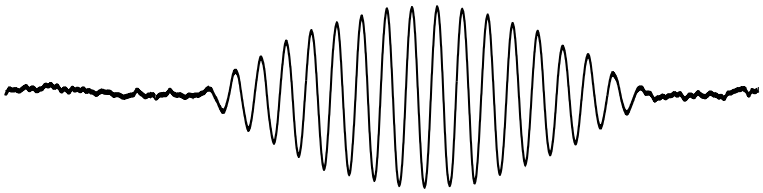

(a) High−power excitation burst

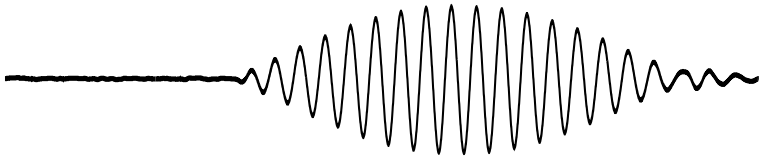

(b) Signal measured by receiver

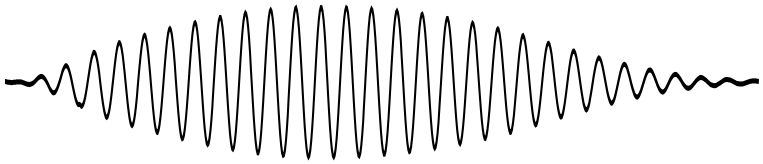

(c) Received signal correlated with receiver burst $W_2\cos(n\omega t)$

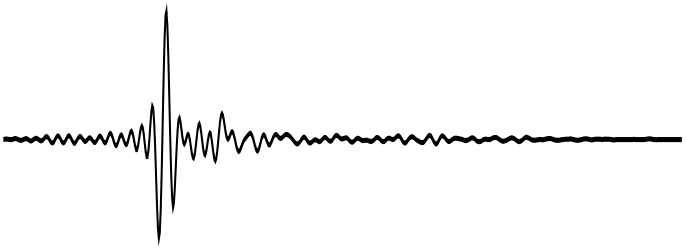

(d) Result from adding correlated bursts from all frequencies

Figure 4.2: Burst processing demonstration.

4. **Add correlated waveforms from bursts at a wide range of frequencies**

   Repeating the above steps for many different frequencies, and adding the correlated waveforms (from Fig. 4.2c) gives our estimate of **A** or **B**. (Fig. 4.2d).

4.3 Interference and Error

The measurement algorithm described above appears reasonably simple and straightforward, but there are numerous potential sources of interference and error. Some come from imperfections or non-ideal behavior in equipment. Other interference comes from the algorithm itself.

4.3.1 Non-ideal behavior

The goal of the measurements is to extract information about the material being tested. In our model, we assume that we apply a perfect tone burst to the material, and measure it perfectly. Of course this is impossible. The excitation waveform always has some amount of harmonic distortion, generated by the waveform generator or amplifier, which will propagate linearly through the medium and be measured as part of the second harmonic impulse response. The transducers themselves can generate harmonics within the piezoelectric crystal, or at the interface with the wear plate or the couplant to the sample. The power amplifier for the excitation can generate switching transients that could be measured as a valid signal. The receiver transducer and electronics also can

generate harmonic distortion that will be measured as part of the second harmonic impulse response. Careful design can minimize, but not eliminate, these phenomena, which we will address further in chapter 5. Conventional measurements of harmonic generation phenomena use resonant narrowband transducers and multipole filters to reduce the effect of harmonic distortion in the equipment. Such workarounds are unavailable to us because we must make broadband measurements.

4.3.2 Algorithmic interference

The measurement algorithm described above relies on two flawed assumptions: That a series of tone bursts at different frequencies adds to a bandlimited impulse (sinc function), and that tone bursts at f and $2f$ are orthogonal.

Consider adding the tone bursts in the frequency domain, as illustrated at the bottom of figure 4.1. The sum always has some periodicity in frequency Δf. In the time domain, this will appear as a periodicity of $1/\Delta f$. Our measured time-domain response will have images of the measured signal at $t = \pm\frac{1}{\Delta f}$. While these images cannot be removed[1], the amplitude of these images can be reduced by minimizing the frequency spacing between bursts. In addition, dithering the frequency spacing spreads the images over a large range in time so that they appear as random noise that can be averaged away. Transforming the error to noise in this fashion entirely eliminates this form of error as a practical concern.

The other flawed assumption is that the f and $2f$ bursts are orthogonal. Let us

[1]One might think that it is possible to eliminate these images by adjusting the burst envelope. This was tried, but has not worked well in experiments so far.

look at the frequency components of a raised-cosine burst of duration Δt (time domain):

$$\left[\frac{1}{2}+\frac{1}{2}\cos\left(\frac{2\pi}{\Delta t}t\right)\right]\left[u\left(t+\frac{\Delta t}{2}\right)-u\left(t-\frac{\Delta t}{2}\right)\right]\cos(2\pi f t) \tag{4.2}$$

The primary frequency components present are $\pm f$ and $\pm f \pm 1/\Delta t$. These frequencies are convolved in frequency with the sinc function that is the Fourier transform of the boxcar $u\left(t+\frac{\Delta t}{2}\right)-u\left(t-\frac{\Delta t}{2}\right)$. Each of these frequencies is thereby spread out over all frequency-space according to (at worst) the sinc function of width $1/\Delta t$.

Suppose a measurement is performed on a linear medium. A burst such as that of eq. 4.2 is applied to the medium. To measure the second harmonic impulse response, a frequency doubled burst is convolved in time – multiplied in frequency – with the measured signal. The overlap of the sidebands of the frequency doubled burst with the original leads to interference that is measured as part of the second harmonic impulse response. The bursts at f and $2f$ are not entirely orthogonal, and the nonorthogonality causes interference.

Experimentally, it has been determined that this interference manifests itself as a pair of pulses in the second harmonic impulse response that are separated in time by exactly half the burst width. The absence of the dual-pulse signature implies that f vs. $2f$ interference is not present. We have used several techniques to reduce the interference. Using longer bursts reduces interference because a larger Δt narrows the sinc function. Using an optimal window for the excitation and/or receiver bursts also reduces the interference.

4.4 Relation to other techniques

4.4.1 Conventional CW or burst harmonic generation measurements

In materials testing, the traditional approach to the measurement of nonlinear phenomena has been the use of narrowband CW or burst harmonic generation measurements. It has been widely described, such as by Ryan et al. [22] and Breazeale [6]. Unfortunately, these methods give either no time resolution or poor time resolution. Our approach is an extension of traditional harmonic generation measurements that provides much better time resolution by using a broadband signal.

However, our method has several disadvantages when compared to traditional methods. One is that our method requires much more precise and powerful measurement hardware. Traditional methods use high-efficiency narrowband resonance transducers. We must use low-efficiency damped broadband transducers, and therefore in general must be able to apply much higher power in order to observe nonlinear phenomena. Another disadvantage is that our method requires isolation of harmonic frequencies from the fundamental that is independent of the frequency in use. Traditional methods can use multiple filters and narrowband transducers to improve harmonic isolation.

4.4.2 "Vibroseis" method

Our method is related to the Vibroseis method [30] which is commonly used in seismic studies as an alternative to the use of explosive sources. In the Vibroseis method, a heavy truck consisting primarily of a hydraulic jack is vibrated up and down in a frequency sweep. Signals recorded at geophones are cross-correlated with the frequency sweep. The resulting waveform is equivalent to that recorded by the geophone, given an impulse source at the location of the truck. In our method, a series of tone bursts at different frequencies is used in place of a frequency sweep. The processing is essentially the same – the measured waveform for each burst is cross-correlated – except we allow second harmonic measurement by cross correlating with the frequency doubled burst. Also, our use of a series of tone bursts rather than a long frequency sweep allows the use of a single transducer in pulse-echo mode with a T/R switch. Nonlinearity and harmonic generation are sometimes observed in Vibroseis surveys. Because the nonlinearity typically comes from near-surface effects it is undesirable and treated as noise.

CHAPTER 5

IMPLEMENTATION OF THE MEASUREMENT ALGORITHM

5.1 Implementation with an analog signal processing system

Analog systems have long promised and delivered signal processing devices with excellent frequency selectivity for minimum interference. The archetypical analog signal processing device is the heterodyne radio receiver. Analog radios have long been able to isolate a particular frequency band, even in the presence of strong interference elsewhere in the spectrum. Isolation of such a band is exactly the requirement for the measurement of a weak nonlinear component of a strong signal. For our experiments, we obtained a Ritec RAM-5000 system [19], containing two high power signal generators/amplifiers and an analog superheterodyne receiver unit.

The goal of the analog receiver system is to convolve/correlate the received signal with a receiver filter $W_2 \cos(n\omega t)$ as in step 3 of the measurement algorithm. The RAM-5000 uses a superheterodyne receiver circuit to minimize (coherent) harmonic interference. The received signal passes first through a pre-amplifier, then to an analog multiplier. It is multiplied in time by a harmonic wave at the desired receive frequency plus 20 MHz. This shifts signals at the receive frequency to 20 MHz. The shifted signal is then filtered and multiplied by 20 MHz signals at quadrature phase (0° and 90°), shifting the signal to the baseband while retaining phase information. The RAM-5000 contains gated

integrators for the quadrature components (denoted 'real' and 'imaginary') and 16 bit ADC's on the integrator outputs.

We are trying to measure the cross correlation of the measured signal $m(t)$ with $W_2 \cos(n\omega t)$. That is,

$$\int_{-\infty}^{\infty} W_2(\tau - t) \cos(n\omega(\tau - t)) m(\tau) d\tau$$

(t indexes the cross-correlation, while τ denotes measurement time) If we let $u = \tau - t$:

$$\int_{-\infty}^{\infty} W_2(u) \cos(n\omega(u)) m(u + t) du$$

If we restrict $W_2(t)$ to being a boxcar function of width l (i.e. 1 for $-l/2 < t < l/2$, 0 otherwise), then:

$$\int_{u=-l/2}^{l/2} \cos(n\omega(u)) m(u + t) du$$

Returning to t and τ:

$$\int_{\tau=t-l/2}^{t+l/2} \cos(n\omega\tau - n\omega t) m(\tau) d\tau \tag{5.1}$$

Equation 5.1 is the expression we need to measure in order to determine one point in the cross-correlation of $m(t)$ with $W_2 \cos(n\omega t)$.

When we use the RAM-5000 receiver, the actual effect of the superheterodyne multipliers is to measure (ignoring filtering):

$$(\cos(n\omega\tau) + isin(n\omega\tau)) m(\tau)$$

or in complex notation:

$$e^{in\omega\tau} m(\tau)$$

We would like to translate this into the expression to be measured, eq. 5.1. If we select the integrator gates to be at $t - l/2$ and $t + l/2$, then we measure

$$\int_{\tau=t-l/2}^{t+l/2} e^{in\omega\tau} m(\tau) d\tau$$

The result of this integral – real and imaginary parts – is what the RAM-5000 measures and is recorded into the computer using the 16 bit DAC's. If these values are multiplied by $e^{-n\omega t}$ then the result is:

$$\int_{\tau=t-l/2}^{t+l/2} e^{in\omega\tau - in\omega t} m(\tau) d\tau$$

If the real part is taken, then we have:

$$\int_{\tau=t-l/2}^{t+l/2} \cos(n\omega\tau - n\omega t) m(\tau) d\tau$$

This is the same as eq. 5.1, hence we can measure one time sample of the desired cross-correlation by using the analog heterodyne receiver in the RAM-5000. The entire cross-correlation can be recorded by repeating with different values of t, over the time range in which a waveform is desired.

5.2 Experimental techniques

5.2.1 System design

The overall hardware design is shown in figure 5.1, and a photograph of the apparatus can be seen in figure 5.2. The RAM-5000 was rewired internally to support an external modulation input. An HP 33120 arbitrary waveform generator was used to provide the modulation envelope of the excitation bursts. One piezoelectric transducer transforms the electrical signals from the high power

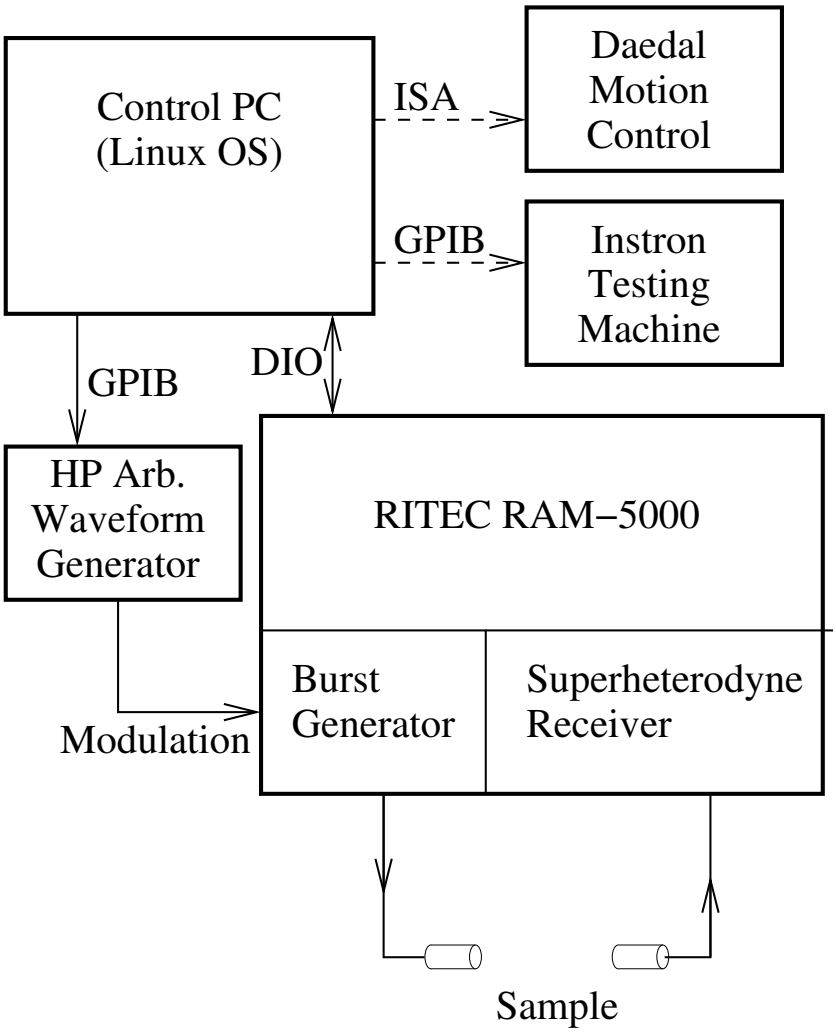

Figure 5.1: Diagram of the hardware used for the time-resolved nonlinear method.

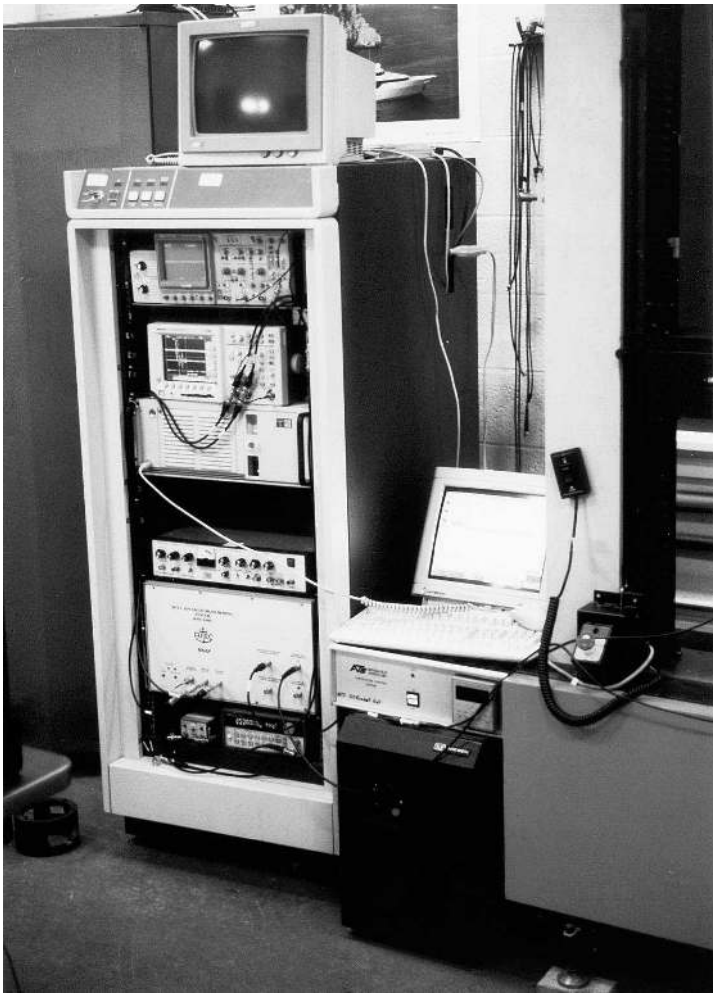

Figure 5.2: Photograph of the hardware used to carry out the time-resolved nonlinear measurements. The RAM-5000 system is the large device near the bottom of the rack.

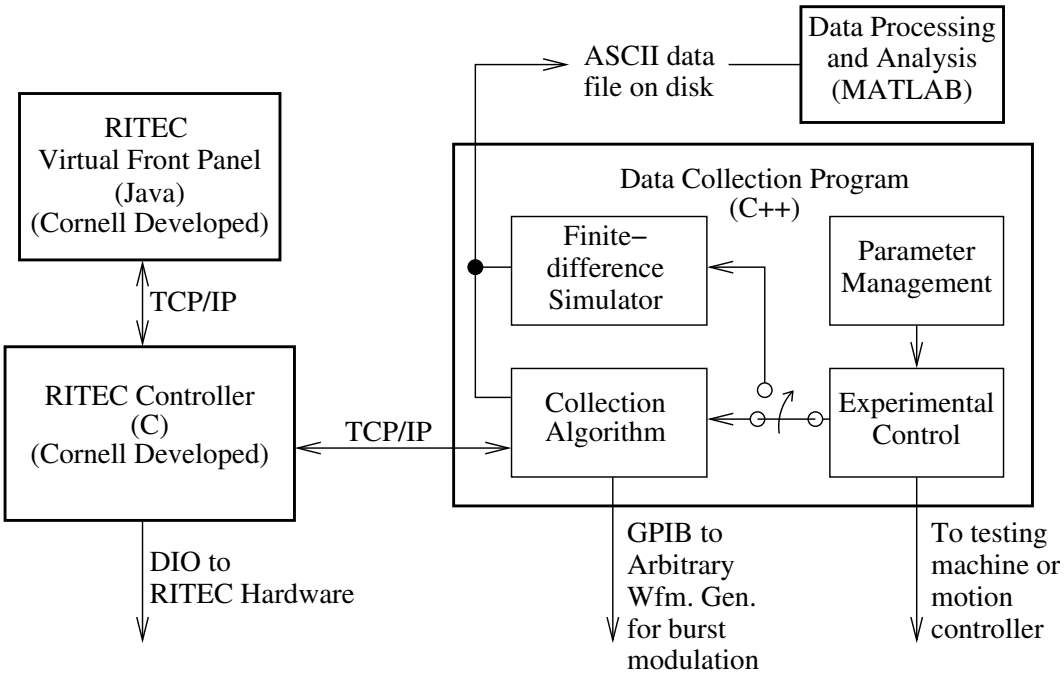

Figure 5.3: Diagram of the software used for the time-resolved nonlinear method.

amplifier in the RAM-5000 into ultrasonic waves within the specimen. Another transducer measures the ultrasonic vibrations in the sample and transmits an electrical signal to the receiver. A Daedal motion control unit and Instron testing machine were also connected under computer control as appropriate for a particular experiment.

The challenging part of the implementation of this project was the software. The software had to implement the measurement algorithm described here. It had to be flexible enough to allow for algorithmic experimentation without requiring rewrites or leading to spaghetti code. Some method of handling the large number of parameters was required. The software had to be reconfigurable for different experiments; one experiment might require controlling a motion control device, while the next might use an Instron testing machine and load cell. Moreover, the

software had to take into account the various idiosyncrasies of the different hardware devices. For example, the signal generators in the RAM-5000 reference their initial phase from the amplifier gate (turn-on) time. However, the phase must be preset one trigger early. Since the gate time is dithered randomly to average away switching transients, the phase must be reprogrammed with every trigger, with the appropriate information corresponding to the succeeding trigger. Needless to say, idiosyncrasies such as this dramatically increase the complexity of the control software.

Figure 5.3 shows the overall software architecture. The "Experimental Control" module is replaceable and different for different experiments. It accepts parameters from the standardized parameter management routines and passes the relevant parameters on to the collection algorithm. A finite difference simulator, discussed in detail in chapter 6, can be used in place of the measurement hardware. The simulator is engineered to share as much code as possible with the collection algorithm, so that the simulation is as similar as possible to the actual experiments. The RAM-5000 hardware is controlled over TCP/IP using firmware that we developed, as discussed in appendix B. The measured data from experiments – samples of the downconverted cross-correlation waveforms – are recorded in an ASCII data file. The data file is post-processed using Matlab scripts to obtain the composite time-resolved waveforms.

5.2.2 Frequency step dithering

There are some subtle points about the measurement system that bear mention. One major issue is the flatness of the frequency response of the applied wavelet –

the sum of the applied bursts. This issue was discussed in section 4.3.2. The problem is that the sum of applied bursts inherently has frequency domain periodicity corresponding to the frequency step spacing. The frequency domain periodicity corresponds to shifted impulse images in the time domain. Minimizing the frequency step size Δf helps reduce the amplitude of these images. Selecting a modulation window such that the frequency domain signals add to very nearly a flat line could also help. To eliminate these images completely, we add a dither to the frequency step size. The dither spreads the energy of these impulse images throughout the time and frequency domains as noise.

5.2.3 Amplifier gate time dithering

It is most critical in the measurement to reduce and eliminate coherent noise. While incoherent noise can be averaged out, coherent noise is more difficult to eliminate. The high power gated amplifier used for excitation generates broadband switching transients when it switches on and off immediately before and immediately after a burst. These transients, unless eliminated, will generate coherent noise in the excitation signal. When the signal is measured, they will translate into phase error. We dither the gated amplifier turn on and turn off times, typically by $\pm 2\mu s$, so that phase error from the switching transients will average to zero over all the measurements for a particular frequency.

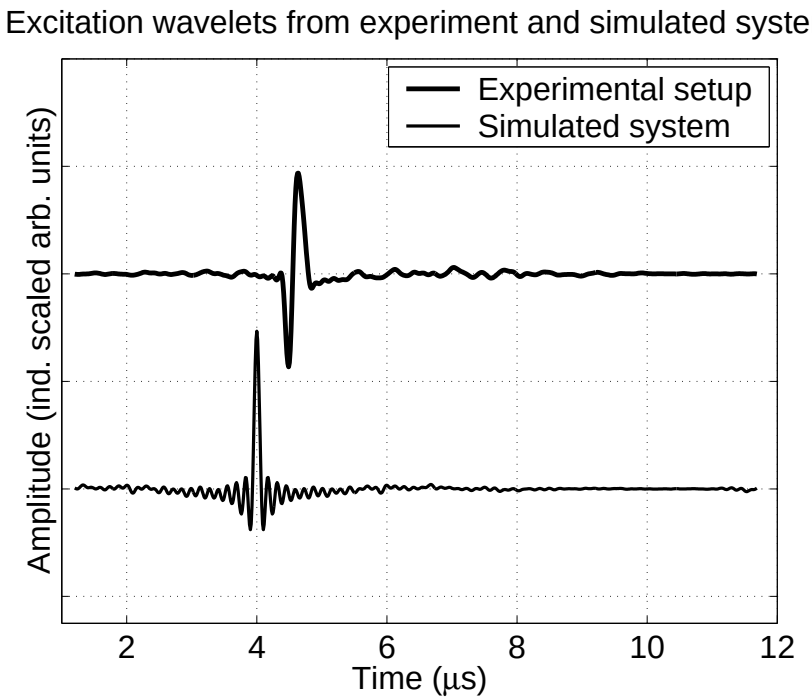

Figure 5.4: Experimental and simulated wavelets used to probe medium.

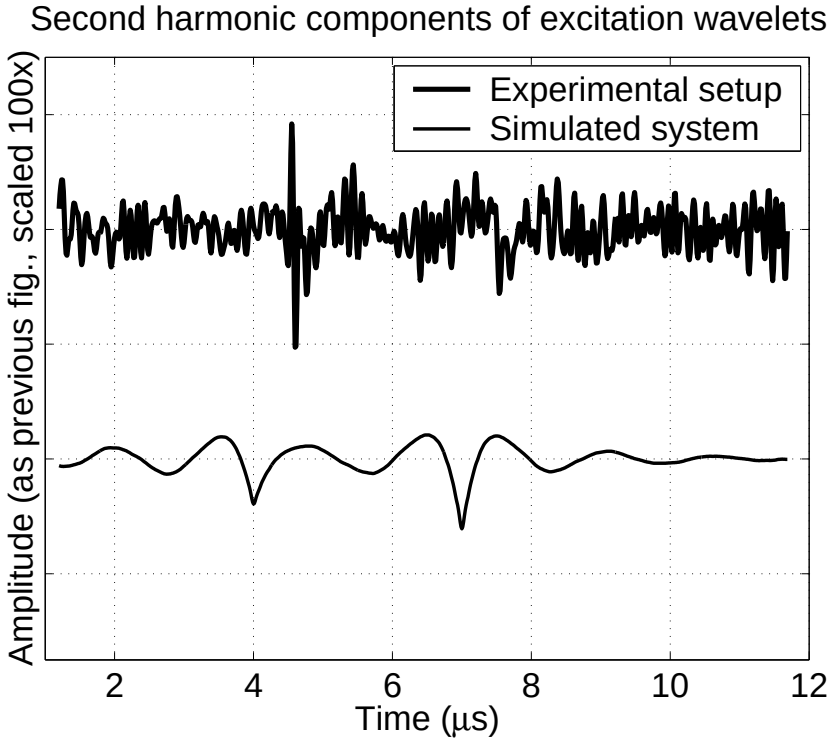

Figure 5.5: Second harmonic content of wavelets used to probe medium.

5.3 Typical wavelet

In our experimental configuration, one input of the measurement system is always used to monitor the excitation. This allows us to measure the wavelet (bandlimited impulse) we use to probe the system, using the same superposition algorithm as for the measured data. Both the linear impulse response and the second harmonic impulse response of this wavelet can be measured. While the second harmonic impulse response of this wavelet would ideally be zero, because of the interference and error phenomena described above in sect. 4.3, a second harmonic impulse response signal is always measured. By evaluating this signal, it is possible to quantify the interference/error/noise level of the second harmonic signal relative to the linear signal. Figure 5.4 shows typical excitation wavelets from experiment and simulation from the water experiment that will be discussed in chapter 7. The excitation time t_0 is 4 μs. The experimental signal appears 500 ns late primarily due to group delay in the receiver filters. Figure 5.5 shows the measured second harmonic impulse response, scaled up by a factor of 100, of the wavelets of figure 5.4. The second harmonic content of the composite wavelet bounds the sensitivity with which second harmonic signals can be detected. The dual pulse signature of algorithmic interference that was discussed in section 4.3.2 can be seen clearly in the second harmonic content of the simulated wavelet at $t = 4$ μs and $t = 7$ μs. The spacing of the interference pulses is 3 μs, or exactly half the burst width of 6 μs. The same dual pulse signature can be seen among the noise of the experimental waveform at $t = 4.5$ μs and $t = 7.5$ μs.

5.4 Implementation with a digital signal processing system (proposed)

While the above analog system demonstrated the viability of our measurement system, it ultimately proved inadequate for performing the rapid high-SNR measurements that would be needed to demonstrate the utility of this measurement system for the non-destructive testing of materials. The signal generators/amplifiers have turned out moderately well, but the receiver unit has been a disappointment. In particular, the receiver unit uses noisy amplifiers and has problems with signal leakage from other parts of the system. In the one characteristic for which the analog system should excel – extraction of a weak signal buried in a strong signal – it fails miserably. A signal just 40 dB – 1% – below the peak is already buried in noise by the front-end amplifier! Even an 8-bit digital system can have a lower noise level. While an optimal analog measurement system might in theory work better for this application, a digital system might be more practical for future work. Nevertheless, we have used this Ritec analog system for the proof-of-concept measurements in this dissertation.

Several particular limitations of the analog equipment were identified:

- **Noisy analog electronics** The Ritec analog front-end is very noisy, with an SNR no better than 40 dB. This broadband noise carries through all stages, although the SNR is improved by the narrowband detection and filtering. Other stages may also have serious noise problems, but the front-end noise seems to dominate.

- **Inefficient performance** Because the superheterodyne receiver can only

measure one point in the cross-correlation per trigger and other limitations, more than 100 triggers are required per frequency. Ideally, only 1 trigger is required per frequency.

- **Harmonic distortion in the frequency synthesizer** The Ritec frequency synthesizer uses 8 bit digital synthesis and generates harmonics internally at -40 to -50 dB. These harmonics are then amplified along with the fundamental and during measurement are indistinguishable from harmonic generation within the sample.

To address these issues, an upgraded system using digital synthesis and digital heterodyne detection was designed. In this system, a 12 bit DAC card, such as GAGE CompuGen 1100 [10], would be used as a signal source as input to the Ritec gated amplifiers. This would reduce harmonic distortion to -65 dB or better. A noise shaping algorithm could further be used to improve precision and reduce harmonic distortion. Acoustic waveforms would be recorded with a high-speed high-precision ADC (e.g. GAGE CompuScope 12100 [10]). The recorded waveforms would be digitally cross-correlated with the actual excitation waveform, and with the square of the actual excitation waveform. This would provide lower noise measurement (-65 dB or better dynamic range/SNR) and much faster measurement times. With digital measurement, only one trigger is required per frequency to capture and correlate the entire waveform. This would lead to 100x faster performance. While the benefits of a digital measurement system are clear, financial support for it was never obtained and it was never implemented.

5.5 Limiting factors of the measurement

The most fundamental limitation of the measurement system is time – the time required to measure a composite waveform. Most of the factors involved in measurement quality reduce in some way to the time required for the measurement. With the current analog system, typical measurement times range from 15 minutes to 4 hours depending upon the settings used. The most important factor in measurement quality is the dynamic range of the receiver. Because harmonic signals tend to be buried many dB below the fundamental, the receiver must be capable of avoiding clipping the fundamental signal without burying the second harmonic signal in noise. Increased measurement time allows more averaging, which decreases the effective noise level of the receiver. Other factors involved in measurement quality also translate into longer measurement time. For example, reducing "f vs. 2f" interference requires using longer tone bursts. Because the duty cycle of the gated amplifier is limited, a lower repetition frequency must be used, and the total measurement time is proportionally longer. Because the practical utility of a system such as this is fundamentally linked to measurement time, reducing it is of the utmost importance. A digital system such as that described in section 5.4 would go a long way toward this goal. The digital system can measure an entire cross-correlation in one trigger, while the analog system is limited to one of 50-100 points in the correlation per trigger.

Some limiting factors of the measurement cannot be corrected by increasing measurement time. Reducing them instead requires improving equipment or modifying the measurement algorithm or implementation. Coherent noise or harmonic distortion coming from the excitation or receiver circuitry cannot be

reduced by using a longer measurement time, nor can harmonic generation within the transducers or coupling media. However, while not all sources of noise or error translate into longer measurement time requirements, the quality of measurement with the current system translates directly to the time permitted for the measurement.

CHAPTER 6

SIMULATION

6.1 A tool for verification

A simulation environment for weakly nonlinear media was developed and integrated into the data collection system. The idea is that a computational model for the experimental system can be constructed. Then the collection algorithm and processing routines can operate on either physical hardware or the simulation environment. This provides an opportunity to confirm and verify that the system behaves as expected on a model environment. By carefully analyzing the simulation, we can gain important insights into both the behavior of the measurement algorithm and the underlying physics of the simulated experiments. We can also use the simulation as an idealized platform on which to study the interference and error limitations of our measurement algorithm, such as those discussed in section 4.3 and observed in section 5.3 and figures 5.4 and 5.5. Finally, the simulation allows us to directly compare experimental and simulated results, and to use this as a tool for evaluating both the measurement system and the experiment itself.

6.2 Finite difference model

We model a 1-dimensional nonlinear medium with a discrete series of masses and nonlinear springs as shown in figure 6.1 with a dashpot at the boundary to

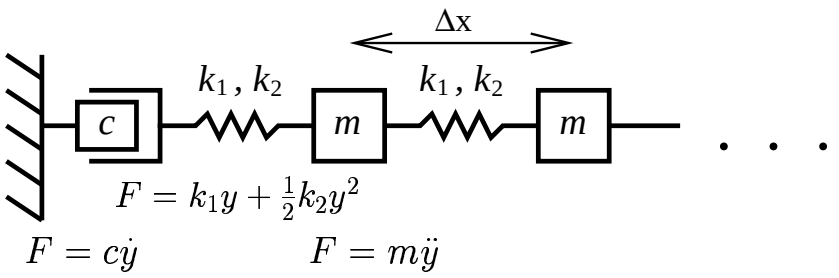

Figure 6.1: Finite difference model of a nonlinear medium.

provide an absorptive end condition. This model (ignoring boundaries) is expressed by the discrete time difference equation (see appendix A.2):

$$\frac{m}{(\Delta t)^2}(y_x^{t+\Delta t} - 2y_x^t + y_x^{t-\Delta t}) = \tag{6.1}$$
$$k_1(y_{x+\Delta x}^t + y_{x-\Delta x}^t - 2y_x^t) + \frac{k_2}{2}(y_{x+\Delta x}^t - y_{x-\Delta x}^t)(y_{x+\Delta x}^t + y_{x-\Delta x}^t - 2y_x^t)$$

In the limit as Δx and Δt approach zero, equation 6.1 becomes the nonlinear one-dimensional PDE (appendix A.3):

$$\frac{\partial^2 y}{\partial t^2} = \frac{E_1}{\rho}\frac{\partial^2 y}{\partial x^2} + 2\frac{E_2}{\rho}\frac{\partial y}{\partial x}\frac{\partial^2 y}{\partial x^2} \tag{6.2}$$

where $E_1 = \frac{k_1 \Delta x}{A}$, $E_2 = \frac{k_2 (\Delta x)^2}{4A}$, and $\rho = \frac{m}{A \Delta x}$.

The nonlinear wave equation, eq. 6.2, can also be derived from $F = ma$ and the nonlinear elastic constitutive law (appendix A.4):

$$\sigma = E_1 \epsilon + E_2 \epsilon^2 \tag{6.3}$$

Hence, our difference equation (eq. 6.1) with sufficiently small Δx and Δt can be used to model a continuous one-dimensional system with the simple nonlinear constitutive law of eq. 6.3. This difference equation contains exactly one term $y_x^{t+\Delta t}$ referencing the future, and can therefore be iterated in time to solve the PDE given initial conditions and boundary conditions.

6.3 Convergence issues and $\frac{\Delta x}{\Delta t}$

Obviously for the difference equation (6.1) to converge, Δx and Δt must approach zero. Properties of the convergence turn out to be highly dependent upon the *ratio* $\frac{\Delta x}{\Delta t}$. Based on an analysis of the linear equation, we will conclude that $\frac{\Delta x}{\Delta t}$ should be slightly larger than the small signal wavespeed.

If we linearize the difference equation (6.1) and let $c = \sqrt{\frac{E_1}{\rho}}$, and $c_\Delta = \frac{\Delta x}{\Delta t}$, the equation reduces to (appendix A.5):

$$y_x^{t+\Delta t} - 2y_x^t + y_x^{t-\Delta t} = \frac{c^2}{c_\Delta^2}(y_{x+\Delta x}^t + y_{x-\Delta x}^t - 2y_x^t) \tag{6.4}$$

A 2-D Z-transform – or equivalently substituting $y = e^{ik(x-c_{ph}t)}$ – gives (appendix A.5):

$$\frac{c_\Delta}{c} = \frac{\sin(\omega c_\Delta \Delta t/2c_{ph})}{\sin(\omega \Delta t/2)} \tag{6.5}$$

This can be nondimensionalized by defining the step size factor $r_{step} = \frac{c_\Delta}{c}$, the wavespeed ratio $r_{speed} = \frac{c_{ph}}{c}$, and the oversampling factor $r_{over} = \frac{f_s}{2f_{meas}} = \frac{\pi}{\omega \Delta t}$. Therefore,

$$r_{step} = \frac{\sin(\frac{\pi r_{step}}{2r_{speed}r_{over}})}{\sin(\frac{\pi}{2r_{over}})} \tag{6.6}$$

This can be solved for r_{speed}:

$$r_{speed} = \frac{\pi r_{step}}{2r_{over}\arcsin[r_{step}\sin(\frac{\pi}{2r_{over}})]} \tag{6.7}$$

In particular, r_{speed} is a function of r_{step} and r_{over}! That is, the discretized wave equation has become dispersive. Since in the linearized model, there should be no dispersion, it makes sense to select step sizes Δx and Δt to minimize the dispersion. We can plot r_{speed} as a function of r_{step} and r_{over} to investigate the

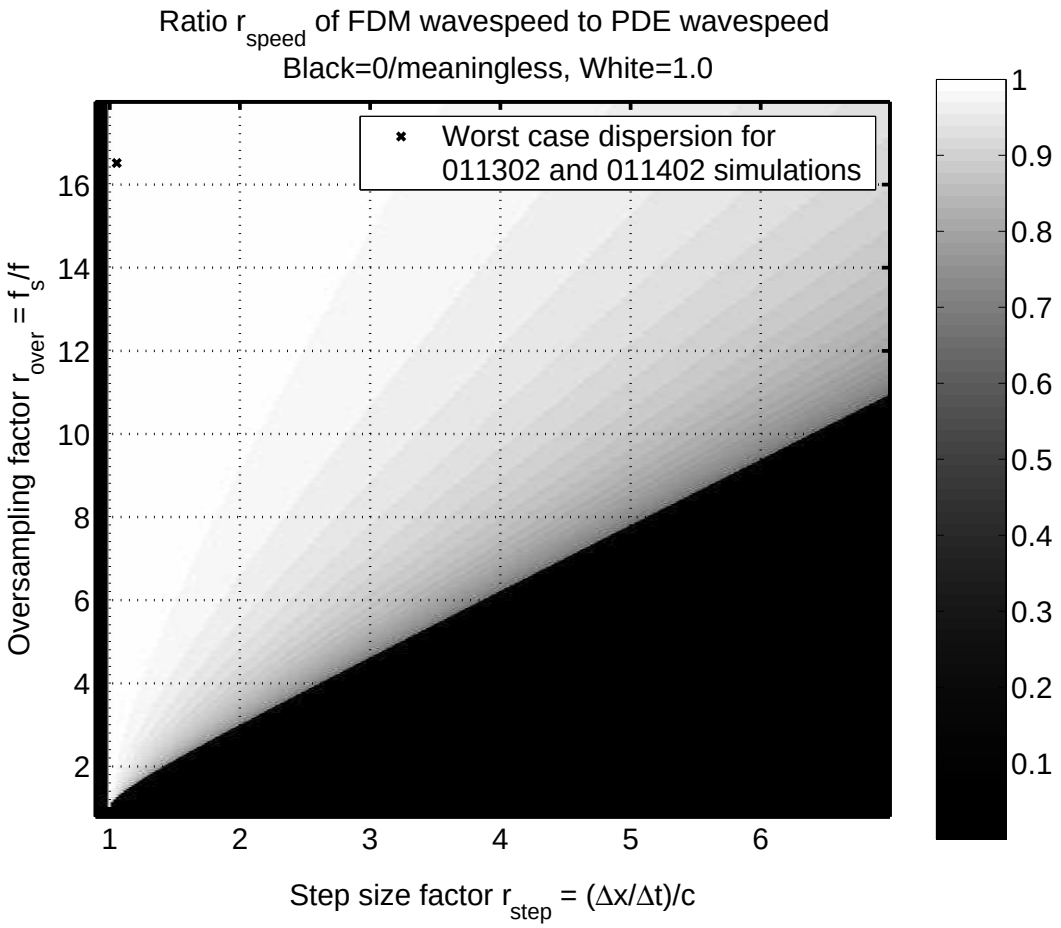

Figure 6.2: Dispersion of the finite difference model as a function of Δx and Δt.

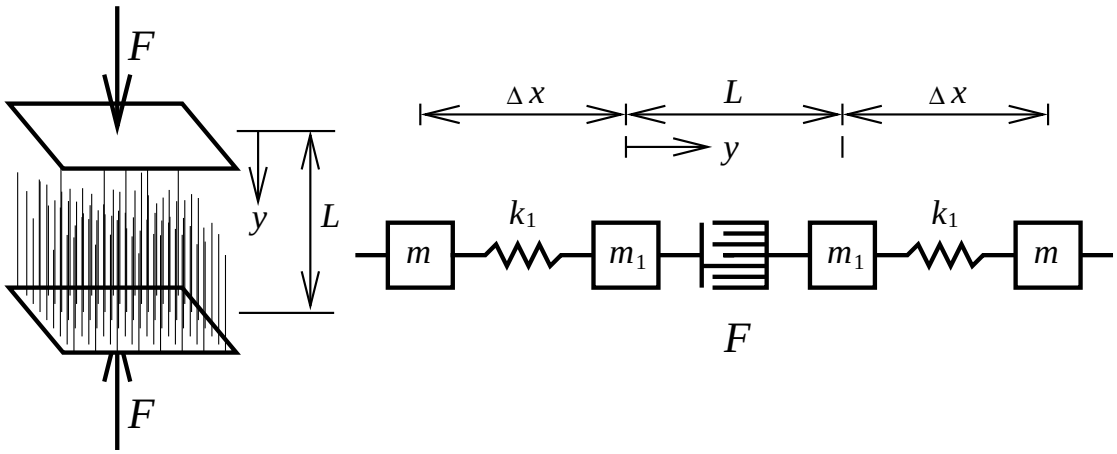

Figure 6.3: Finite difference modeling of a dry contact or crack.

dispersion. Figure 6.2 shows r_{speed} (grayscale) as a function of r_{step} and r_{over}, from eq. 6.7. Since the simulation should exhibit no dispersion ($r_{speed} = 1.0$), we can select the simulation parameters r_{step} and r_{over} from fig. 6.2 to minimize dispersion. From the figure, we clearly want $r_{step} = 1 + \epsilon$ (that is, $\frac{\Delta x}{\Delta t}$ slightly larger than c) and r_{over} as large as possible. The worst case parameters for the water simulation experiment that will be discussed in chapter 7 are marked with a cross on figure 6.2.

6.4 Model of a crack or dry contact

We use a dry contact between two pieces of material as an experimental model for a crack. In order to properly simulate such an experiment, an elastic model for the crack or dry contact is needed. We use an array of pins (compressive springs) between rigid plates as shown in figure 6.3 to model the dry contact. The equilibrium pin length is a normally distributed random quantity. This

model is inserted between two masses in place of a spring in the finite difference model. Given a displacement from nominal length y, the force F given by this model is (appendix A.6):

$$F = \frac{yAE}{2L} \operatorname{erfc}\left(\frac{y}{\sqrt{2}\sigma}\right) - \frac{\sigma AE}{L\sqrt{2\pi}} e^{-\frac{y^2}{2\sigma^2}} \tag{6.8}$$

where σ is the standard deviation of the pin length and L is the amount of physical length required by the dry contact model. In our simulation, we let $L = \Delta x$ and define a dimensionless parameter $\alpha = \frac{\sigma}{L}$ that describes the roughness or randomness of the surface. Putting this all together, we obtain a relatively simple stress-strain relation:

$$\text{stress} = \frac{1}{2}\epsilon E \operatorname{erfc}\left(\frac{\epsilon}{\sqrt{2}\alpha}\right) + \frac{E\alpha}{\sqrt{2\pi}} e^{-\frac{\epsilon^2}{2\alpha^2}} \tag{6.9}$$

To model the nonlinearity, we insert equation 6.9 into the finite difference model eq. 6.1 at a point, replacing a spring. Unfortunately, because the width of the nonlinearity is defined by the spatial step size Δx, the behavior of the simulation is not independent of Δx. Therefore convergence testing of the simulation by reducing Δx and Δt cannot be performed. Instead we must rely on convergence testing from a system with no nonlinearity.

The stress-strain relation, eq. 6.9, for $E = 70\ GPa$, $\alpha = .045$, and $\Delta x = 28.5\mu m$ is shown in figure 6.4. As one would expect for a dry contact between two aluminum specimens, it is linear with a modulus of 70 GPa under large compression, but exhibits no stiffness under tension.

6.5 Integration with data collection

In order to be useful and relevant to the measurements discussed here, it must be possible to apply the same series of tone bursts to the simulator as to the

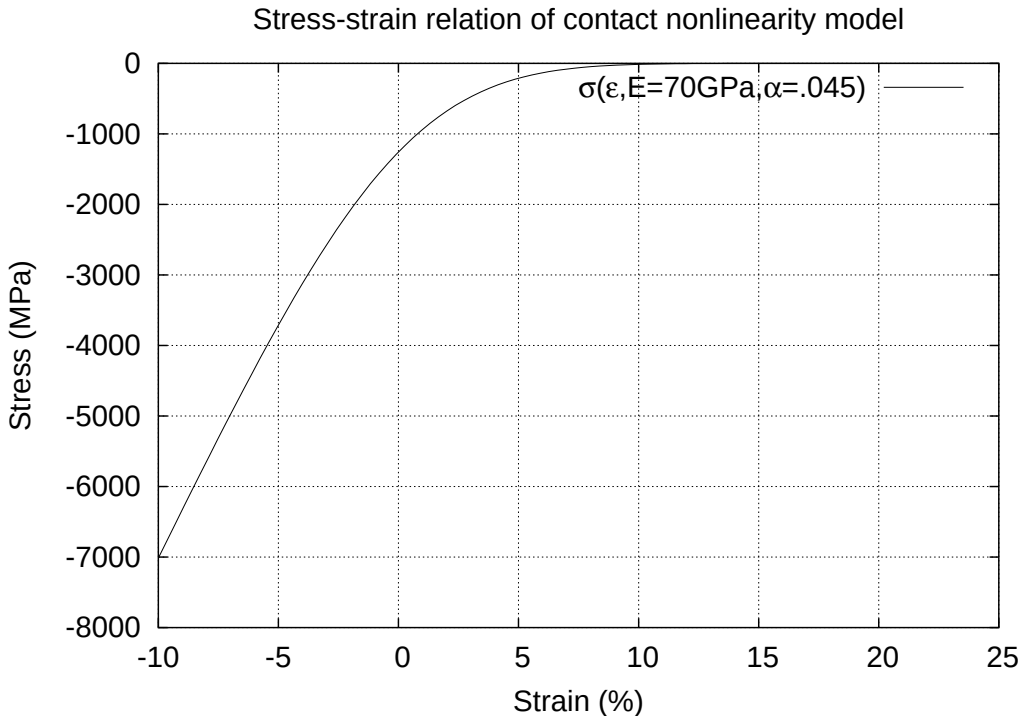

Figure 6.4: Stress-strain relation of nonlinear contact model.

physical sample, and then to perform the analog processing of the Ritec receiver unit, and finally to simulate the normal data collection procedure. For this reason, the simulator has been integrated into the data collection program. A single parameter selects whether a real experiment is to be performed or a simulation should be run. All other settings are shared by the simulator and data collection routines. Much of the same data collection code is used. The data file formats are the same. All of the post-processing is identical. This way, the simulator is very useful for testing data collection and processing codes and procedures as well as being an experimental tool.

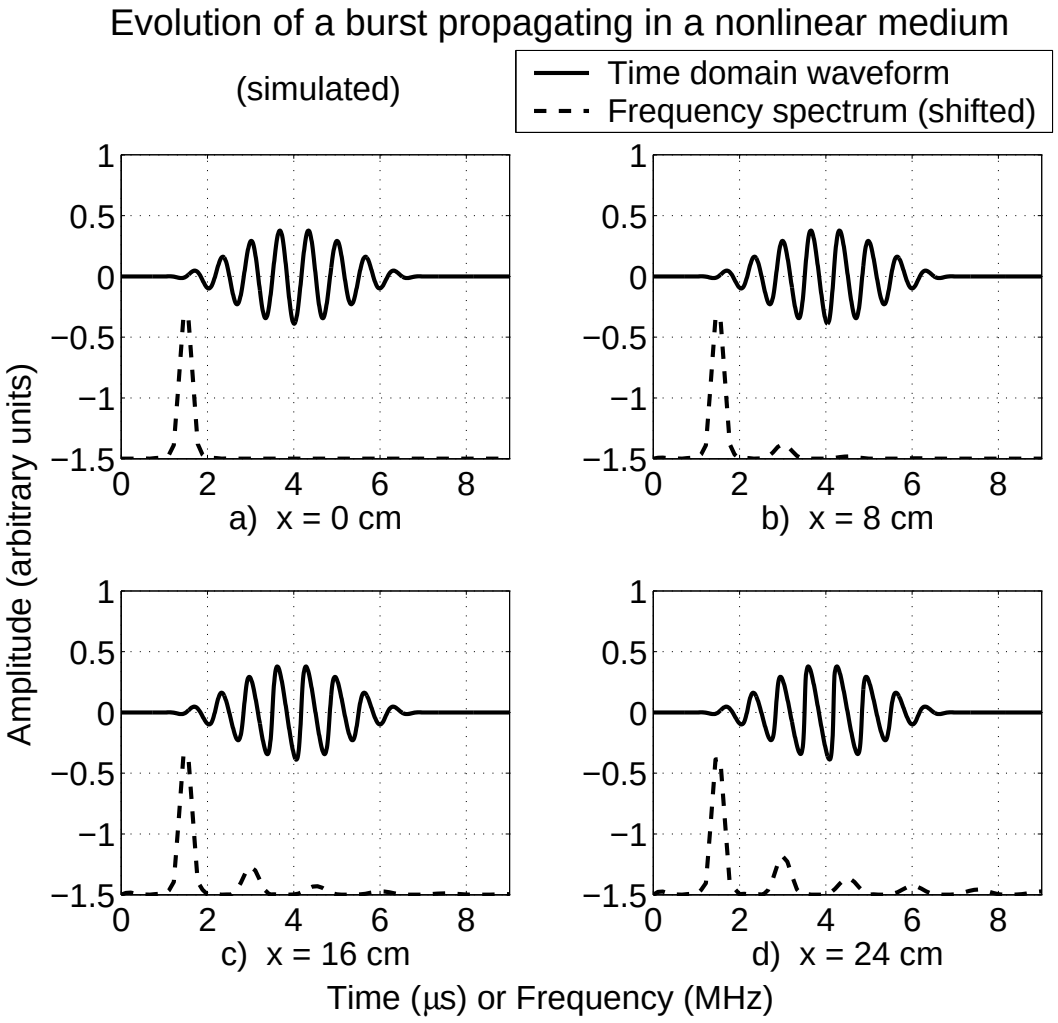

Figure 6.5: Demonstration of simulated wave propagation in a nonlinear medium.

6.6 Nonlinear wave propagation demonstration

While specific results relevant to the time-resolved nonlinear process will be discussed along with the corresponding experiments, here we demonstrate the finite difference simulation by propagating a tone burst through a nonlinear medium. The excitation is a $f = 1.5MHz$ tone burst in a $6\mu s$ raised-cosine envelope, applied as an external force to the end of the simulated nonlinear medium. The response of the medium is measured by a velocity sensor with a variable position. The evolution of the tone burst can be seen in figure 6.5. Figure 6.5 (a) shows the burst at the excitation point in the time and frequency domains. Figure 6.5 (b), (c), and (d) show the burst after propagating through 8 cm, 16 cm, and 24 cm of the nonlinear medium of equation 6.3 respectively.

Fig. 6.5a shows no nonlinearity. There is a signal only at the excitation frequency. After a short distance of propagation, a small amount of nonlinear self-interaction has occurred, leading to the second harmonic shown in Fig. 6.5b. More propagation distance leads to higher order harmonics and larger amplitudes of the harmonics, as can be seen in Figs 6.5c and 6.5d. Propagation over larger distances could lead to shock generation and more exotic nonlinear phenomena.

CHAPTER 7

EXPERIMENT: HARMONIC GENERATION IN WATER

7.1 Experimental configuration

As a simple test of the time-resolved nonlinear method, we chose to apply the method to measure harmonic generation in water. The nonlinear acoustic acoustic behavior of water is well known and well characterized, e.g. Beyer [3] and Krassilnikov et al. [16]. Figure 7.1 gives the results from Krassilnikov et al. [16] showing second harmonic generation (not time-resolved) for water and transformer oil. Curves 1, 2, and 3 correspond to harmonic generation in water for excitation amplitudes of 500 V, 1 kV, and 2 kV respectively applied to a piezoelectric transducer at 1.5 MHz. Curve 4 (and the right hand voltage scale) corresponds to 2 kV excitation at 1.5 MHz in transformer oil. In a simple weakly nonlinear medium, we would expect harmonic generation to be proportional to the distance traveled, as shown in curve 1 of figure 7.1. Curves 2 and 3 do not show this beyond 20 cm. Most likely the criterion of weak nonlinearity is being violated by these experiments, because otherwise these results are inconsistent with with well established and verified theory ([17] and see below).

We demonstrated a similar experiment using the time-resolved method. In this experiment, separate source and receiver immersion transducers were used to measure an ultrasonic wave propagating in the water. The axial separation between source and receiver was varied using a motion-control system, as shown in figure 7.2. We measured the linear and second harmonic impulse responses at each separation for source frequencies from 0.86 to 7.25 MHz, in steps averaging

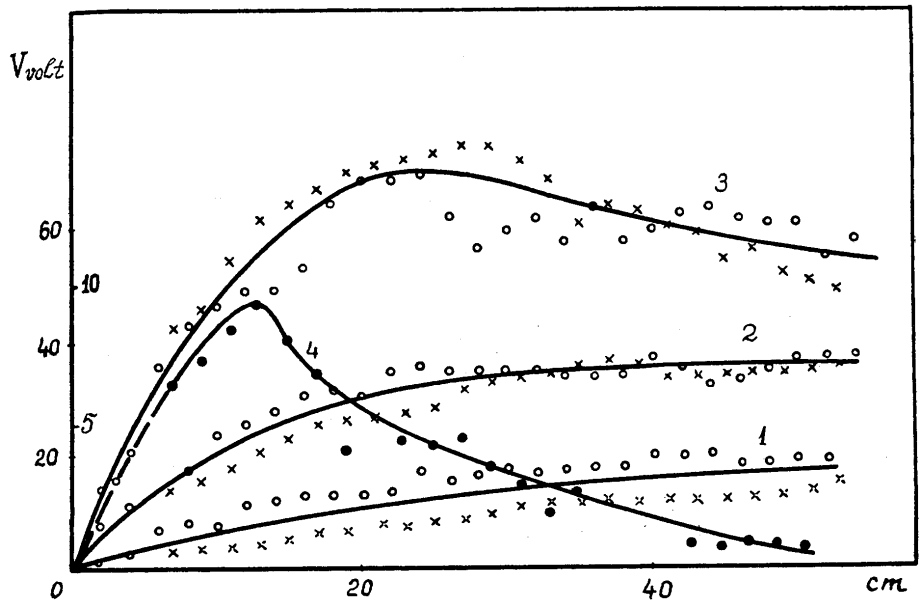

Figure 7.1: Results from Krassilnikov et al. [16] showing harmonic generation at 3 MHz from 1.5 MHz ultrasound propagating in water and transformer oil.

Curves 1, 2, and 3 correspond to propagation in water at 500 V, 1 kV, and 2 kV excitation levels respectively. Curve 4 corresponds to propagation in transformer oil with 2 kV excitation. The left scale on the voltage axis corresponds to the water experiments; the right scale corresponds to the transformer oil experiments. $\times$ and $\circ$ correspond to different measurement methods.

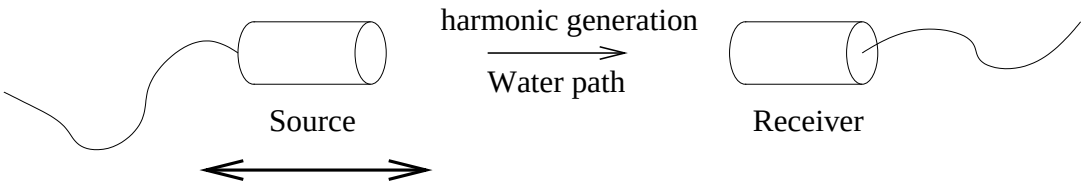

Figure 7.2: Illustration of experiment showing harmonic generation in water.

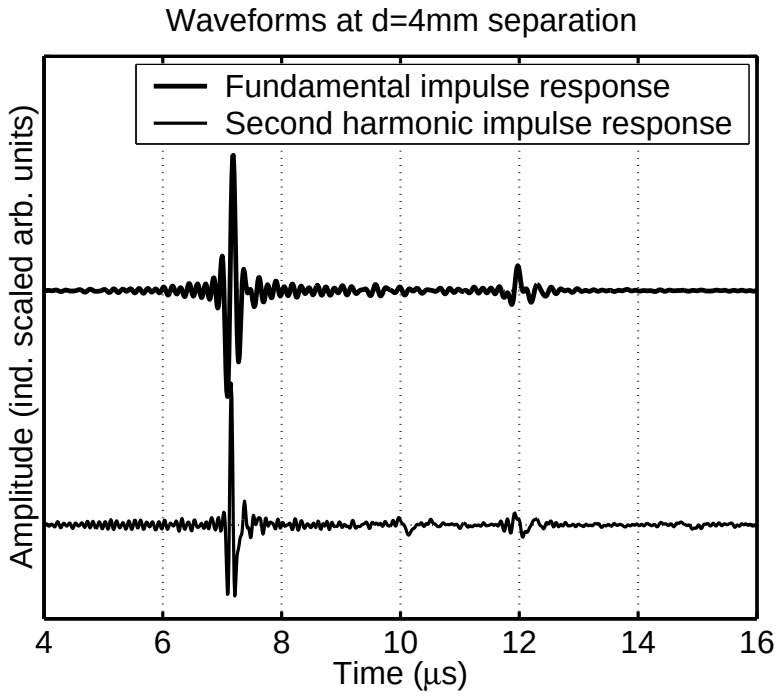

Figure 7.3: Sample waveforms, harmonic generation in water, propagation distance=4 mm.

38.5 kHz (fundamental) or 19.2 kHz (second harmonic). Off-the-shelf commercial immersion transducers were used for this experiment (3 MHz Ultran L50-3 source and 5 MHz Panametrics V310 receiver). Since wave propagation over a longer distance would tend to give more harmonic generation, we expected the amplitude of the second harmonic to increase proportionally with distance. In contrast, we expected the amplitude of the linear pulse to remain approximately constant.

7.2 Experimental results

Two experiments were performed, at relative excitation amplitudes 1.00 and 2.49. Figure 7.3 shows sample waveforms corresponding to $d = 4\ mm$ separation, 2.49

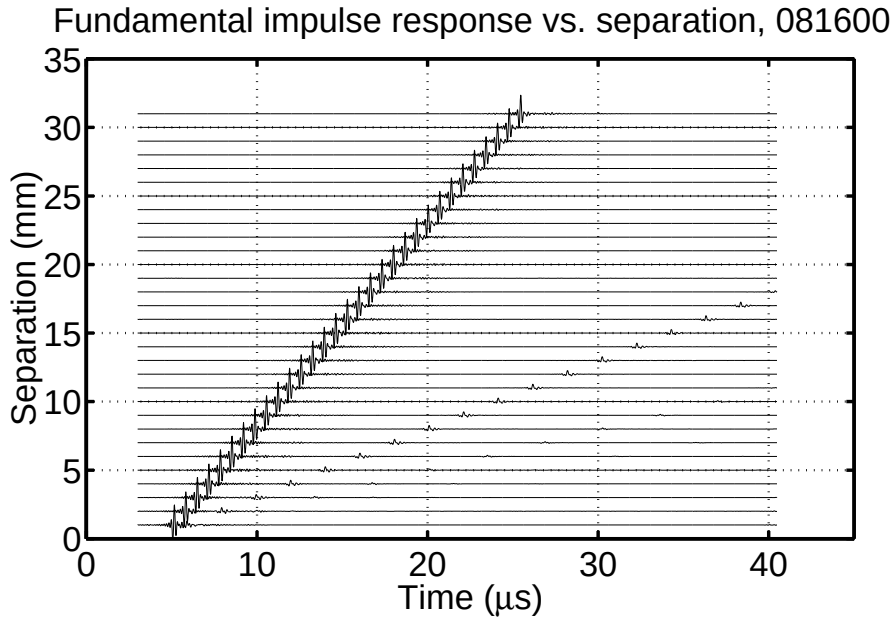

Figure 7.4: Linear (fundamental) impulse response waveforms as source-receiver distance is varied.

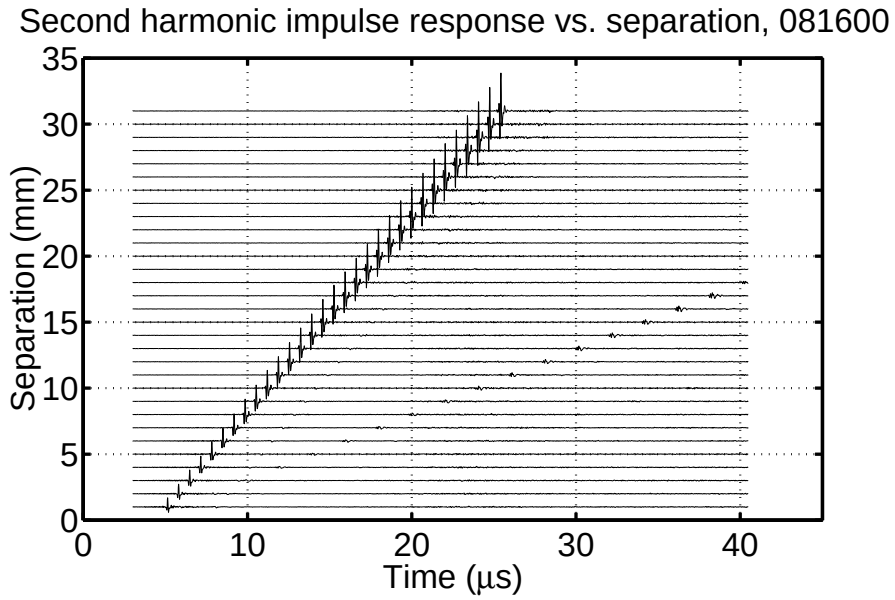

Figure 7.5: Second harmonic impulse response waveforms as source-receiver distance is varied.

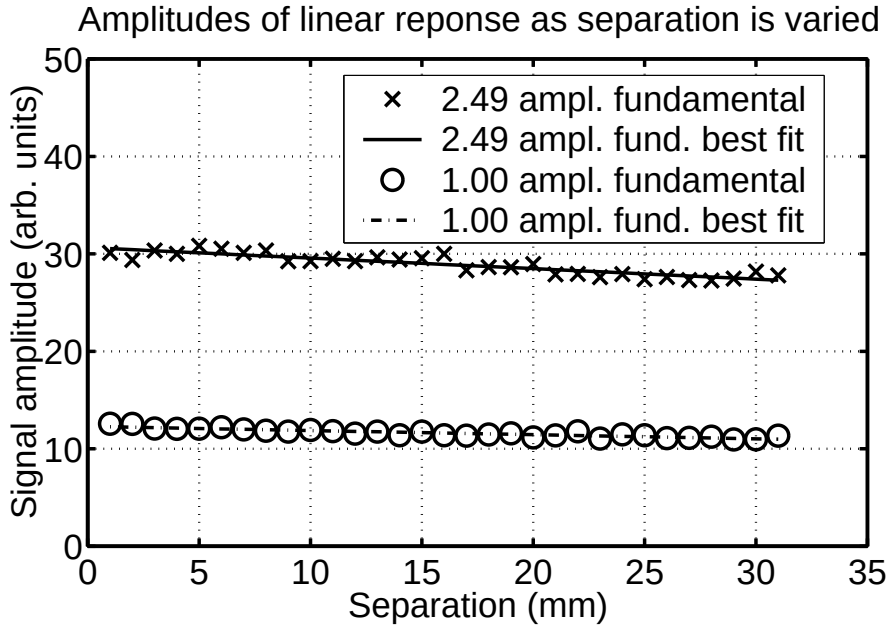

Figure 7.6: Linear (fundamental) impulse response amplitude as source-receiver distance is varied.

Two experiments were run at relative excitation amplitudes of 2.49 and 1.00.

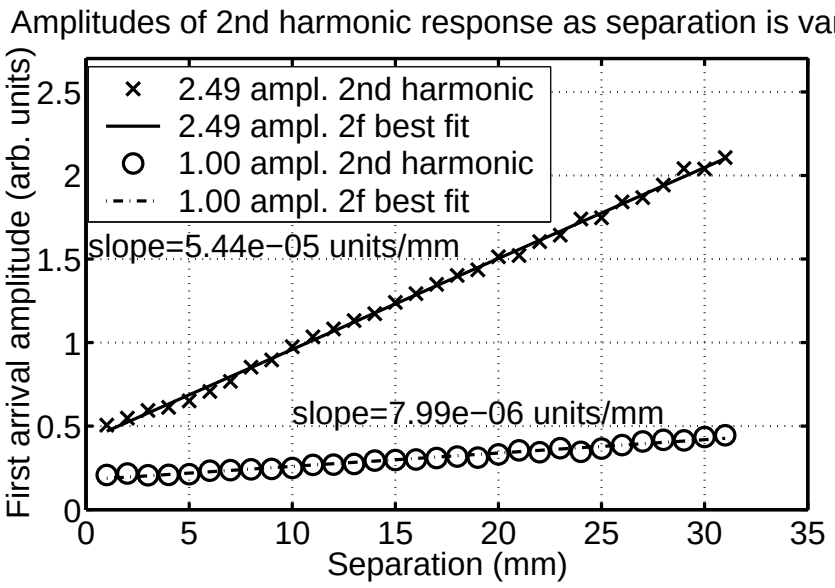

Figure 7.7: Second harmonic impulse response amplitude as source-receiver distance is varied.

The ratio of the slopes of the second harmonics of the experiments at 2.49 and 1.00 excitation amplitudes is 6.81. sqrt(slope ratio)=2.61.

amplitude. These waveforms are the linear and second harmonic impulse responses as measured according to the procedure described in chapters 4 and 5. The direct arrival can be seen at $t = 7\mu s$ and a reverberation between source and receiver transducers appears at $t = 12\mu s$. It is important to note that the burst width for this experiment was 6 μs. Compare that to the 1 μs width of the impulses in fig. 7.3 to see the improvement in time resolution resulting from our method. Figure 7.4 shows the linear impulse response waveforms as a function of separation for a relative excitation amplitude of 2.49. Figure 7.5 shows the corresponding second harmonic impulse response waveforms. The peak amplitudes from figures 7.4 and 7.5 were extracted along with those from the 1.00 rel. amplitude experiment. The peak amplitudes of the linear impulse response are shown in Figure 7.6 and the second harmonic amplitudes are shown in figure 7.7. We see that the amplitude of the linear impulse response remains relatively constant, while the amplitude of the second harmonic increases linearly with propagation distance, as expected.

From theory (Lamb [17] and see below), we expect the second harmonic impulse response to vary with the square of the excitation amplitude. From the two runs at different amplitudes, this can be easily verified. The excitation amplitude ratio (and linear impulse response ratio) of the two experiments is 2.49. We would expect the square root of the ratio of the slopes of the second harmonic impulse responses to approximately match this. In fact, it does. The ratio of of the slopes is 6.81. The square root of that is 2.61, within reasonable error of the amplitude ratio of 2.49. This is also approximately consistent with the ratios of the initial slopes of the second harmonic curves 1, 2, and 3 from Krassilnikov [16] (fig. 7.1).

7.3 Simulation results

To further verify and understand our method, we decided to repeat the above experiment in simulation. We implemented the finite-difference simulator with a nonlinear constitutive law as discussed in chapter 6. We simulated a source and receiver and varied the distance between them. Parameters were selected so as to operate in the same regime of weak nonlinearity as the physical experiments carried out in water. The same data collection program used for the physical experiments was used to collect the simulation data, but with the simulator 'plugged in' in place of physical hardware. Step sizes of Δx and Δt were selected according to the criteria discussed above in section 6.3. Additional experiments, with scaled Δx and Δt values, generated identical results to those shown below, confirming convergence of the simulation.

Figures 7.8, 7.9, 7.10, and 7.11 show the results of the finite difference simulations of harmonic generation in water. Precisely the same phenomena observed in the experiments are seen here. Nonlinearity grows proportionally with distance and with the square of the excitation amplitude.

7.4 An analytic solution

We follow the analysis of Lamb [17] to demonstrate an approximate analytic solution for harmonic generation in water. Consider the nonlinear one-dimensional PDE of equation 6.2:

$$\frac{\partial^2 y}{\partial t^2} = \frac{E_1}{\rho}\frac{\partial^2 y}{\partial x^2} + 2\frac{E_2}{\rho}\frac{\partial y}{\partial x}\frac{\partial^2 y}{\partial x^2} \tag{6.2}$$

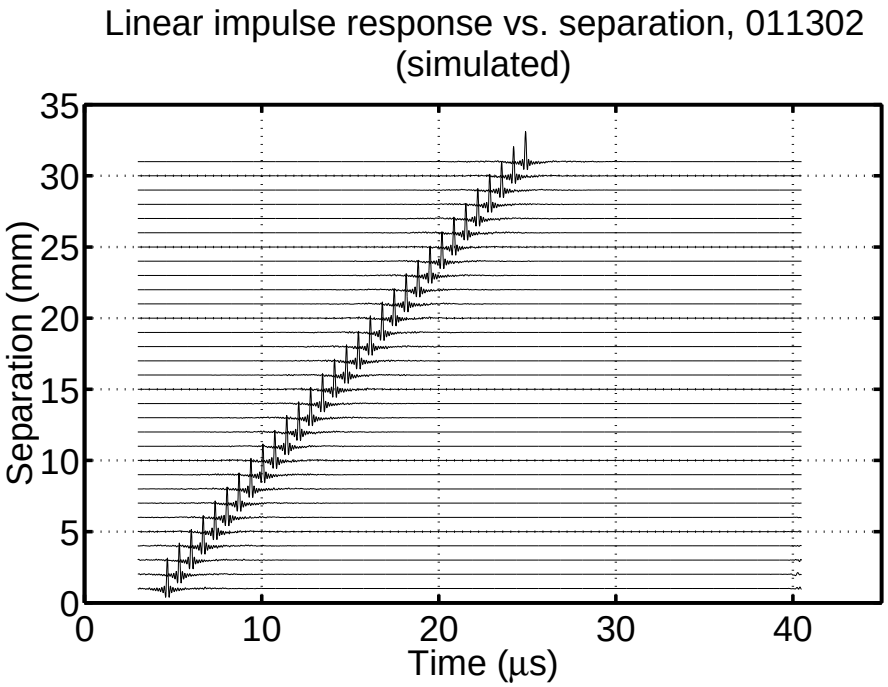

Figure 7.8: Simulated linear impulse response waveforms as source-receiver distance is varied.

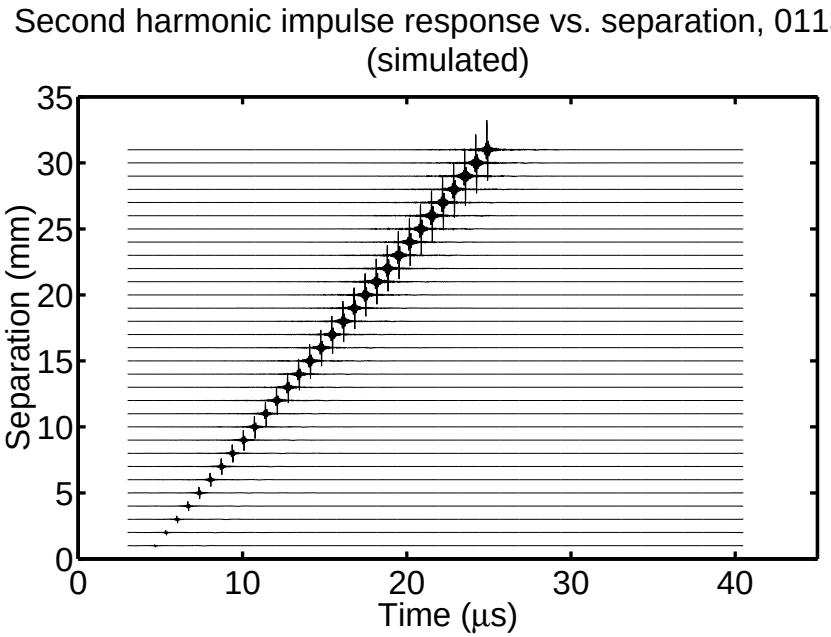

Figure 7.9: Simulated second harmonic impulse response waveforms as source-receiver distance is varied.

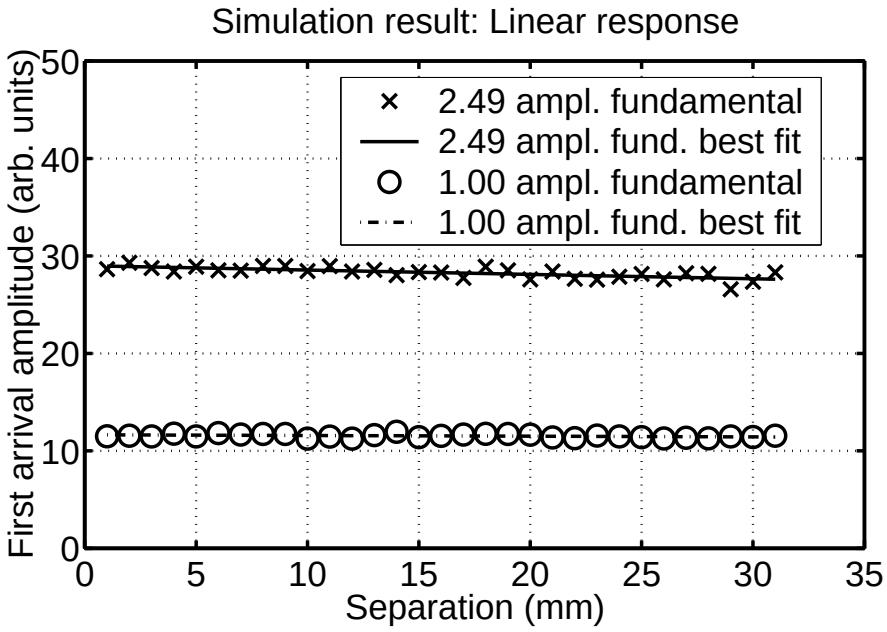

Figure 7.10: Simulated linear impulse response amplitude as source-receiver distance is varied.

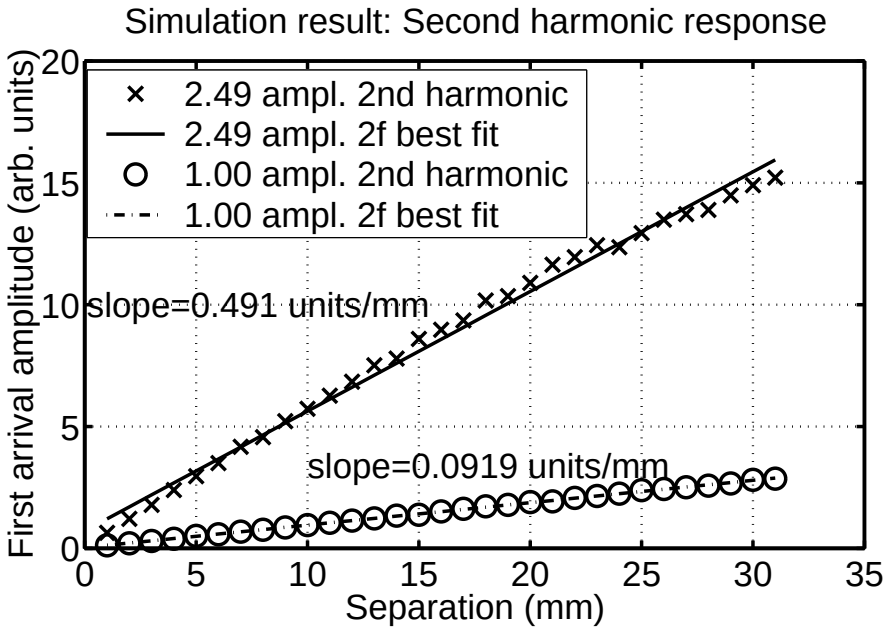

Figure 7.11: Simulated second harmonic impulse response amplitude as source-receiver distance is varied.
Second harmonic slope ratio=5.34. sqrt(slope ratio)=2.31.

If we were to omit the nonlinear term, then the D'Alembert solution $y = f\left(t - \sqrt{\frac{\rho}{E_1}}x\right)$, where $f(t)$ is the solution for $x = 0$, would apply. If we substitute the D'Alembert solution into the nonlinear term of the above PDE, we obtain a new PDE (appendix A.7):

$$\frac{\partial^2 y}{\partial t^2} = \frac{E_1}{\rho}\frac{\partial^2 y}{\partial x^2} + \frac{E_2}{E_1}\frac{\partial}{\partial x}\left(\left[f'\left(t - \sqrt{\frac{\rho}{E_1}}x\right)\right]^2\right) \tag{7.1}$$

This new PDE has the solution (appendix A.7):

$$y = f\left(t - \sqrt{\frac{\rho}{E_1}}x\right) - \frac{E_2\rho}{2E_1^2}x\left[f'\left(t - \sqrt{\frac{\rho}{E_1}}x\right)\right]^2 \tag{7.2}$$

Equation 7.2 is an approximate solution for the original PDE eq. 6.2. In effect, we have substituted the whole of eq. 7.2 into the first two terms of eq. 6.2, but only the D'Alembert solution into the final (nonlinear) term of eq. 6.2. These substitutions solve eq. 6.2 but with residual error because the nonlinear term of eq. 7.2 was never substituted into the nonlinear term of eq. 6.2. It is argued that in the case of weak nonlinearity, the nonlinear terms are both small and hence the error is negligible. If the nonlinear terms are smaller than the linear terms by a factor of ϵ, the error will be $O(\epsilon^2)$, while the largest terms of interest are $O(\epsilon)$.

Equation 7.2 has two terms: the 'D'Alembert term' $f\left(t - \sqrt{\frac{\rho}{E_1}}x\right)$ that solves the linear equation, and the 'nonlinear term', $-\frac{E_2\rho}{2E_1^2}x\left[f'\left(t - \sqrt{\frac{\rho}{E_1}}x\right)\right]^2$. The first and most important characteristic of eq. 7.2 is that it shows the behavior of the nonlinear term. In particular, the amplitude of the nonlinear term is proportional to both the propagation distance x and the square of the excitation amplitude f. This is the fundamental behavior – amplitude proportionality with distance and excitation^2 – that we have seen in both the experiments and the simulation, and it is clearly reflected in the analytic solution.

We would like like to make a detailed comparison between the analytic solution eq. 7.2 and the results from simulation. To simplify the analysis, we will modify the analytic solution to reflect the physical methods of excitation and detection modeled in the simulation. In particular, excitation is applied with a *force actuator*, and detection is performed with a *velocity sensor*. The displacement waveform excited in the medium by a force actuator is proportional to the integral of the force waveform. So if we keep f as the externally applied signal, our solution is (replacing each f in eq. 7.2 with $\int f\ dt$):

$$y = \int f\left(t - \sqrt{\frac{\rho}{E_1}}x\right) dt - \frac{E_2\rho}{2E_1^2}x\left[f\left(t - \sqrt{\frac{\rho}{E_1}}x\right)\right]^2 \tag{7.3}$$

If we measure y with a velocity sensor, we obtain $g = \partial y/\partial t$ (using g to represent the measured signal, as in chapter 3). So the modified analytic solution is:

$$g = f\left(t - \sqrt{\frac{\rho}{E_1}}x\right) - \frac{E_2\rho}{2E_1^2}x\frac{\partial}{\partial t}\left(\left[f\left(t - \sqrt{\frac{\rho}{E_1}}x\right)\right]^2\right) \tag{7.4}$$

The only difference between equations 7.2 and 7.4 is that the squaring and differentiation operations on the nonlinear term are interchanged.

We recall our model from chapter 3, eq. 3.9:

$$\hat{g} = \mathbf{A} \otimes f(t) + \mathbf{B} \otimes f^2(t) \tag{3.9}$$

We can now analyze our analytic solution, eq. 7.4, in terms of this model by inspection. Clearly (see appendix A.8),

$$\mathbf{A} \;=\; \delta\left(t - \sqrt{\frac{\rho}{E_1}}x\right) \tag{7.5}$$

and

$$\mathbf{B} \;=\; -\frac{E_2\rho}{2E_1^2}x\frac{\partial}{\partial t}\delta\left(t - \sqrt{\frac{\rho}{E_1}}x\right) \tag{7.6}$$

We can also look at the frequency spectra of **A** and **B**. Since **A** is a time-shifted delta function, it will have a frequency spectrum of uniform magnitude. The term **B**, being the derivative of a delta function, will have frequency spectrum magnitude proportional to frequency. Recall that **A** and **B** are the idealized non-band-limited linear and second harmonic impulse responses, respectively.

Figure 7.12 shows fundamental and second harmonic impulse responses from the simulation at $x = 21\ mm$, in the time and frequency domains (the third waveform will be discussed below). Recall that when we measure **A**, we measure it by probing it with the composite f, a band-limited impulse. You can see that in fig. 7.12. The solid curve is equivalently our linear impulse response or our bandlimited impulse, time shifted according to eq. 7.5. In the frequency domain, it is zero except over the frequency range of the bursts used to compose it, and it has constant magnitude over that range. Similarly, the dashed curve in fig. 7.12 shows the second harmonic impulse response. From the theory above, we would expect **B** to be proportional to frequency, but bandlimited. That is exactly what we see in the dashed curve of fig. 7.12.

The third curve in fig. 7.12, denoted by dashes and dots, was calculated by differentiating the square of the linear impulse response. This is the nonlinear component of the signal we would obtain by applying the entire composite impulse to the nonlinear system. You can see that it is essentially the same as the second harmonic impulse response waveform, except that it has been filtered. The filtering comes from squaring a function that is band limited. If we take a boxcar in frequency, such as the solid line in fig. 7.12b, and square it in the time domain (convolve it with itself in the frequency domain), we obtain an

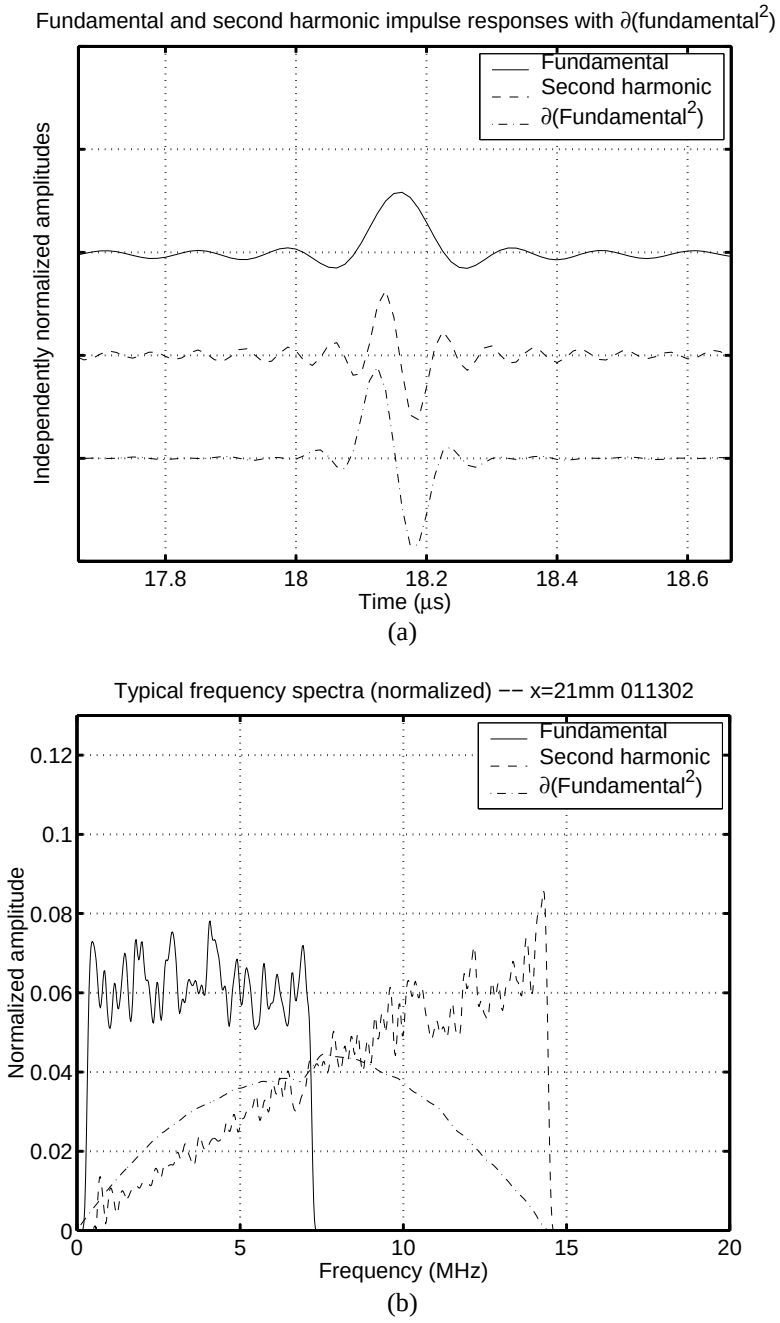

Figure 7.12: Fundamental and second harmonic impulse responses, along with ∂(fundamental^2), in the time domain (a) and the frequency domain (b).

(approximately) triangular frequency spectrum. It is this triangular f^2 that is used to probe **B**. If we had applied the composite impulse directly to the nonlinear medium, we would have probed **B** with this triangular spectrum rather than a flat spectrum. Differentiating the triangular spectrum in the time-domain (multiplying by frequency in the frequency domain), as happens when **B** is applied to f^2, gives the spectrum that is the dash-dot curve in fig 7.12b. It is the same waveform as the second harmonic impulse response, only measured by an impulse with different spectral content.

So the difference between what we measure as the second harmonic impulse response, and the actual quadratic nonlinearity component one would obtain by applying an actual bandlimited impulse, is just a difference in filtering! Moreover, if we were to somehow apply a perfect non-band-limited impulse to the nonlinear system, then the measured quadratic nonlinearity would *be* a non-band-limited version of the second harmonic impulse response as we measure it[1].

In short, we have shown that in certain specialized conditions we can analytically determine the second harmonic impulse response. We have further shown that for this particular experiment, what we measure as "second harmonic impulse response" is a bandlimited representation of the actual quadratic nonlinearity from a broadband impulse.

[1]Assuming we don't violate the approximation of small nonlinearity in the derivation of eq. 7.2

CHAPTER 8

EXPERIMENT: MEASUREMENTS ON A CRACK

The initial motivations for the time-resolved measurement system were the potential applications to non-destructive testing problems. The use of bulk nonlinearity as a flaw or fatigue detector is well established [2], and individual macroscopic cracks are also known to generate harmonics [25]. Here we describe an experiment involving an actual fatigue crack in a block of titanium. This experiment did not work, in the sense that it did not yield any measurable trend in the recorded waveforms. However, it does provide an instructive example that demonstrates limitations and suggests improvements. Furthermore, this failed experiment motivated the successful measurements of contact acoustic nonlinearity that are discussed in the succeeding chapter.

8.1 Experimental configuration

We obtained a titanium specimen containing a fatigue crack. A diagram of the specimen and transducers is shown in figure 8.1. A photograph of the specimen is shown in figure 8.2. A 3 MHz custom built lithium niobate longitudinal wave transducer, honey-coupled, was used as the source. A Panametrics V121 7.5 MHz wideband transducer was used as the receiver. A specially designed jig, described in appendix C, held the source and receiver transducers spring-loaded against the sample. The specimen was placed in an Instron testing machine. The testing machine was used to apply a force and displacement, causing the crack to open. We applied our algorithm, with a burst width of 4 μs and excitation frequency

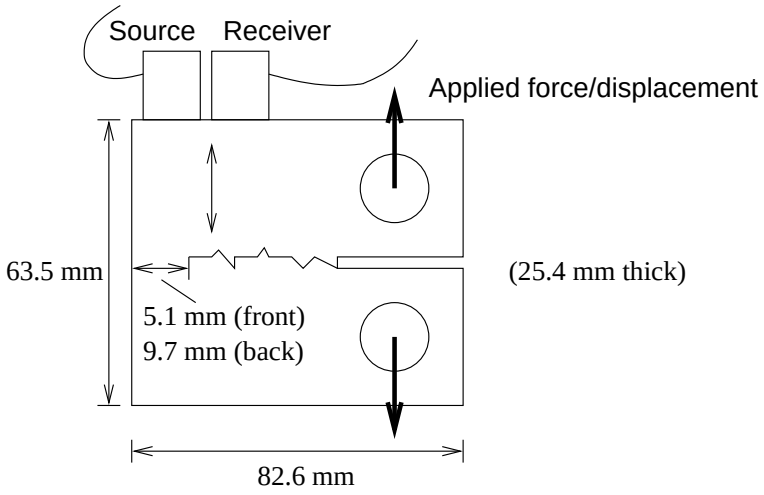

Figure 8.1: Diagram showing the cracked titanium sample and transducer positioning.

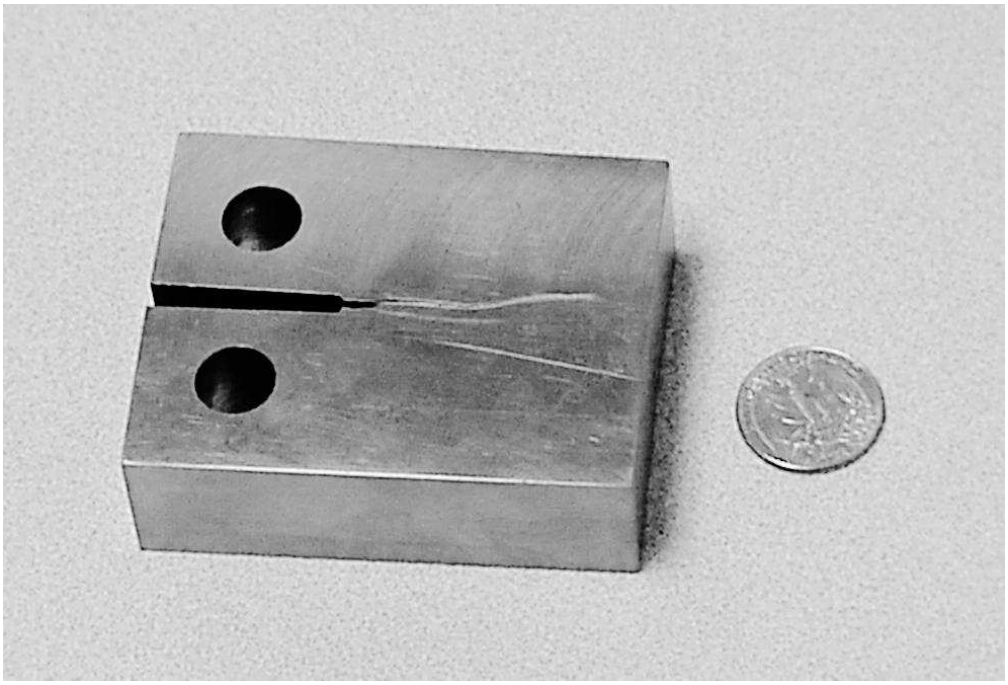

Figure 8.2: Photograph of the cracked titanium sample.

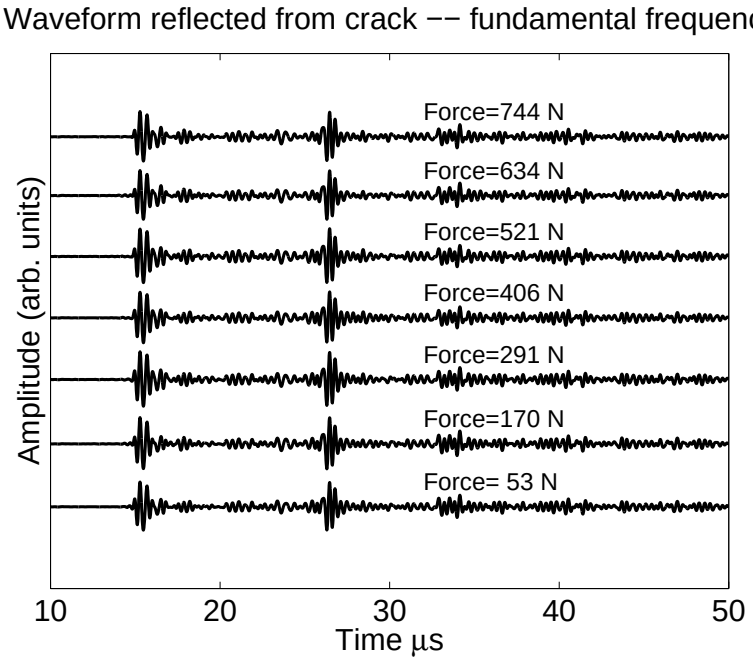

Figure 8.3: Reflected signals from the crack, fundamental (linear) impulse response.

range of $0.5 - 5.5\ MHz$ to measure the the linear and second harmonic impulse responses a function of applied displacement and force.

8.2 Results

The measured waveforms as a function of applied load are shown in figures 8.3 (fundamental) and 8.4 (second harmonic). No trend can immediately be seen. Residuals, waveforms calculated by subtracting the minimum force waveforms from all others, are shown in figures 8.5 and 8.6. Still, no trend appears. There is no measurable change in the linear or second harmonic waveform that correlates with applied load.

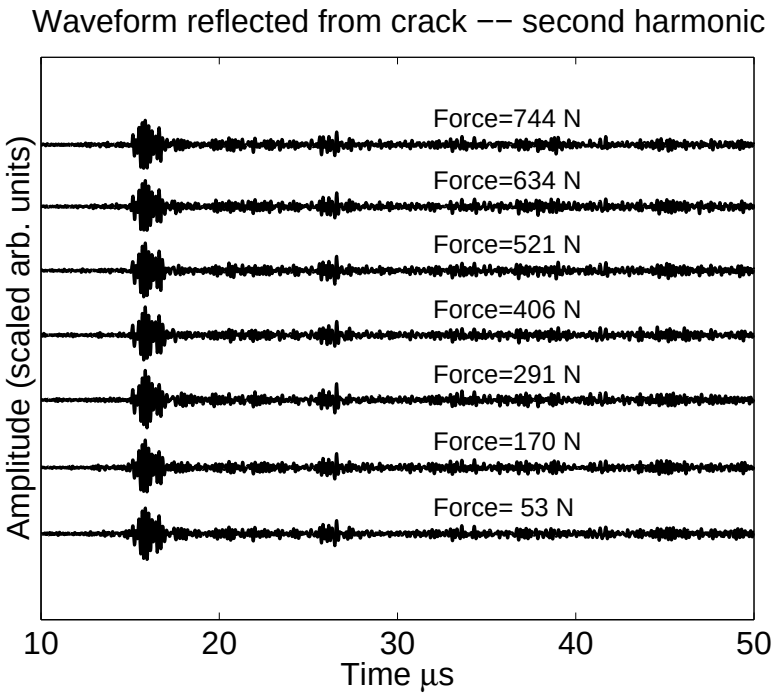

Figure 8.4: Reflected signals from the crack, second harmonic impulse response.

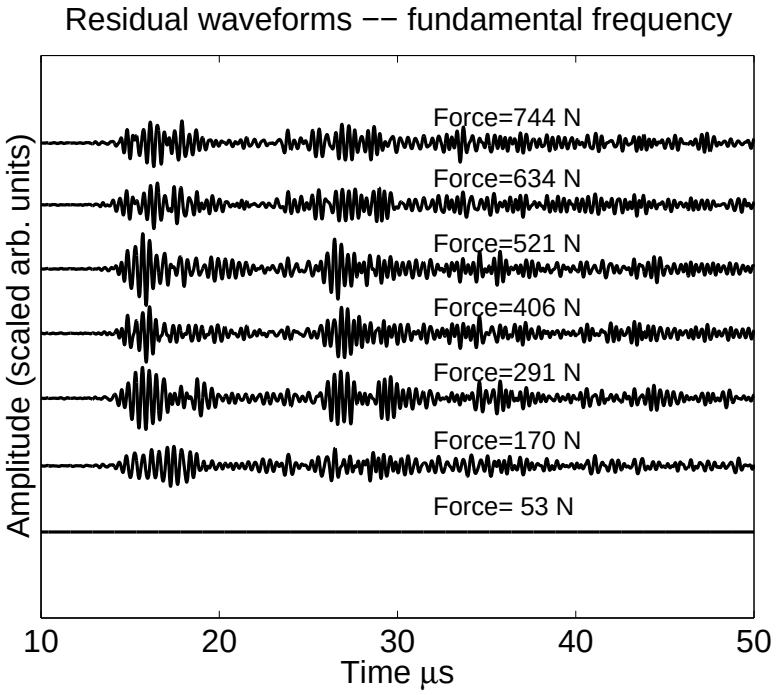

Figure 8.5: Fundamental (linear) impulse response residual.

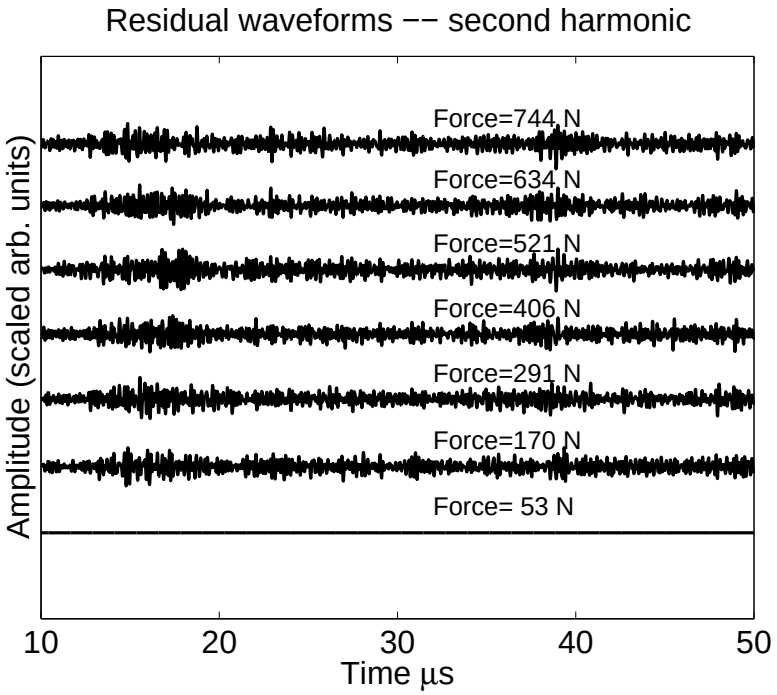

Figure 8.6: Second harmonic impulse response residual.

8.3 Analysis

What is wrong? Why can't we measure a change in nonlinearity from the crack as it opens? We have measured nonlinear response, but it might not be from the crack, it might be from the equipment or other noise/interference sources.

A free surface does not generate acoustic nonlinearity. Perhaps we measured in the wrong place and measured only the free surface, not the crack tip or other areas of nonlinear contact. Perhaps the nonlinear echo came off at an angle and missed the receiver transducer. Even if we were to measure nonlinearity from the crack, what trend would we expect as we apply displacement? It is not clear how the linear and second harmonic impulse response waveforms should change with crack-opening displacement or force.

There are many potential sources of nonlinearity in the experiment, only one of which is the sample. The signal generator which creates the excitations bursts generates harmonics internally. The high power amplifiers can generate harmonics. The transducers or coupling can generate harmonics too. Finally, algorithmic interference can create phantom nonlinearity as described in section 4.3.2. In order to know a-priori that the measured nonlinearity comes from the sample and not from one of these other sources, each of the above interference sources must be analyzed and rejected. This was not done, because it is extremely complicated and time-consuming if it is possible at all.

In general the interference from one of these sources is difficult or impossible to calculate in advance. Nonlinearity in the transducer couplant, for example, will depend on how much couplant was used and exactly how the transducer was placed on the sample. Nonlinearity in the equipment will be a function of all of the settings, including frequency. In order to reject these interference sources, their amplitudes must be measured and found to be orders of magnitude smaller than the phenomena being measured. With current equipment, interference phenomena are generally on the same order, or slightly smaller, than the nonlinear acoustic phenomena. For viable single-shot nonlinearity measurements, much better and more refined equipment is needed. Because of the large number of potential error sources and the complete lack of positive results, we decided not to pursue this experiment further and instead focus on more controlled experiments.

The problems in this experiment with a crack motivated our further studies of contact acoustic nonlinearity. By measuring harmonic generation at a simple and

flat dry interface under load, we can avoid many of the problems described here. In the case of the dry interface, we have a much more controlled experiment. Solodov [24] gives us an estimate for how the nonlinearity should vary as the load is increased. If the nonlinearity does indeed vary in this fashion, we can know for certain that the measured nonlinearity did not arise from problems in the equipment because of the way the measured nonlinearity varies with the load.

CHAPTER 9

EXPERIMENT: HARMONIC GENERATION AT A DRY CONTACT

9.1 Experimental configuration

We wish to investigate in a more robust manner whether the time-resolved nonlinear method can be applied to the nondestructive detection of cracks and flaws. The experiment described in the previous chapter with an actual crack was not well controlled because of the complexity of the crack. The crack has a tip. It also has jagged surfaces and complicated topography. In this experiment, we use a dry contact between the flat surfaces of two aluminum bars as a simplistic representation of a crack. Then we attempt to apply the time-resolved method to measure harmonic generation from that interface, a contact acoustic nonlinearity (CAN).

Figure 9.1 shows results from a similar, but not time-resolved, experiment from Solodov [24]. This experiment was at much lower frequency – 300 Hz – but was otherwise similar in nature to the experiment we describe below. A dry contact between two metal rods was put under compressive load and the second harmonic generation was measured as a function of applied load. The horizontal axis of fig. 9.1 is compressive load (unspecified units). The vertical axis is second harmonic amplitude for samples with: ($\triangle$) polished contact surfaces and ($\bullet$) surfaces finished with grinding.

We take two aluminum bars and put them in contact over a small area (21.6 mm x 25.4 mm), as illustrated in figure 9.2. The upper bar is 38mm thick and the

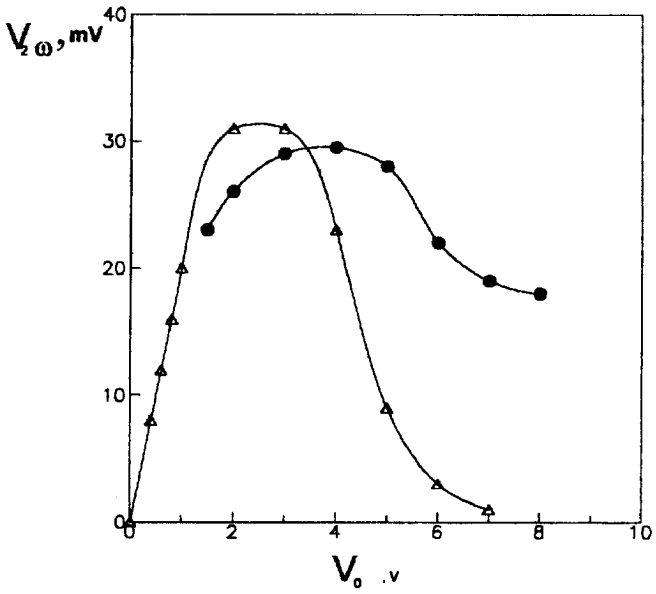

Figure 9.1: Results from Solodov [24].
Second harmonic amplitude is shown as a function of compressive load. (△) corresponds to a polished contact surface; (•) corresponds to a contact surface finished with grinding.

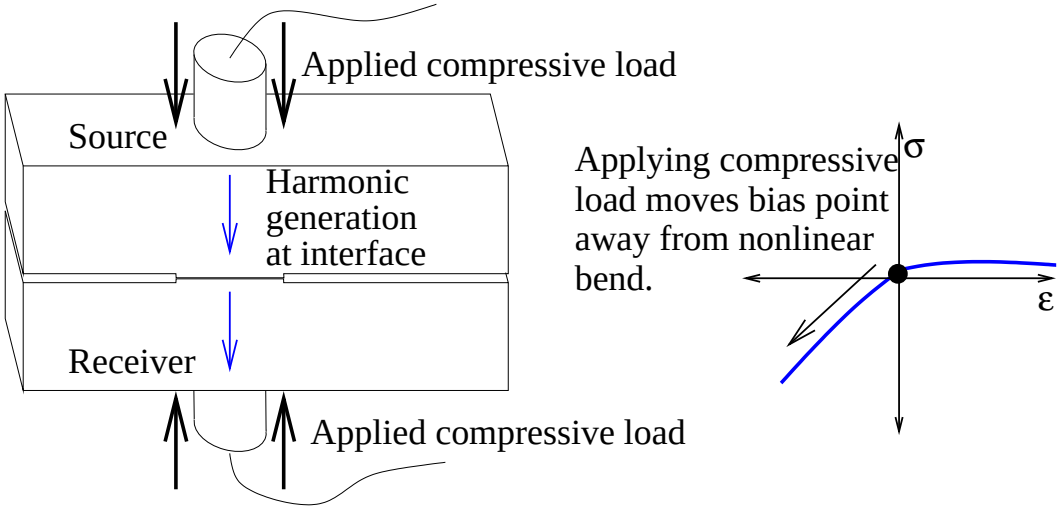

Figure 9.2: Diagram of Contact Acoustic Nonlinearity (CAN) experiment.

lower bar is 25.4mm thick. We will vary the compressive load on the contact interface. Since the interface can support compression but not tension it is a point nonlinearity in the stress-strain relation. As the applied load varies, the 'bias point' of the acoustic vibrations on the stress-strain curve varies, causing the measured nonlinearity to change as illustrated on the right hand side of figure 9.2.

The contact surfaces were prepared by grinding. Spring loaded transducers and honey couplant were used to provide a qualitatively repeatable measurement. We used custom built broadband transducers with a lithium niobate element for maximum bandwidth and minimum transducer nonlinearity. The transducers were manufactured by Valpey Fisher. We measured the transmission of the fundamental and second harmonic frequencies through the interface as a function of applied load. We used a burst width of 4 MHz and a frequency range of 0.5-5.5 MHz, with an average frequency step of 37.3 kHz (fundamental) or 18.6 kHz (second harmonic).

9.2 Experimental results

Figure 9.3 shows sample waveforms corresponding to a compressive load of 11.4 MPa. The direct arrival can be seen at 14 μs and reverberations in the aluminum bars appear at 22.5 and 26 μs. Figure 9.4 shows the entire set of composite fundamental waveforms, and fig. 9.5 shows the entire set of second harmonic waveforms as a function of applied load. The first arrival amplitudes of the waveforms in figs. 9.4 and 9.5 are shown in fig. 9.6. We note that as the applied compressive load increases, the measured fundamental component increases linearly, while the measured second harmonic component increases

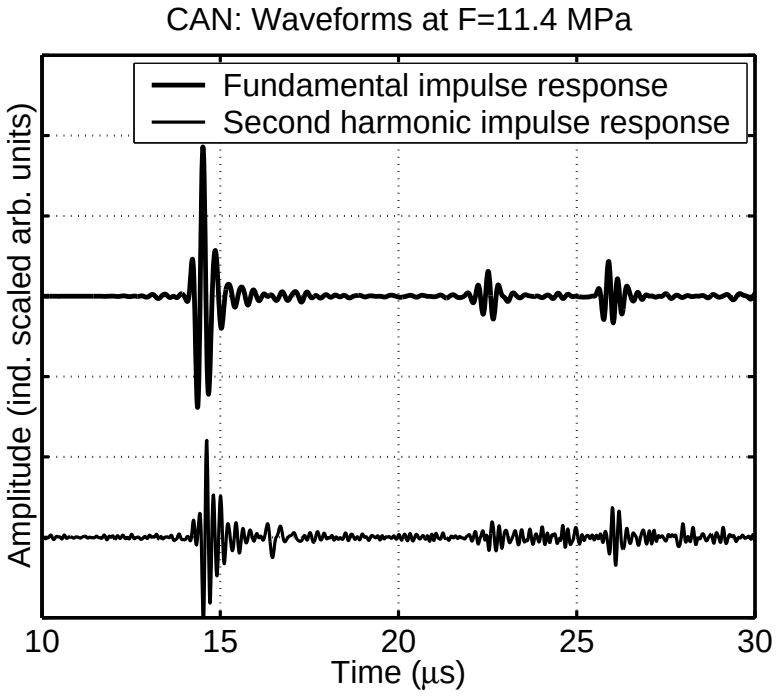

Figure 9.3: Sample contact acoustic nonlinearity waveforms, Force/Area=11.4 MPa.

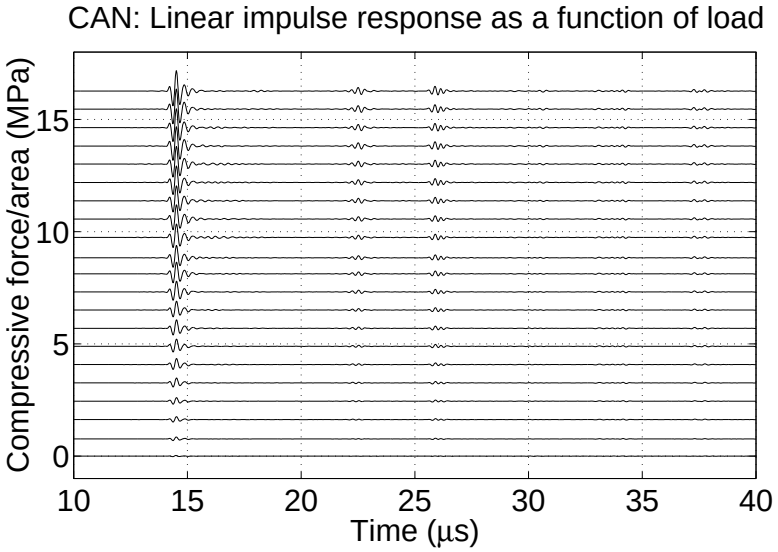

Figure 9.4: Fundamental impulse response waveforms from contact acoustic nonlinearity as a function of applied load.

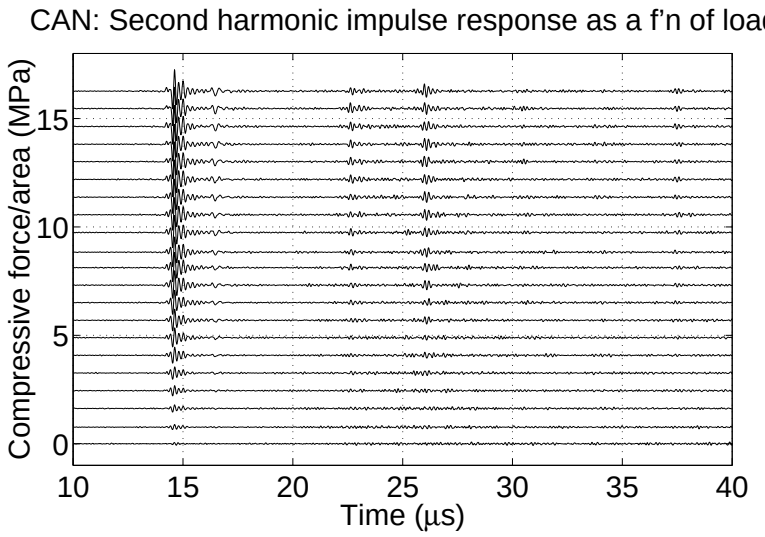

Figure 9.5: Second harmonic impulse response waveforms (contact acoustic nonlinearity) as a function of applied load.

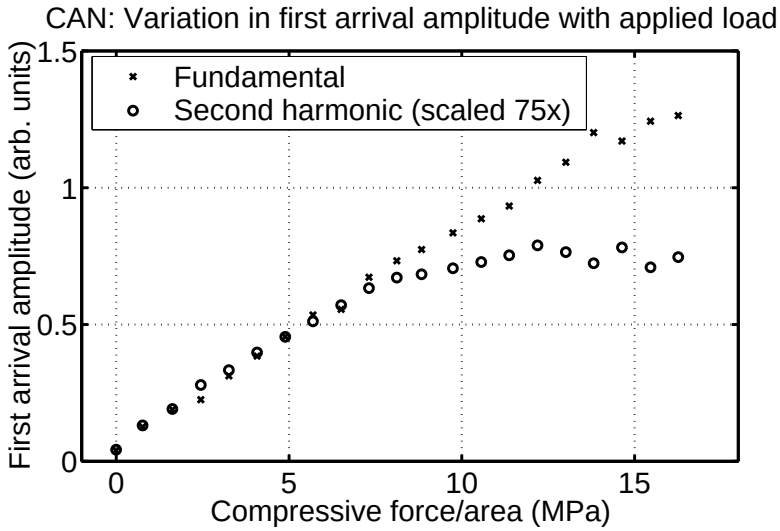

Figure 9.6: Change of first arrival amplitude with applied compressive load, dry-contact CAN.

linearly initially, but stops increasing with higher loads. This is both plausible and consistent with published results such as Solodov [24] (fig. 9.1). At no load, no signal is transmitted through the interface because the contact area is very small because of surface roughness, so the measured fundamental and second harmonic signals are zero. As a load is applied, both fundamental and second harmonic signals increase proportionally. As the load continues to increase, the second harmonic signal decreases relative to the fundamental signal because the compressive load biases the system away from the nonlinear regime. With sufficient load, the amplitude of the fundamental signal should approach a constant, and the amplitude of the second harmonic signal should approach zero.

9.3 Simulation results

Unfortunately, the maximum force applied in the above experiment was limited by the strength of the jig supporting the transducers and experiment. To get a better understanding of the phenomena and measurement issues involved, we simulated the experimental system using the finite difference model described in chapter 6.

The stress-strain relation of the nonlinear contact model was given in eq. 6.9 and shown in figure 6.4. Here, we will focus on the region in the stress-strain curve in which stress is on the order of the amplitude of the simulated elastic stress wave. Figure 9.7 shows the stress-strain curve of the nonlinear contact model for stresses between -80 and 0 MPa. For comparison the peak to peak amplitude selected for the simulated elastic waves was 9 MPa.

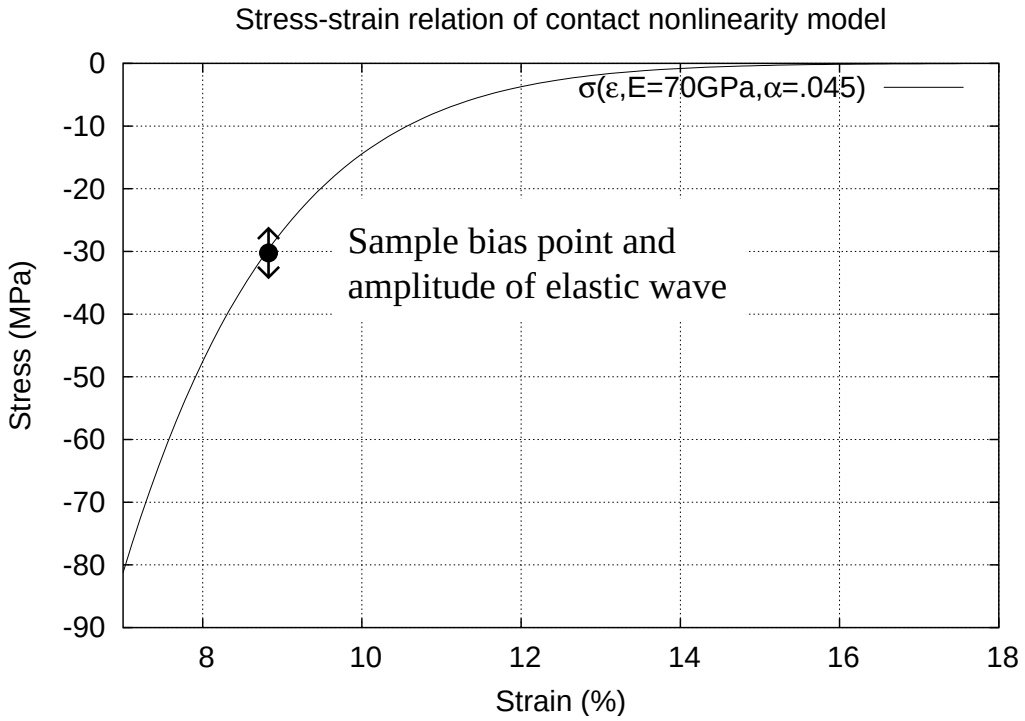

Figure 9.7: Stress-strain relation of nonlinear contact model for small stress.

It is important to emphasize that no claim whatsoever is made that the simulation parameters reflect the above experiments quantitatively. The simulation parameters, α, Δx, and elastic wave amplitude, were tuned so that they qualitatively match the observed experimental data over the range of the experiment.

From figure 9.7 it is directly possible to see where the nonlinearity comes from. The applied compressive load sets the vertical position of the bias point marked in fig. 9.7. The simulated elastic wave modulates $\pm 4.5\ MPa$ about the bias point. Nonlinearity comes from the curvature of the stress-strain curve within that $\pm 4.5\ MPa$ of the bias point. As can be seen in figure 9.7, the more compressive load is applied, the less curvature exists within the $\pm 4.5\ MPa$, so

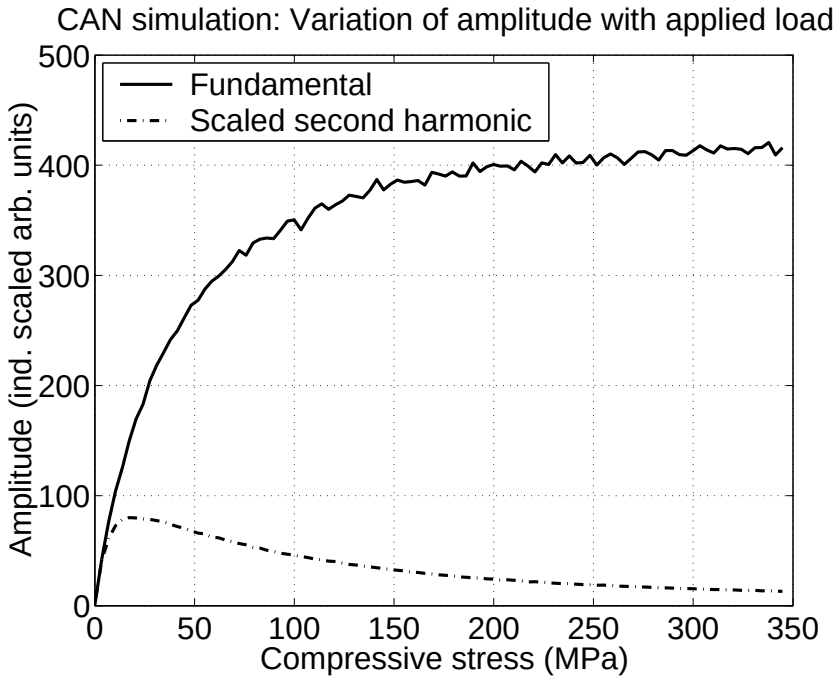

Figure 9.8: Amplitude of fundamental and second harmonic signals from simulation experiment.

the less relative nonlinearity would be observed.

A simulation experiment was performed with conditions similar to the physical experiments described in the previous section. Figure 9.8 shows the measured amplitudes of the linear impulse response and the second harmonic impulse response from the simulation. The decrease in nonlinearity under large load is clearly visible in these results. Figure 9.9 shows the amplitudes over a range of stress analogous to the experimental results shown above in figure 9.6. The plausible contact nonlinearity model we developed in chapter 6 shows behavior consistent with our expectations, our experimental results, and previous work such as that by Solodov [24] (figure 9.1).

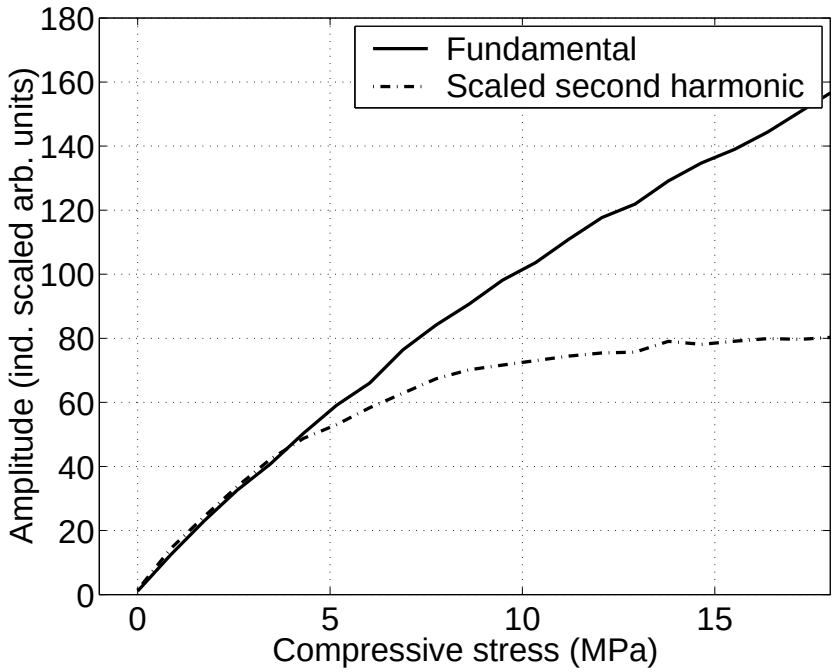

Figure 9.9: Amplitude of fundamental and second harmonic signals from simulation experiment, limited stress range.

CHAPTER 10

A BLUEPRINT FOR FUTURE DEVELOPMENT

While we have very successfully developed and demonstrated a technique for time-resolved measurements of nonlinearity, the technique will remain an academic exercise until it is refined to the point of practical utility. Time-resolved measurements of nonlinearity have the potential to dramatically enhance non-destructive testing by providing information on nonlinearity while still using the same measurement methodologies used today.

In order to transform our method from a laboratory curiosity to a commercially viable nondestructive testing tool, several critical improvements are needed. First, more 'headroom' is needed. The equipment must have a large usable dynamic range. Whenever a nonlinear signal is detected, there must be no question that the nonlinearity came from the sample, not the equipment. Second, the speed of the measurement must be increased. The time required to obtain a waveform must be reduced from hours to seconds or minutes.

Fortunately, there are a large number of potential improvements that are at least moderately straightforward. Implementing the proposed digital system of section 5.4 would provide major increments in both headroom and performance. In addition, measurement time could be substantially reduced by reducing the burst width proportionally with higher frequencies. Reducing the burst width both directly allows faster measurements – the repetition rate is limited according to the burst width to prevent amplifier overheating – and reduces the number of frequency steps required because narrower bursts have wider bandwidth. Furthermore, the excitation and receiver bursts could be optimized to give a flat

frequency response of the composite impulse at wider burst frequency spacing. This would reduce the number of frequency steps required per measurement and further reduce the measurement time.

It would also be worthwhile to redevelop the algorithm to use nonlinear mixing of two frequencies rather than harmonic generation. Instead of applying a single frequency to the sample and measuring harmonic generation, we can apply two frequencies, with different amplifiers and a multi-element transducer, and measure the nonlinear mixing. Measurement of mixing is much less sensitive to nonlinearity in the equipment and transducers because the two probe frequencies can be kept separate until they reach the sample being tested. Furthermore, one of the probe frequencies can be fixed while the other is varied. This means that a narrowband transducer can be used for the fixed probe. Narrowband transducers are much more efficient, so the signal amplitude will be higher, making the nonlinearity proportionally easier to detect.

We suspect that the above improvements will allow sufficient headroom and sufficiently fast measurements for this technique to be useful in practical nondestructive testing applications. The extra information this technique captures has the potential to create a dramatic improvement in nondestructive measurements of materials.

CHAPTER 11

CONCLUSIONS

We have developed a new method for studying materials and systems exposed to finite amplitude sound waves. By superimposing a series of narrowband bursts to form a composite impulse, we are able to make time-resolved measurements of nonlinear harmonic generation phenomena. Such measurements have the potential for great practical utility in the field of nondestructive testing. We have developed and described a mathematical justification for our method, and discussed its benefits and limitations. We built a measurement system capable of testing the method and performed several demonstrative experiments. A simulation environment was developed to cross-check the experiments and study noise and artifacts.

We demonstrated harmonic generation in in water as a function of transducer distance, and showed a match between theory, simulation, and experiment. We demonstrated harmonic generation at a dry contact nonlinearity, and showed a match between simulation, experiment, and previously published results. We have not yet demonstrated specific experiments that would be impossible to perform using conventional narrowband harmonic generation experiments, but we have demonstrated experiments in which the interpretation was far easier and less vulnerable to interference due to our method. We have also discussed how time-resolved measurements of nonlinear phenomena could be used to enhance the nondestructive testing of materials. Our time-resolved method allows time-domain, easy to interpret measurements of nonlinear acoustic phenomena.

APPENDIX A

DERIVATIONS

A.1 Demonstration that the discrete time Volterra expansion is a Taylor series

We shall show in this section that discrete time Volterra expansion given in eq. 3.5 is a Taylor series. The discrete time Volterra expansion was given as:

$$\hat{g}_i = \left.\frac{\partial g_i}{\partial f_j}\right|_{f=0} f_j + \frac{1}{2!}\left.\frac{\partial^2 g_i}{\partial f_j \partial f_k}\right|_{f=0} f_j f_k + \frac{1}{3!}\left.\frac{\partial^3 g_i}{\partial f_j \partial f_k \partial f_l}\right|_{f=0} f_j f_k f_l + \ldots \quad (3.5)$$

$$\left(\begin{array}{c} \text{sum over} \\ j,k,l, \text{ etc.} \end{array} \right)$$

Since a Taylor series approximates a function by matching its value and derivatives at a particular point, we can show that eq. 3.5 is a Taylor series by confirming that the functional values and derivatives of g and $\hat{g}$ match at $f = 0$.

At $f_i = 0$ $(\forall i)$, $\hat{g}_i = 0$. Since it is assumed that the system provides no response to zero input, this is consistent with $g_i = 0$. Consider the first derivatives:

$$\frac{\partial \hat{g}_i}{\partial f_m} = \left.\frac{\partial g_i}{\partial f_j}\right|_{f=0} \frac{\partial f_j}{\partial f_m} + \frac{1}{2!}\left.\frac{\partial^2 g_i}{\partial f_j \partial f_k}\right|_{f=0} \left(f_j \frac{\partial f_k}{\partial f_m} + f_k \frac{\partial f_j}{\partial f_m} \right) + \text{H.O.T} \ldots \quad (A.1)$$

(sum over repeated indices in this section)

Assuming the time samples of f are independent, $\frac{\partial f_k}{\partial f_m} = \delta_{km}$.

$$\begin{aligned} \frac{\partial \hat{g}_i}{\partial f_m} &= \left.\frac{\partial g_i}{\partial f_j}\right|_{f=0} \delta_{jm} + \frac{1}{2!}\left.\frac{\partial^2 g_i}{\partial f_j \partial f_k}\right|_{f=0} f_j \delta_{km} + \frac{1}{2!}\left.\frac{\partial^2 g_i}{\partial f_j \partial f_k}\right|_{f=0} f_k \delta_{jm} + \text{H.O.T} \ldots \\ &= \left.\frac{\partial g_i}{\partial f_m}\right|_{f=0} + \frac{1}{2!}\left.\frac{\partial^2 g_i}{\partial f_j \partial f_m}\right|_{f=0} f_j + \frac{1}{2!}\left.\frac{\partial^2 g_i}{\partial f_m \partial f_k}\right|_{f=0} f_k + \text{H.O.T} \ldots \quad (A.2) \end{aligned}$$

Evaluating at $f = 0$:

$$\left.\frac{\partial \hat{g}_i}{\partial f_m}\right|_{f=0} = \left.\frac{\partial g_i}{\partial f_m}\right|_{f=0} \tag{A.3}$$

So the first derivatives match at $f = 0$. Now consider the second derivatives:

$$\frac{\partial^2 \hat{g}_i}{\partial f_m \partial f_p} = \frac{1}{2!}\left.\frac{\partial^2 g_i}{\partial f_j \partial f_m}\right|_{f=0}\frac{\partial f_j}{\partial f_p} + \frac{1}{2!}\left.\frac{\partial^2 g_i}{\partial f_m \partial f_k}\right|_{f=0}\frac{\partial f_k}{\partial f_p} + \text{H.O.T . . .} \tag{A.4}$$

Once again, since $\frac{\partial f_k}{\partial f_m} = \delta_{km}$:

$$\begin{aligned}\frac{\partial^2 \hat{g}_i}{\partial f_m \partial f_p} &= \frac{1}{2!}\left.\frac{\partial^2 g_i}{\partial f_j \partial f_m}\right|_{f=0}\delta_{jp} + \frac{1}{2!}\left.\frac{\partial^2 g_i}{\partial f_m \partial f_k}\right|_{f=0}\delta_{kp} + \text{H.O.T . . .} \\ &= \frac{1}{2!}\left.\frac{\partial^2 g_i}{\partial f_p \partial f_m}\right|_{f=0} + \frac{1}{2!}\left.\frac{\partial^2 g_i}{\partial f_m \partial f_p}\right|_{f=0} + \text{H.O.T . . .}\end{aligned} \tag{A.5}$$

Assuming $\frac{\partial^2 g_i}{\partial f_p \partial f_m} = \frac{\partial^2 g_i}{\partial f_m \partial f_p}$:

$$\frac{\partial^2 \hat{g}_i}{\partial f_m \partial f_p} = \left.\frac{\partial^2 g_i}{\partial f_m \partial f_p}\right|_{f=0} + \text{H.O.T . . .} \tag{A.6}$$

Evaluated at $f = 0$:

$$\left.\frac{\partial^2 \hat{g}_i}{\partial f_m \partial f_p}\right|_{f=0} = \left.\frac{\partial^2 g_i}{\partial f_m \partial f_p}\right|_{f=0} \tag{A.7}$$

The second derivatives of $\hat{g}$ with respect to f also match the second derivatives of g with respect to f at $f = 0$. We have therefore confirmed that equation 3.5 is indeed a Taylor series for the mapping of f onto g, at least up to the quadratic terms. A similar procedure can be applied to the cubic and higher terms.

A.2 Difference equation of a weakly nonlinear medium

We derive the discrete time difference equation (eq. 6.1) used to simulate a nonlinear medium.

Consider the nonlinear spring from fig. 6.1: $F = k_1 y + \frac{1}{2}k_2 y^2$ (F is defined as the force applied *to* the spring, not the force applied *by* the spring). Consider a mass

at position x. The displacement from nominal length of the spring on the left is $y_x^t - y_{x-\Delta x}^t$. The displacement of the spring on the right is $y_{x+\Delta x}^t - y_x^t$. The force on the left to the left is:

$$k_1(y_x^t - y_{x-\Delta x}^t) + \frac{1}{2}k_2\left[(y_x^t)^2 - 2y_x^t y_{x-\Delta x}^t + (y_{x-\Delta x}^t)^2\right] \tag{A.8}$$

The force on the right to the right is:

$$k_1(y_{x+\Delta x}^t - y_x^t) + \frac{1}{2}k_2\left[(y_{x+\Delta x}^t)^2 - 2y_x^t y_{x+\Delta x}^t + (y_x^t)^2)\right] \tag{A.9}$$

The net force to the right on the mass is the difference of eq. A.9 and eq. A.8:

$$F = k_1(y_{x+\Delta x}^t - 2y_x^t + y_{x-\Delta x}^t) + \frac{1}{2}k_2\left[(y_{x+\Delta x}^t)^2 - (y_{x-\Delta x}^t)^2 - 2y_x^t(y_{x+\Delta x}^t - y_{x-\Delta x}^t)\right] \tag{A.10}$$

The difference of squares can be factored into $(y_{x+\Delta x}^t - y_{x-\Delta x}^t)(y_{x+\Delta x}^t + y_{x-\Delta x}^t)$. Now each of the k_2 terms of equation A.10 has a factor of $y_{x+\Delta x}^t - y_{x-\Delta x}^t$. These can be factored out, obtaining a simple form for the net force on the mass:

$$F = k_1(y_{x+\Delta x}^t - 2y_x^t + y_{x-\Delta x}^t) + \frac{1}{2}k_2(y_{x+\Delta x}^t - y_{x-\Delta x}^t)(y_{x+\Delta x}^t + y_{x-\Delta x}^t - 2y_x^t) \tag{A.11}$$

All that remains at this point is to write $F = ma$ with discretized time. If we have a time step Δt, then the acceleration a_x^t is:

$$a_x^t = \frac{v_x^{t+\Delta t/2} - v_x^{t-\Delta t/2}}{\Delta t} \tag{A.12}$$

in terms of the velocity v. The velocity $v_x^{t+\Delta t/2}$ is $(y_x^{t+\Delta t} - y_x^t)/\Delta t$. The velocity at $t - \Delta t/2$ is $v_x^{t-\Delta t/2} = (y_x^t - y_x^{t-\Delta t})/\Delta t$. Putting this together, the acceleration becomes:

$$a_x^t = \frac{y_x^{t+\Delta t} - 2y_x^t + y_x^{t-\Delta t}}{(\Delta t)^2} \tag{A.13}$$

Writing $ma = F$ with the acceleration of eq. A.13 and force of eq. A.11 gives the difference equation, eq. 6.1:

$$\frac{m}{(\Delta t)^2}(y_x^{t+\Delta t} - 2y_x^t + y_x^{t-\Delta t}) = \tag{6.1}$$
$$k_1(y_{x+\Delta x}^t + y_{x-\Delta x}^t - 2y_x^t) + \frac{k_2}{2}(y_{x+\Delta x}^t - y_{x-\Delta x}^t)(y_{x+\Delta x}^t + y_{x-\Delta x}^t - 2y_x^t)$$

A.3 Derivation of the nonlinear PDE from the discrete time difference equation

We start with the discrete-time nonlinear difference equation, eq. 6.1:

$$\frac{m}{(\Delta t)^2}(y_x^{t+\Delta t} - 2y_x^t + y_x^{t-\Delta t}) = \tag{6.1}$$
$$k_1(y_{x+\Delta x}^t + y_{x-\Delta x}^t - 2y_x^t) + \frac{k_2}{2}(y_{x+\Delta x}^t - y_{x-\Delta\ x}^t)(y_{x+\Delta x}^t + y_{x-\Delta x}^t - 2y_x^t)$$

and wish to turn this into a PDE by taking the limit as Δx and Δt go to zero.

$$m\left(\frac{\frac{y_x^{t+\Delta t}-y_x^t}{\Delta t} - \frac{y_x^t-y_x^{t-\Delta t}}{\Delta t}}{\Delta t}\right) = \tag{A.14}$$
$$k_1(\Delta x)^2\left(\frac{\frac{y_{x+\Delta x}^t-y_x^t}{\Delta x} - \frac{y_x^t-y_{x-\Delta x}^t}{\Delta x}}{\Delta x}\right)$$
$$+\frac{k_2(\Delta x)^3}{2}\left(\frac{y_{x+\Delta x}^t - y_{x-\Delta x}^t}{\Delta x}\right)\left(\frac{\frac{y_{x+\Delta x}^t-y_x^t}{\Delta x} - \frac{y_x^t-y_{x-\Delta x}^t}{\Delta x}}{\Delta x}\right)$$

As Δx and $\Delta t \rightarrow 0$,

$$m\left(\frac{\left.\frac{\partial y}{\partial t}\right|_{x,t+\frac{\Delta t}{2}} - \left.\frac{\partial y}{\partial t}\right|_{x,t-\frac{\Delta t}{2}}}{\Delta t}\right) = \tag{A.15}$$
$$k_1(\Delta x)^2\left(\frac{\left.\frac{\partial y}{\partial x}\right|_{x+\frac{\Delta x}{2},t} - \left.\frac{\partial y}{\partial x}\right|_{x-\frac{\Delta x}{2},t}}{\Delta x}\right)$$
$$+\frac{k_2(\Delta x)^3}{2}\left.\frac{\partial y}{\partial x}\right|_{x,t}\left(\frac{\left.\frac{\partial y}{\partial x}\right|_{x+\frac{\Delta x}{2},t} - \left.\frac{\partial y}{\partial x}\right|_{x-\frac{\Delta x}{2},t}}{\Delta x}\right)$$

$$m \left.\frac{\partial^2 y}{\partial t^2}\right|_{x,t} = k_1(\Delta x)^2 \left.\frac{\partial^2 y}{\partial x^2}\right|_{x,t} + \frac{k_2(\Delta x)^3}{2} \left.\frac{\partial y}{\partial x}\right|_{x,t} \left.\frac{\partial^2 y}{\partial x^2}\right|_{x,t} \tag{A.16}$$

$$m\frac{\partial^2 y}{\partial t^2} = k_1(\Delta x)^2\frac{\partial^2 y}{\partial x^2} + \frac{k_2(\Delta x)^3}{2}\frac{\partial y}{\partial x}\,\frac{\partial^2 y}{\partial x^2} \tag{A.17}$$

If we let $k_1 = \frac{E_1 A}{\Delta x}$, $k_2 = \frac{4E_2 A}{(\Delta x)^2}$, and $m = \rho A \Delta x$, we obtain the PDE, eq. 6.2:

$$\frac{\partial^2 y}{\partial t^2} \;=\; \frac{E_1}{\rho}\frac{\partial^2 y}{\partial x^2} \;+\; 2\frac{E_2}{\rho}\frac{\partial y}{\partial x}\frac{\partial^2 y}{\partial x^2} \tag{6.2}$$

A.4 Derivation of the nonlinear PDE from the nonlinear elastic constitutive law

We derive the nonlinear PDE of equation 6.2 from the constitutive law of eq. 6.3:

$$\sigma = E_1\epsilon + E_2\epsilon^2 \tag{6.3}$$

Consider an infinitesimal slice (width δ, mass $\rho A\delta$) of a nonlinear one-dimensional medium with the above constitutive law. The strain on the right can be evaluated as $\left.\frac{\partial y}{\partial x}\right|_{x+\delta/2}$. The strain on the left can be evaluated as $\left.\frac{\partial y}{\partial x}\right|_{x-\delta/2}$. The corresponding stresses can be evaluated through the constitutive law as $E_1 \left.\frac{\partial y}{\partial x}\right|_{x+\delta/2} + E_2\left[\left.\frac{\partial y}{\partial x}\right|_{x+\delta/2}\right]^2$ and $E_1 \left.\frac{\partial y}{\partial x}\right|_{x-\delta/2} + E_2\left[\left.\frac{\partial y}{\partial x}\right|_{x-\delta/2}\right]^2$ respectively. The net force per area on our infinitesimal slice comes from the difference in stress:

$$F/A = E_1\left(\left.\frac{\partial y}{\partial x}\right|_{x+\delta/2} - \left.\frac{\partial y}{\partial x}\right|_{x-\delta/2}\right) + E_2\left[\left(\left.\frac{\partial y}{\partial x}\right|_{x+\delta/2}\right)^2 - \left(\left.\frac{\partial y}{\partial x}\right|_{x-\delta/2}\right)^2\right] \tag{A.18}$$

The difference of squares in the E_2 term can be factored:

$$\begin{aligned} F/A = {} & E_1\left(\left.\frac{\partial y}{\partial x}\right|_{x+\delta/2} - \left.\frac{\partial y}{\partial x}\right|_{x-\delta/2}\right) \\ & + E_2\left(\left.\frac{\partial y}{\partial x}\right|_{x+\delta/2} - \left.\frac{\partial y}{\partial x}\right|_{x-\delta/2}\right)\left(\left.\frac{\partial y}{\partial x}\right|_{x+\delta/2} + \left.\frac{\partial y}{\partial x}\right|_{x-\delta/2}\right) \end{aligned} \tag{A.19}$$

Divide through by δ:

$$F/(A\delta) = \tag{A.20}$$
$$E_1 \frac{\left(\frac{\partial y}{\partial x}\Big|_{x+\delta/2} - \frac{\partial y}{\partial x}\Big|_{x-\delta/2}\right)}{\delta} + E_2 \frac{\left(\frac{\partial y}{\partial x}\Big|_{x+\delta/2} - \frac{\partial y}{\partial x}\Big|_{x-\delta/2}\right)}{\delta} \left(\frac{\partial y}{\partial x}\Big|_{x+\delta/2} + \frac{\partial y}{\partial x}\Big|_{x-\delta/2}\right)$$

Assume δ is small:

$$F/(A\delta) = E_1 \frac{\partial^2 y}{\partial x^2} + E_2 \frac{\partial^2 y}{\partial x^2}\left(2\frac{\partial y}{\partial x}\right) \tag{A.21}$$

Substitute into $F = ma$:

$$\rho A\delta \frac{\partial^2 y}{\partial t^2} = A\delta\left(E_1 \frac{\partial^2 y}{\partial x^2} + 2E_2 \frac{\partial^2 y}{\partial x^2}\frac{\partial y}{\partial x}\right) \tag{A.22}$$

Dividing through by $\rho A\delta$ gives the PDE of equation 6.2:

$$\frac{\partial^2 y}{\partial t^2} = \frac{E_1}{\rho}\frac{\partial^2 y}{\partial x^2} + 2\frac{E_2}{\rho}\frac{\partial y}{\partial x}\frac{\partial^2 y}{\partial x^2} \tag{6.2}$$

A.5 Dispersive behavior of the linearized difference equation

The linear wave equation is non-dispersive. However, if we take the difference equation, eq. 6.1, and linearize it to be analogous to the linear wave equation, we obtain eq. 6.4:

$$y_x^{t+\Delta t} - 2y_x^t + y_x^{t-\Delta t} = \frac{c^2}{c_\Delta^2}(y_{x+\Delta x}^t + y_{x-\Delta x}^t - 2y_x^t) \tag{6.4}$$

where c is the wavespeed given by $\sqrt{\frac{E_1}{\rho}}$ and c_Δ is the ratio $\frac{\Delta x}{\Delta t}$. Eq. 6.4 turns out to be dispersive! The dispersion is dependent upon the Δx and Δt. To determine

the dispersion, we substitute $y = e^{ik(x-c_{ph}t)}$ into eq. 6.4. This is equivalent to taking a 2-D Z-transform.

$$e^{ik(x-c_{ph}(t+\Delta t))} - 2e^{ik(x-c_{ph}t)} + e^{ik(x-c_{ph}(t-\Delta t))} = \frac{c^2}{c_\Delta^2}\left(e^{ik(x+\Delta x-c_{ph}t)} + e^{ik(x-\Delta x-c_{ph}t)} - 2e^{ik(x-c_{ph}t)}\right) \tag{A.23}$$

$$e^{ikc_{ph}\Delta t}e^{ik(x-c_{ph}t)} - 2e^{ik(x-c_{ph}t)} + e^{-ikc_{ph}\Delta t}e^{ik(x-c_{ph}t)} = \frac{c^2}{c_\Delta^2}\left(e^{ik\Delta x}e^{ik(x-c_{ph}t)} + e^{-ik\Delta x}e^{ik(x-c_{ph}t)} - 2e^{ik(x-c_{ph}t)}\right) \tag{A.24}$$

$$e^{ikc_{ph}\Delta t} - 2 + e^{-ikc_{ph}\Delta t} = \frac{c^2}{c_\Delta^2}\left(e^{ik\Delta x} + e^{-ik\Delta x} - 2\right) \tag{A.25}$$

Since $\cos(\theta) = \frac{e^{i\theta}+e^{-i\theta}}{2}$,

$$2\cos(kc_{ph}\Delta t) - 2 = \frac{c^2}{c_\Delta^2}(2\cos(k\Delta x) - 2) \tag{A.26}$$

Since $\cos(\theta) - 1 = -2\sin^2(\theta/2)$,

$$\sin^2(kc_{ph}\Delta t/2) = \frac{c^2}{c_\Delta^2}\sin^2(k\Delta x/2) \tag{A.27}$$

or,

$$\frac{c_\Delta}{c} = \frac{\sin(k\Delta x/2)}{\sin(kc_{ph}\Delta t/2)} \tag{A.28}$$

We can replace k with ω/c_{ph} and Δx with $c_\Delta \Delta t$ to obtain eq. 6.5:

$$\frac{c_\Delta}{c} = \frac{\sin(\omega c_\Delta \Delta t/2c_{ph})}{\sin(\omega\Delta t/2)} \tag{6.5}$$

This equation implicitly determines the phase velocity c_{ph} as a function of frequency ω and the simulation parameters. It can be solved explicity for c_{ph} to determine the dispersion:

$$c_{ph} = \frac{\omega c_\Delta \Delta t}{2\text{arcsin}\left[\frac{c_\Delta}{c}\sin\left(\frac{\omega\Delta t}{2}\right)\right]} \tag{A.29}$$

A.6 Derivation of the force-displacement equation for the dry-contact model

The dry-contact model uses an array of pins of random length pressed between flat surfaces as a model for a crack or dry contact. Figure 6.3 illustrates this behavior. We assume that the force-displacement relation of the dry contact follows the expectation of the force in terms of displacement for this stochastic model.

We assume the pins have normally distributed length, with average length L. The probability density function for the length l of a particular pin is: $f_l(l, \sigma^2) = \frac{1}{\sqrt{2\pi}\sigma} e^{-\frac{(l-L)^2}{2\sigma^2}}$.

Given a displacement of y (positive y $\sim$ increasing separation) relative to the nominal distance L between the two surfaces, the force in the particular pin (area A, length l) is (positive tensile):

$$F = \begin{cases} AE(y - (l - L))/L & \text{if } y < l - L \\ 0 & \text{otherwise} \end{cases} \tag{A.30}$$

We would like to find the probability density function (PDF) for F so that we can determine the expectation of F. We will do this by first determining the cumulative density functions (CDF's):

$$P(l < l_0) = F_l(l_0) = \int_{-\infty}^{l_0} f_l(l) dl \tag{A.31}$$

$$P(F < F_0) = F_F(F_0) = \int_{-\infty}^{F_0} f_F(F) dF \tag{A.32}$$

where l_0 and F_0 are particular lengths of and forces in the pin, respectively. If

$l < y - L$, then $l = y + L - \frac{FL}{AE}$ and $l_0 = y + L - \frac{F_0 L}{AE}$ follow from eq. A.30. Therefore,

$$P(l < l_0) \equiv P\left(\left\{y + L - \frac{FL}{AE}\right\} < \left\{y + L - \frac{F_0 L}{AE}\right\}\right) \tag{A.33}$$

and

$$\begin{aligned} P(l < l_0) &= P(-F < -F_0) \\ &= P(F > F_0) \\ &= 1 - P(F < F_0) \end{aligned} \tag{A.34}$$

We can substitute the right hand sides of eqns. A.31 and A.32 into this equation under the condition $l_0 = y + L - \frac{F_0 L}{AE}$. Now:

$$\int_{-\infty}^{l_0} f_l(l)dl = 1 - \int_{-\infty}^{F_0} f_F(F)dF \tag{A.35}$$

Substituting in for l_0,

$$\int_{-\infty}^{y+L-\frac{F_0 L}{AE}} f_l(l)dl = 1 - \int_{-\infty}^{F_0} f_F(F)dF \tag{A.36}$$

We take the derivative of both sides with respect to F_0:

$$-\frac{L}{AE} f_l\left(y + L - \frac{F_0 L}{AE}\right) = -f_F(F_0) \tag{A.37}$$

So, the PDF for F (still restricted to $l < y - L$ or $F < 0$) is:

$$f_F(F) = \frac{L}{AE} f_l\left(y + L - \frac{FL}{AE}\right) \tag{A.38}$$

$$= \frac{L}{AE} \frac{1}{\sqrt{2\pi}\sigma} e^{-\frac{\left(y - \frac{FL}{AE}\right)^2}{2\sigma^2}} \tag{A.39}$$

(using the definition of $f_l(l)$.)

We would like to calculate the expectation $EF = \int_{-\infty}^{\infty} F f_F(F)dF$. So we have

$$EF = \frac{L}{AE} \frac{1}{\sqrt{2\pi}\sigma} \int_{-\infty}^{0} F e^{-\frac{\left(y - \frac{FL}{AE}\right)^2}{2\sigma^2}} dF \tag{A.40}$$

We have taken care of the $l >= y - L$ case here by limiting the bounds of integration. If there is no contact on a pin, the force is zero. Because of the F factor in the integral, there is no contribution to the expectation from pins that hold no force.

We substitute $u = y - \frac{FL}{AE}$ and $dF = \frac{-AE}{L}du$ within the integral, replacing F with u as the variable over which we integrate:

$$EF = \frac{L}{AE}\frac{1}{\sqrt{2\pi}\sigma}\int_{\infty}^{y}\frac{AE}{L}(y-u)e^{-\frac{u^2}{2\sigma^2}}\frac{-AE}{L}du \tag{A.41}$$

simplify:

$$EF = \frac{AE}{L}\frac{1}{\sqrt{2\pi}\sigma}\int_{y}^{\infty}(y-u)e^{-\frac{u^2}{2\sigma^2}}du \tag{A.42}$$

split the integral:

$$EF = \frac{AE}{L}\frac{1}{\sqrt{2\pi}\sigma}\int_{y}^{\infty}ye^{-\frac{u^2}{2\sigma^2}}du - \frac{AE}{L}\frac{1}{\sqrt{2\pi}\sigma}\int_{y}^{\infty}ue^{-\frac{u^2}{2\sigma^2}}du \tag{A.43}$$

let $v = \frac{u}{\sqrt{2}\sigma}$ and $w = -\frac{u^2}{2\sigma^2}$.

$$EF = \frac{yAE}{2L}\int_{\frac{y}{\sqrt{2}\sigma}}^{\infty}\frac{2}{\sqrt{\pi}}e^{-v^2}dv + \frac{AE}{L}\frac{\sigma}{\sqrt{2\pi}}\int_{-\frac{y^2}{2\sigma^2}}^{-\infty}e^{w}dw \tag{A.44}$$

Finally, evaluating the integrals and assuming the force is equal to its expectation gives equation 6.8:

$$F \;=\; \frac{yAE}{2L}\,\mathrm{erfc}\left(\frac{y}{\sqrt{2}\sigma}\right) \;-\; \frac{\sigma AE}{L\sqrt{2\pi}}e^{-\frac{y^2}{2\sigma^2}} \tag{6.8}$$

A.7 Demonstration of the analytic solution

We demonstrate how the analytic solution, equation 7.2:

$$y = f\left(t - \sqrt{\frac{\rho}{E_1}}x\right) - \frac{E_2\rho}{2E_1^2}x\left[f'\left(t - \sqrt{\frac{\rho}{E_1}}x\right)\right]^2 \tag{7.2}$$

approximately solves the nonlinear PDE of equation 6.2:

$$\frac{\partial^2 y}{\partial t^2} \;=\; \frac{E_1}{\rho}\frac{\partial^2 y}{\partial x^2} \;+\; 2\frac{E_2}{\rho}\frac{\partial y}{\partial x}\frac{\partial^2 y}{\partial x^2} \tag{6.2}$$

We start by applying the D'Alembert solution to the nonlinear term $2\frac{E_2}{\rho}\frac{\partial y}{\partial x}\frac{\partial^2 y}{\partial x^2}$ of the PDE. The D'Alembert solution is $y = f\left(t - \sqrt{\frac{\rho}{E_1}}x\right)$.

$$\frac{\partial y}{\partial x} = f'\left(t - \sqrt{\frac{\rho}{E_1}}x\right)\left(-\sqrt{\frac{\rho}{E_1}}\right) \tag{A.45}$$

$$\frac{\partial^2 y}{\partial x^2} = f''\left(t - \sqrt{\frac{\rho}{E_1}}x\right)\left(\frac{\rho}{E_1}\right) \tag{A.46}$$

$$\begin{aligned}\frac{\partial y}{\partial x}\frac{\partial^2 y}{\partial x^2} &= f'\left(t - \sqrt{\frac{\rho}{E_1}}x\right) f''\left(t - \sqrt{\frac{\rho}{E_1}}x\right)\left(-\frac{\rho}{E_1}\right)^{\frac{3}{2}} \\ &= \frac{1}{2}\frac{\rho}{E_1}\frac{\partial}{\partial x}\left(\left[f'\left(t - \sqrt{\frac{\rho}{E_1}}x\right)\right]^2\right)\end{aligned} \tag{A.47}$$

So the nonlinear term of the PDE, after substitution is:

$$\frac{E_2}{E_1}\frac{\partial}{\partial x}\left(\left[f'\left(t - \sqrt{\frac{\rho}{E_1}}x\right)\right]^2\right) \tag{A.48}$$

and the PDE as a whole, with the D'Alembert solution substituted into the nonlinear term is eq. 7.1:

$$\frac{\partial^2 y}{\partial t^2} \;=\; \frac{E_1}{\rho}\frac{\partial^2 y}{\partial x^2} \;+\; \frac{E_2}{E_1}\frac{\partial}{\partial x}\left(\left[f'\left(t - \sqrt{\frac{\rho}{E_1}}x\right)\right]^2\right) \tag{7.1}$$

Lamb's solution to this is eq. 7.2 [17]:

$$y = f\left(t - \sqrt{\frac{\rho}{E_1}}x\right) - \frac{E_2\rho}{2E_1^2}x\left[f'\left(t - \sqrt{\frac{\rho}{E_1}}x\right)\right]^2 \tag{7.2}$$

We substitute Lamb's solution into the linear terms of the PDE. Up to here, we have only substituted the D'Alembert solution into the nonlinear term of the PDE.

$$\frac{\partial y}{\partial x} = -f'\left(t-\sqrt{\frac{\rho}{E_1}}x\right)\sqrt{\frac{\rho}{E_1}} \\ -\frac{E_2\rho}{2E_1^2}x\frac{\partial}{\partial x}\left[f'\left(t-\sqrt{\frac{\rho}{E_1}}x\right)\right]^2 - \frac{E_2\rho}{2E_1^2}\left[f'\left(t-\sqrt{\frac{\rho}{E_1}}x\right)\right]^2 \quad \text{(A.49)}$$

$$\frac{\partial^2 y}{\partial x^2} = f''\left(t-\sqrt{\frac{\rho}{E_1}}x\right)\frac{\rho}{E_1} - \frac{E_2\rho}{2E_1^2}x\frac{\partial^2}{\partial x^2}\left[f'\left(t-\sqrt{\frac{\rho}{E_1}}x\right)\right]^2 \\ -\frac{E_2\rho}{2E_1^2}\frac{\partial}{\partial x}\left[f'\left(t-\sqrt{\frac{\rho}{E_1}}x\right)\right]^2 - \frac{E_2\rho}{2E_1^2}\frac{\partial}{\partial x}\left[f'\left(t-\sqrt{\frac{\rho}{E_1}}x\right)\right]^2 \quad \text{(A.50)}$$

$$\frac{\partial y}{\partial t} = f'\left(t-\sqrt{\frac{\rho}{E_1}}x\right) - \frac{E_2\rho}{2E_1^2}x\frac{\partial}{\partial t}\left[f'\left(t-\sqrt{\frac{\rho}{E_1}}x\right)\right]^2 \quad \text{(A.51)}$$

$$\begin{aligned}\frac{\partial^2 y}{\partial t^2} &= f''\left(t-\sqrt{\frac{\rho}{E_1}}x\right) - \frac{E_2\rho}{2E_1^2}x\frac{\partial^2}{\partial t^2}\left[f'\left(t-\sqrt{\frac{\rho}{E_1}}x\right)\right]^2 \\ &= f''\left(t-\sqrt{\frac{\rho}{E_1}}x\right) - \frac{E_2\rho}{2E_1^2}x\frac{E_1}{\rho}\frac{\partial^2}{\partial x^2}\left[f'\left(t-\sqrt{\frac{\rho}{E_1}}x\right)\right]^2 \quad \text{(A.52)}\end{aligned}$$

Put it all together:

$$f''\left(t-\sqrt{\frac{\rho}{E_1}}x\right) - \frac{E_2\rho}{2E_1^2}x\frac{E_1}{\rho}\frac{\partial^2}{\partial x^2}\left[f'\left(t-\sqrt{\frac{\rho}{E_1}}x\right)\right]^2 = \frac{E_1}{\rho}f''\left(t-\sqrt{\frac{\rho}{E_1}}x\right)\frac{\rho}{E_1} \\ -\frac{E_1}{\rho}\frac{E_2\rho}{2E_1^2}x\frac{\partial^2}{\partial x^2}\left[f'\left(t-\sqrt{\frac{\rho}{E_1}}x\right)\right]^2 - \frac{E_1}{\rho}\frac{E_2\rho}{2E_1^2}\frac{\partial}{\partial x}\left[f'\left(t-\sqrt{\frac{\rho}{E_1}}x\right)\right]^2 \\ -\frac{E_1}{\rho}\frac{E_2\rho}{2E_1^2}\frac{\partial}{\partial x}\left[f'\left(t-\sqrt{\frac{\rho}{E_1}}x\right)\right]^2 + \frac{E_2}{E_1}\frac{\partial}{\partial x}\left(\left[f'\left(t-\sqrt{\frac{\rho}{E_1}}x\right)\right]^2\right) \quad \text{(A.53)}$$

$$f''\left(t-\sqrt{\frac{\rho}{E_1}}x\right) - \frac{E_2}{2E_1}x\frac{\partial^2}{\partial x^2}\left[f'\left(t-\sqrt{\frac{\rho}{E_1}}x\right)\right]^2 = f''\left(t-\sqrt{\frac{\rho}{E_1}}x\right) \\ -\frac{E_2}{2E_1}x\frac{\partial^2}{\partial x^2}\left[f'\left(t-\sqrt{\frac{\rho}{E_1}}x\right)\right]^2 - \frac{E_2}{2E_1}\frac{\partial}{\partial x}\left[f'\left(t-\sqrt{\frac{\rho}{E_1}}x\right)\right]^2 \\ -\frac{E_2}{2E_1}\frac{\partial}{\partial x}\left[f'\left(t-\sqrt{\frac{\rho}{E_1}}x\right)\right]^2 + \frac{E_2}{E_1}\frac{\partial}{\partial x}\left(\left[f'\left(t-\sqrt{\frac{\rho}{E_1}}x\right)\right]^2\right) \quad \text{(A.54)}$$

$$\begin{aligned}0 &= -\frac{E_2}{2E_1}\frac{\partial}{\partial x}\left[f'\left(t-\sqrt{\frac{\rho}{E_1}}x\right)\right]^2 - \frac{E_2}{2E_1}\frac{\partial}{\partial x}\left[f'\left(t-\sqrt{\frac{\rho}{E_1}}x\right)\right]^2 \\ &\quad + \frac{E_2}{E_1}\frac{\partial}{\partial x}\left(\left[f'\left(t-\sqrt{\frac{\rho}{E_1}}x\right)\right]^2\right) \quad \text{(A.55)}\end{aligned}$$

$$0 = 0 \tag{A.56}$$

Therefore eq. 7.2 solves eq. 7.1 and approximately solves the nonlinear PDE of eq. 6.2.

A.8 Demonstration of mapping the analytic solution to our model

In section 7.4, we claimed that we could map the modified analytic solution eq. 7.4:

$$g = f\left(t - \sqrt{\frac{\rho}{E_1}}x\right) - \frac{E_2\rho}{2E_1^2}x\frac{\partial}{\partial t}\left(\left[f\left(t - \sqrt{\frac{\rho}{E_1}}x\right)\right]^2\right) \tag{7.4}$$

onto our model from chapter 3:

$$\hat{g} = \mathbf{A} \otimes f(t) + \mathbf{B} \otimes f^2(t) \tag{3.9}$$

by applying:

$$\mathbf{A} \;=\; \delta\left(t - \sqrt{\frac{\rho}{E_1}}x\right) \tag{7.5}$$

and

$$\mathbf{B} \;=\; -\frac{E_2\rho}{2E_1^2}x\frac{\partial}{\partial t}\delta\left(t - \sqrt{\frac{\rho}{E_1}}x\right) \tag{7.6}$$

This can be demonstrated by substitution of $\mathbf{A}$ and $\mathbf{B}$ into eq. 3.9:

$$\hat{g} = \delta\left(t - \sqrt{\frac{\rho}{E_1}}x\right) \otimes f(t) - \left[\frac{E_2\rho}{2E_1^2}x\frac{\partial}{\partial t}\delta\left(t - \sqrt{\frac{\rho}{E_1}}x\right)\right] \otimes f^2(t) \tag{A.57}$$

or

$$\hat{g} = f\left(t - \sqrt{\frac{\rho}{E_1}}x\right) - \frac{E_2\rho}{2E_1^2}x\frac{\partial}{\partial t}\left[\delta\left(t - \sqrt{\frac{\rho}{E_1}}x\right) \otimes f^2(t)\right] \tag{A.58}$$

or

$$\hat{g} = f\left(t - \sqrt{\frac{\rho}{E_1}}x\right) - \frac{E_2\rho}{2E_1^2}x\frac{\partial}{\partial t}f^2\left(t - \sqrt{\frac{\rho}{E_1}}x\right) \tag{A.59}$$

which is the same as eq. 7.4:

$$g = f\left(t - \sqrt{\frac{\rho}{E_1}}x\right) - \frac{E_2\rho}{2E_1^2}x\frac{\partial}{\partial t}\left(\left[f\left(t - \sqrt{\frac{\rho}{E_1}}x\right)\right]^2\right) \tag{7.4}$$

APPENDIX B

CONTROL FIRMWARE FOR AN ULTRASONIC MEASUREMENT SYSTEM

The Ritec RAM-5000 measurement system, as we obtained it, was without a useful means of automatic control. For a complex measurement algorithm such as the one we have described, automatic computer control of the measurement is needed. The RAM-5000 has no physical front panel controls. It came with a computer program in BASIC that simulates front panel controls. This program directly manipulates control registers in the RAM-5000 unit through a digital I/O card. Unfortunately, these registers are write-only, so the state of the unit is known only by the BASIC program. This effectively precludes external control of the RAM-5000.

Because of the complexity of the measurement algorithm described in this thesis, kludging the required automatic control into the BASIC program was not an option. Therefore we entered into a cooperative agreement with the manufacturer to develop both an improved control program and a virtual front-panel that would allow effective remote control of the instrument.

B.1 An Internet-enabled client/server laboratory instrument

The standard control interface for laboratory instrumentation is the General Purpose Interface Bus (GPIB), also known by the designation IEEE-488. By modern standards, GPIB is costly and slow. We designed our control firmware to

be based on the TCP/IP networking standard. TCP/IP allows the instrument to be controlled transparently from the local host or over the Internet. The control firmware is based on a client/server architecture. Clients, such as the virtual front panel or an automated control program, send commands and status queries to the server. The server manages the internal state of the equipment. The virtual front panel, which can run as an independent application or as a Java applet within a web browser, provides an intuitive interface to controlling the hardware functions.

In principle, the server and client could be provided on an embedded computer within the RAM-5000 case. This computer could have an embedded display that runs the virtual front panel, or it could use a web server to download the virtual front panel to clients over the network.

B.2 The RAM-5000 control server

We developed the RAM-5000 control server in the C language. It accepts commands and queries over TCP/IP connections. The commands and queries are in human-readable text format, similar to the format commonly used with GPIB. Any telnet client can be used to manually issue commands and queries by connecting to the server port (typically 1647). A few of the possible commands are listed in table B.1. Security is handled through plaintext authorization codes that are required for access (in a hostile network environment it would be wise to tunnel network accesses through a secure protocol, such as Secure Sockets Layer (SSL) or Secure Shell (SSH)). The server responds to commands by manipulating control registers and updating its internal representation of the state of the

Sample RAM-5000 server commands

SYS:TRIGGER	Perform computer trigger
TIMING:FREQ<i>	Frequency selection
GA<i>:DELAY	Desired gated amplifier delay
GA<i>:WIDTH	Desired gated amplifier width
ALC:GA<i>:BURSTWIDTH	Hardware gated amplifier burst width
SYS:GA<i>:RFLEVEL	Gated amplifier RF level
LOCKOUT	Lock out all other clients
TIMING:REPRATE	Set internal repetition rate
RECV:IN<i>:FREQ	Receiver frequency
RECV:IN<i>:FREQN	Receiver frequency tracking expression
RECV:IN<i>:GAIN	Receiver gain
SYS:INTRE	Read real part of integrator output
SYS:INTIM	Read imaginary part of integrator output
RECV:IN<i>:HIGHPASS	High pass filter selection
RECV:IN<i>:INTDELAY	Integrator gate delay
RECV:IN<i>:INTWIDTH	Integrator gate width
RECV:IN<i>:LOWPASS	Low pass filter selection
QUIT	Disconnect from ram-server

Table B.1: Partial list of server commands.

```
goliath% telnet localhost 1647
Trying 127.0.0.1...
Connected to localhost.
Escape character is '^]'.
auth xyzzy
200 0008 AUTH_OK
ga1:delay 1.2 ms
200 0018 GA1:DELAY 1200 us
ga1:width 14 200 0016 GA1:WIDTH 14 us recv:in2:gain?
200 0020 RECV:IN2:GAIN 22 dB
recv:in1:gnai
504 0022 ERROR INVALID_COMMAND
recv:in1:freqn 2*ga1*cos(ga2)
200 0030 RECV:IN1:FREQN 2*ga1*cos(ga2)
recv:in1:freq?
200 0031 RECV:IN1:FREQ 1.7551651275 MHz
timing:freq1 14.7
200 0036 TIMING:FREQ1 14.699999991501681 MHz
recv:in1:freq?
200 0032 RECV:IN1:FREQ 25.8009271803 MHz
quit
Connection closed by foreign host.
goliath%
```

Figure B.1: A sample transcript of direct communication with the server using `telnet`.
Commands typed by the user are in boldface and the responses from the server are in typewriter font.

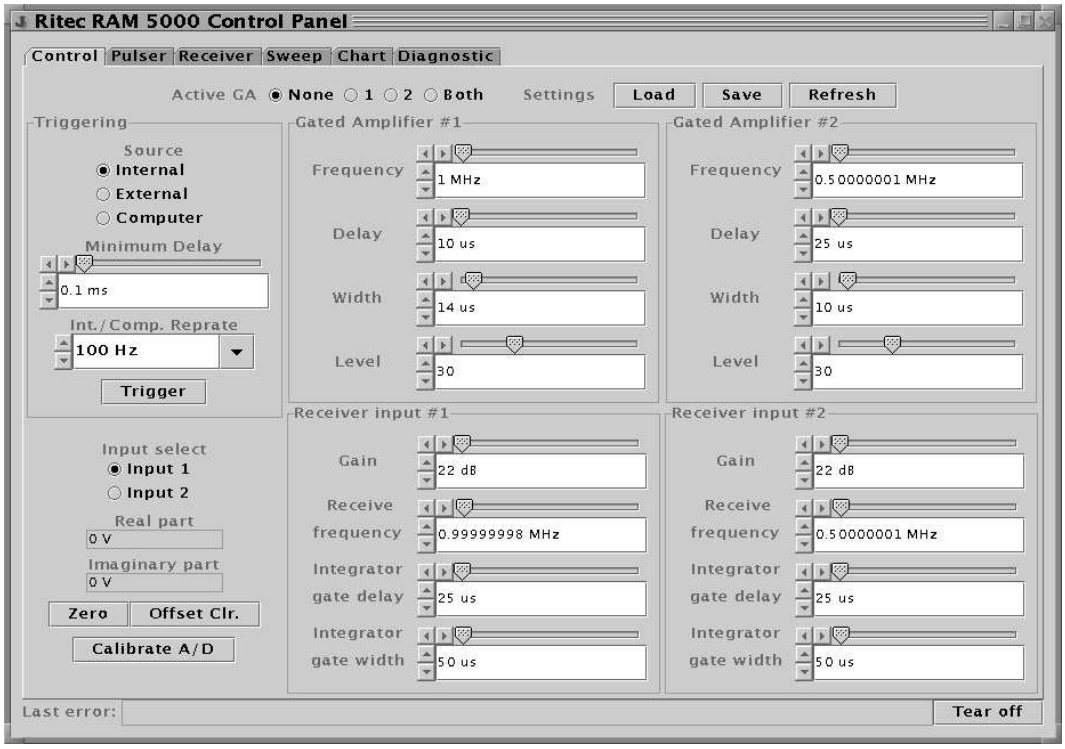

Figure B.2: Screenshot of the virtual front panel controls.

instrument. Since the hardware registers are write-only, it responds to queries by reporting its internal representation of the state of the instrument. The server also enforces safety criteria to prevent the hardware from exceeding its design specifications.

B.3 The virtual front panel

The RAM-5000 virtual front panel is a Graphical User Interface (GUI) to the underlying functions of the control server. Figure B.2 shows a screenshot of the virtual front panel. Each control maps directly to an underlying server command. The tabs along the top select different control panes. The virtual front panel provides direct control of hardware settings, macro control of hardware settings,

result monitoring, hardware diagnostic readout, and a frequency sweep function for making complex measurements. The virtual front panel was written in Java with the Swing toolkit and has an object-oriented architecture that maps GUI widget sets directly to commands on the control server.

B.4 Conclusions

The control server/firmware we developed for the Ritec RAM-5000 allowed both far more flexible automatic control, and easier manual control than the original software. Our text-based control interface provided an abstraction layer that isolated our implementation of the time-resolved measurement algorithm both from the details of the underlying hardware and from manual control requirements. For purposes of comparison, the RAM-5000 control server and GUI are about 16,000 lines of C and Java. This complexity is isolated from the 7,500 lines of C and C++ in our time-resolved measurement software. Implementing the time-resolved measurement algorithm would have been an almost impossible, complex task without a control interface and abstraction layer such as this firmware.

APPENDIX C

DESIGN OF A JIG TO HOLD TRANSDUCERS FOR MEASUREMENT OF THE CRACKED TITANIUM SAMPLE

In order to measure waveforms from the cracked titanium sample of chapter 8, it was necessary to build a jig to hold the transducers in place. In order to hold the source and receiver transducers in place, the jig had to attach to the sample and hold the transducers tightly in place. For repeatable contact force, the transducers had to be spring-loaded to the sample. To allow for multiple experiments under different conditions, the jig had to be able to hold many different types of transducers, each with their own physical dimensions. The jig was designed to use interlocking Teflon inserts to tightly hold a wide variety of possible transducers. Figure C.1 shows the jig design and figure C.2 shows the design of the Teflon inserts. A photograph is given in figure C.3.

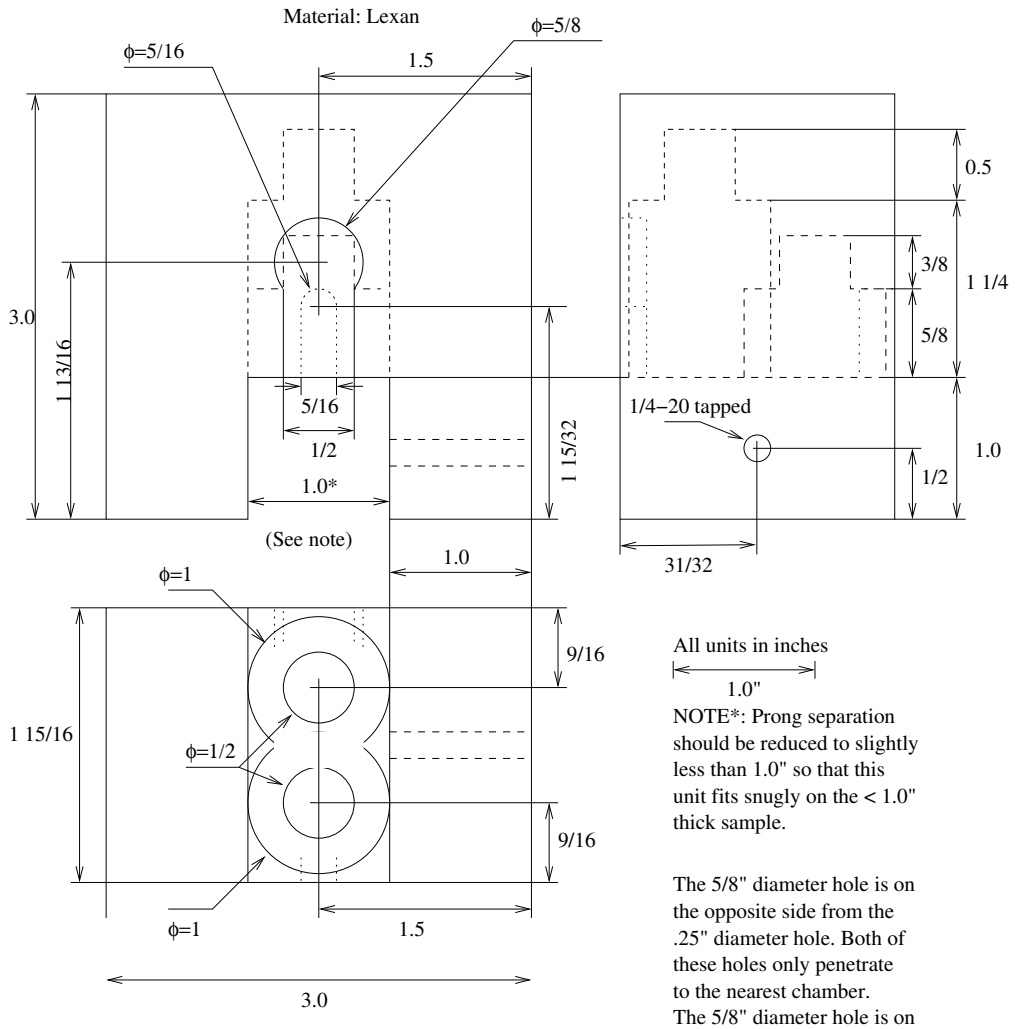

Figure C.1: Design of a jig to hold transducers for the measurement of a cracked titanium sample.

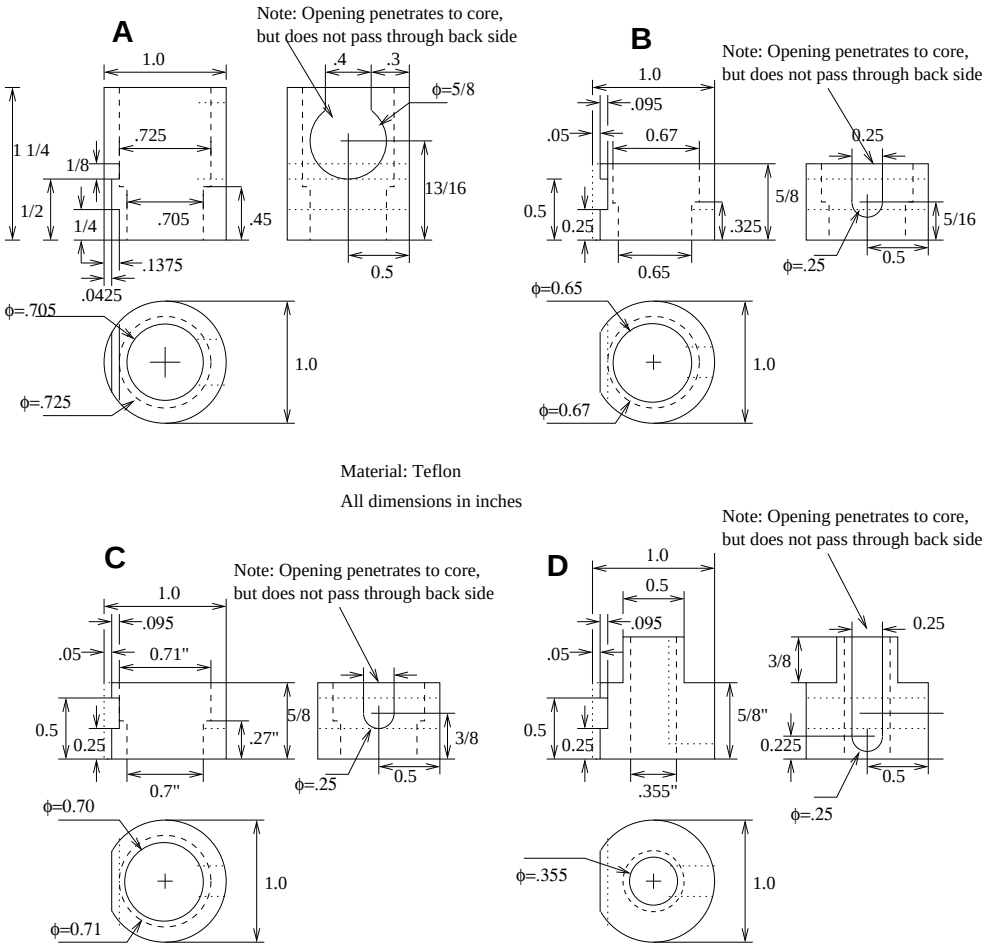

Figure C.2: Design of Teflon transducer-holding inserts for a jig to hold transducers for the measurement of a cracked titanium sample.

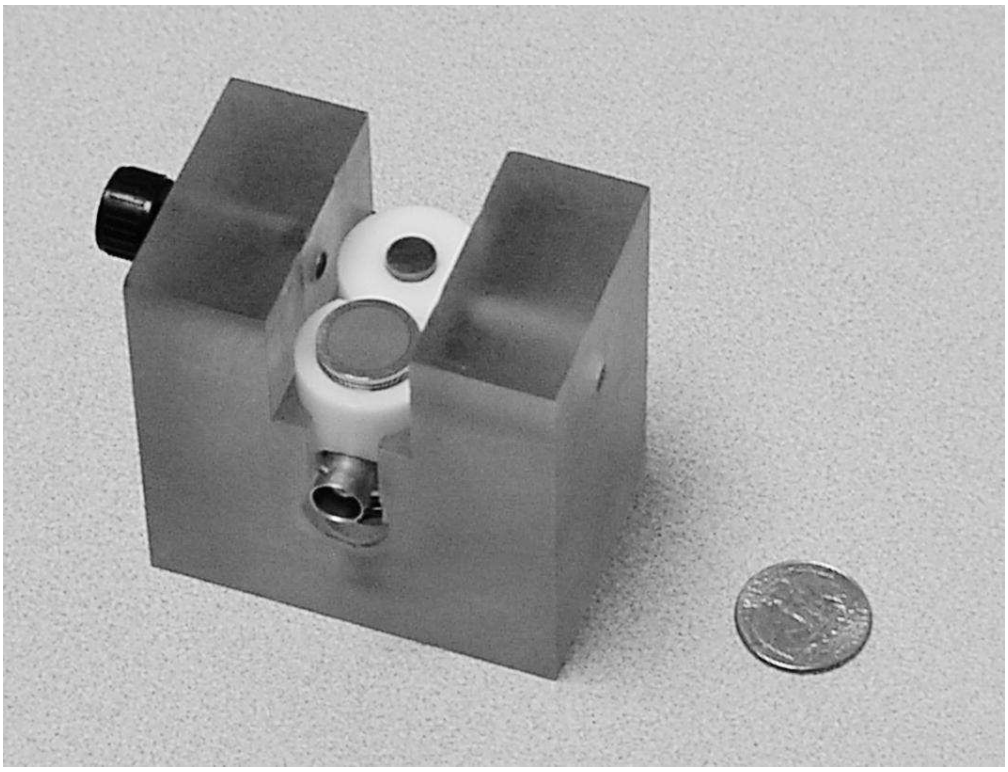

Figure C.3: Photograph of the transducer jig with two inserts and two transducers.

REFERENCES

[1] K. E.-A. Van Den Abeele, J. Carmeliet, J. A. Ten Cate, and P. Johnson, Nonlinear Elastic Waves Spectroscopy (NEWS) techniques to discern material damage. Part II: Single Mode Nonlinear Resonance Acoustic Spectroscopy, Res. in Nondest. Eval. 12 (2000) 31.

[2] K. E.-A. Van Den Abeele, P. Johnson, and A. Sutin, Nonlinear Elastic Waves Spectroscopy (NEWS) techniques to discern material damage. Part I: Nonlinear Wave Modulation Spectroscopy (NWMS), Res. in Nondest. Eval. 12 (2000) 17.

[3] R. T. Beyer, Parameter of nonlinearity in fluids, J. Acoust. Soc. Am. 32 (1960) 719.

[4] L. Bjørnø, Nonlinear acoustics, Acoustics and Vibration Progress, Vol. 2 (1976), R.W.B. Stephens and H.G. Leventhall, eds. pp. 179-199.

[5] M. A. Breazeale, Third-order elastic constants of cubic crystals, Handbook of Elastic Properties of Solids, Liquids, and Gasses, M. Levy, H. E. Bass, and R. R. Stern eds., Volume I: Dynamic Methods for Measuring the Elastic Properties of Solids, A. G Every and W. Sachse vol. eds., Academic Press, 2001, pp. 489-510.

[6] M. A. Breazeale and J. Philip, Determination of Third Order Elastic Constants from Ultrasonic Harmonic Generation Measurements, Physical Acoustics, Vol XVII, W. P. Mason and R. N. Thurston eds., Academic Press, 1984, pp. 1-60.

[7] M. A. Breazeale and D. O. Thompson, Finite-amplitude ultrasonic waves in aluminum, Appl. Phys. Let. 3 (1963) 77.

[8] P. P. Delsanto, S. Hirsekorn, V. Agostini, R. Loparco, and A. Koka, Modeling the propagation of ultrasonic waves in the interface region between two bonded elements (in press), Ultrasonics xxx (2002) xxx.

[9] S. Earnshaw, On the mathematical theory of sound, Phil. Trans. Roy. Soc. (London) 150 (1860), 133.

[10] Gage Applied Sciences, Online Product Catalog 2002, http://www.gage-applied.com.

[11] I. D. Gits, V. V. Gushchin, and B. A. Konyukhov, Variation of the nonlinear distortion of sound waves in polycrystalline aluminium during fatigue tests, Soviet Phys. (Acoust.) 19 (1973) 221.

[12] C. M. Hedberg and O.V. Rudenko, Pulse response of a nonlinear layer, J. Acoust. Soc. Am. 110 (2001) 2340.

[13] A. Hikata, B. B. Chick, and C. Elbaum, Effect of dislocations on finite amplitude ultrasonic waves in aluminum, Appl. Phys. Let. 3 (1963) 195.

[14] S. D. Holland, W. Sachse, A time-resolved method for nonlinear ultrasonic measurements (in press), Ultrasonics xxx (2002) xxx.

[15] P. A. Johnson, The new wave in acoustic testing, Materials World, 7 (1999) 544.

[16] V. A. Krassilnikov, V. V. Schklovskaya-Kordi, and L. K. Zarembo, On the propagation of ultrasonic waves of finite amplitudes in liquids, J. Acoust. Soc. Amer. 29 (1957) 642.

[17] Sir H. Lamb, The Dynamical Theory of Sound, Second Edition, Edward Arnold & Co., London, 1931.

[18] F. J. Pompei, The use of airborne ultrasonics for generating audible sound beams, J. Audio Eng. Soc. 47 (1999) 726.

[19] Ritec, Inc., Ritec Advanced Measurement System Model RAM-5000-SNAP, http://www.ritecinc.com.

[20] F. R. Rollins, L. H. Taylor, and P. H. Todd, Jr., Ultrasonic study of three-phonon interactions: II. Experimental results, Phys. Rev. 136A (1964) A597.

[21] E. V. Romanenko, Experimental investigation of the propagation of finite-amplitude spherical waves, Soviet Phys. (Acoust.) 5 (1959) 100.

[22] R. P. Ryan, A. G. Lutsch, and R. P. Beyer, Measurement of the distortion of finite ultrasonic waves in liquids by a pulse method, J. Acoust. Soc. Amer. 34 (1962) 31.

[23] M. Schetzen, The Volterra and Weiner Theories of Nonlinear Systems, John Wiley and Sons, New York, 1980.

[24] I. Y. Solodov, Ultrasonics of non-linear contacts: propagation, reflection, and NDE applications, Ultrasonics 36 (1998) 383.

[25] I. Y. Solodov, N. Krohn, G. Busse, CAN: an example of nonclassical acoustic nonlinearity in solids (in press), Ultrasonics xxx (2002) xxx.

[26] J. A. Ten Cate and T. J. Shankland, Slow dynamics in the nonlinear elastic response of Berea sandstone, Geophys. Res. Let. 23 (1996) 3019.

[27] A. L. Thuras, R. T. Jenkins, and H. T. O'Neil, Extraneous frequencies generated in air carrying intense sound waves, J. Acoust. Soc. Amer. 6 (1935) 173.

[28] F. Tranquart, N. Grenier, V. Eder, and L. Pourcelot, Clinical use of ultrasound tissue harmonic imaging, Ultrasound in Medicine and Biology 25 (1999) 889.

[29] V. Volterra, Theory of Functionals and of Integral and Integro-Differential Equations, Dover Publications, New York, 1959.

[30] K. H. Waters, Reflection Seismology: A Tool for Energy Resource Exploration, Third Edition, John Wiley and Sons, New York, 1987.